

**NASA**  
**Technical**  
**Paper**  
**2345**

January 1985

Aerothermal Tests of a  
12.5° Cone at Mach 6.7  
for Various Reynolds  
Numbers, Angles of  
Attack, and Nose Shapes

Robert J. Nowak,  
Cindy W. Albertson,  
and L. Roane Hunt

**NASA  
Technical  
Paper  
2345**

1985

**Aerothermal Tests of a  
12.5° Cone at Mach 6.7  
for Various Reynolds  
Numbers, Angles of  
Attack, and Nose Shapes**

Robert J. Nowak,  
Cindy W. Albertson,  
and L. Roane Hunt

*Langley Research Center  
Hampton, Virginia*



National Aeronautics  
and Space Administration

**Scientific and Technical  
Information Branch**

## SUMMARY

An experimental investigation was conducted in the Langley 8-Foot High-Temperature Tunnel at Mach 6.7 to determine the effects of free-stream unit Reynolds number, angle of attack, and nose shape on the aerothermal environment of a 3-ft base-diameter, 12.5° half-angle cone. The average total temperature was 3300°R, the free-stream unit Reynolds number ranged from  $0.4 \times 10^6$  to  $1.4 \times 10^6$  per foot, and the angle of attack ranged from 0° to 10°. Three nose configurations were tested on the cone: a 3-in-radius tip, a 1-in-radius tip on an ogive frustum, and a sharp tip on an ogive frustum. Surface-pressure and cold-wall (ratio of wall temperature to total temperature of 0.16) heating-rate distributions were obtained for laminar, transitional, and turbulent boundary layers. Shock shapes and profiles of Mach number and total temperature in the shock layer were obtained.

Surface-pressure data were independent of free-stream Reynolds number and required longer distances to recover from nose overexpansion as bluntness increased. Windward pressure data were well predicted by an inviscid flow-field code for the present range of angle of attack. Laminar heating data normalized by the stagnation-point heat transfer were independent of free-stream Reynolds number and were well predicted on the windward side. Turbulent heating levels were in agreement with an empirical method. The location of the start of transition moved forward on both the windward and leeward sides with increasing free-stream Reynolds number, increasing angle of attack, and decreasing nose bluntness.

## INTRODUCTION

Applications of conical shapes for high-speed vehicles have led to a large aerothermal data base for cones. Although many experimental investigations have been done on cones in high-enthalpy hypersonic flow, several aspects of aerothermal heating are not fully understood and additional data are needed. Some of these aspects are as follows: (1) The location of the start of transition on blunt cones at angle of attack is not well understood and, in fact, conflicting trends have been observed. (See, for example, refs. 1 to 3.) (2) Methods for accurately predicting leeward heating are not available (refs. 4 and 5), although progress is being made through the use of the parabolized Navier-Stokes (PNS) equations (ref. 6). (3) Various types of slender-body nose shapes (ogives, for example) are often used on hypersonic vehicles and missiles; but despite the frequent use of ogives, there is a lack of heating data in the open literature at Mach 7 and above. Because of these deficiencies in the existing data base, the present study was performed to provide additional experimental data on transition location, leeward heating, and ogive aeroheating.

A 3-ft base-diameter, 12.5° half-angle cone with three interchangeable nose configurations was tested in the Langley 8-Foot High-Temperature Tunnel (8-ft HTT) at a free-stream Mach number of 6.7, a total temperature of 3300°R, free-stream unit Reynolds numbers from  $0.4 \times 10^6$  to  $1.4 \times 10^6$  per foot, and angles of attack up to 10°. The nose shapes tested were a 3-in-radius tip, a 1-in-radius tip on an ogive frustum, and a sharp tip on an ogive frustum. The large size of the model enabled high local Reynolds numbers plus flow-field surveys from three sets of retractable

rakes. Surface-pressure and cold-wall (ratio of wall temperature to total temperature of 0.16) heating-rate distributions were obtained for laminar, transitional, and turbulent boundary layers. Shock shapes and profiles of Mach number and total temperature in the shock layer were obtained.

The pressure data and shock-layer profiles are compared with predictions from an inviscid three-dimensional computer code referred to as STEIN (supersonic three-dimensional external inviscid). (See refs. 7 and 8.) Laminar heat-transfer data are compared with the code described in reference 9. Turbulent heating levels are compared with semiempirical reference-temperature methods described in references 10 to 13 and with the code described in references 14 and 15.

#### SYMBOLS

$c_p$	specific heat, Btu/lb-°R
$k$	thermal conductivity, Btu/ft-sec-°R
$M$	Mach number
$N_{Pr}^*$	Prandtl number, $(c_p \mu / k)^*$
$N_{Re}$	free-stream unit Reynolds number, $\rho_\infty V_\infty / \mu_\infty$ , $\text{ft}^{-1}$
$N_{Re}^*$	local Reynolds number based on reference temperature, $\rho_e^* V_e s / \mu^*$
$N_{St}^*$	Stanton number based on reference temperature, $\dot{q} / [(T_{aw} - T_w) \rho_e^* V_e c_p^*]$
$p$	pressure, psia
$\dot{q}$	heat flux, Btu/ft <sup>2</sup> -sec
$r, \varphi, x$	cylindrical coordinates (see fig. 12)
$\bar{r}, \varphi, \theta$	spherical coordinates (see fig. 12)
$r_b$	base radius, in.
$r_n$	nose radius, in.
$s$	surface distance from stagnation point (see fig. 7), in.
$s_c$	surface distance from start of cone frustum (see fig. 7), in.
$T$	temperature, °R
$t$	time, sec
$V$	velocity, ft/sec
$y$	distance normal to axis of revolution (see fig. 7), $x$ , in.
$\alpha$	angle of attack, deg



$\gamma$	ratio of specific heats
$\Delta$	difference
$\eta$	distance normal to surface (see fig. 7), in.
$\mu$	viscosity, lb/ft-sec
$\rho$	density, lbm/ft <sup>3</sup>
$\tau$	skin thickness, in.

#### Subscripts:

aw	adiabatic wall
e	edge of boundary layer
s	stagnation point
spc	sharp cone
t	total condition of tunnel (combustor)
tr	start of transition
w	model wall
$\infty$	free stream

#### Superscript:

*	conditions at Eckert's reference temperature (see eq. (5)) as described in reference 10
---	---

## APPARATUS AND TESTS

### Model

The present test program included a portion devoted to studying film cooling by injection of a coolant through various types of noses. Film-cooling data, however, are not reported in this paper, but the cooling aspect plus the requirement to test the model near radiation equilibrium did influence the selection of nose shapes and some model design features.

The model, shown in figure 1 mounted in the test section of the Langley 8-Foot High-Temperature Tunnel, consisted of a cone frustum, three interchangeable nose tips, three shock-layer flow survey rakes, and a boattail base. The structure of the model is shown in figure 2. The cone frustum was 63.6 in. long with a 3-ft-diameter base and a 12.5° half-angle. This frustum consisted of an outer 0.060-in-thick ( $\pm 0.003$ ) René 41 skin supported by an inner load-bearing structural shell. The outer skin was attached to the inner shell only at the forward end of the frustum, which was threaded for attaching the noses. The outer skin was supported by the inner shell through five insulated support rings shown in figures 2 and 3. These support

rings were made of segmented insulated pads interconnected by a spring-loaded mechanism that allowed the rings to expand as the outer skin expanded upon heating. (See insert in fig. 3.) This mechanism was designed to allow the outer skin to reach temperatures up to about 2000°R without buckling. A 1-in-thick blanket of insulation was strapped to the inner shell between the rings, as shown in figures 2 and 3, to reduce heat losses from the inside of the outer skin. The surface contour of the cone frustum was measured, and the maximum longitudinal waviness was  $\pm 0.050$  in. with local angular deformations up to 0.1°. The cone frustum was painted to provide a uniform emissivity ( $0.8 \pm 0.1$ ) surface.

The boattail cover shown in figure 2 had a 19.7° half-angle cone frustum, was 36.3 in. long, and was made from 0.13-in-thick stainless steel. The purpose of the boattail was to protect the instrumentation wires and the remote multiplexed data system from the base flow. The rear of the boattail was attached to the sting, and the front was supported, but not restrained, by an aluminum ring. A 0.30-in. gap between the boattail and the cone frustum and a 0.15-in. backward-facing step allowed thermal growth and venting of the model during the entire test sequence. (See detail in fig. 2.)

The three nose shapes are shown in figure 4. The nose shown in figure 4(a) has a 3-in-radius spherical tip, which is attached to a 12.5° half-angle cone-frustum adapter, and is made from 0.9-in-thick mild steel. This nose configuration is referred to herein as nose R-3 (where the "R" designates radius and the "3" designates the nose radius in inches). The nose shown in figure 4(b), and referred to as nose R-1, has a solid 1-in-radius spherical tip of stainless steel and a 20° half-angle cone frustum. This nose is attached to a 0.083-in-thick stainless-steel ogive frustum that has a 74.15-in. radius. The fineness ratio of the full ogive is 2.50. (The fineness ratio is the length of the ogive, with its front extended to a sharp tip and its base extended to a zero slope, divided by the base diameter.) The third nose (fig. 4(c)), referred to as nose R-S, has a 20° half-angle, solid sharp tip (actual nose radius was approximately 0.02 in.) attached to the same ogive frustum as in figure 4(b). The tips on the ogive frustum were internally spring mounted to the base of the ogive to allow thermal growth. High-temperature insulation was placed against the inside of the ogive shell to reduce heat losses from the skin to the interior of the model. All junctions between each of the model segments were smooth except for the ogive frustum, in which the base was oversized and resulted in a rearward-facing step about 0.005 in. high.

Three sets of rake assemblies were used to survey the flow within the shock layer at three axial stations. Photographs of a rake assembly extended from the surface and retracted are shown in figure 5. Each rake consisted of three struts, a cover plate with a sharp beveled edge, and a floor plate with two static-pressure orifices between the struts. (See fig. 6.) Each strut contained either five pitot-pressure tubes, five sharp conical-tip static-pressure probes, or five stagnation-temperature probes. The heights of the probes above the surface were 0.20, 0.45, 0.82, 1.25, and 1.75 in. The pitot probes were 0.50 in. long from the strut to the orifice and had a 0.060-in. outside diameter (O.D.) and a 0.040-in. inside diameter (I.D.). The static-pressure probes had a 7.1° half-angle conical tip, with an overall length of 1.38 in. and an O.D. of 0.060 in. Four 0.020-in-diameter orifices spaced 90° apart and staggered 0.020 in. axially were a mean distance of 0.87 in. from the strut. Thermocouple wire beads (platinum versus platinum 13-percent rhodium) with single shielding platinum tubes were used for the temperature probes. These platinum shields had a 0.090-in. O.D. and a 0.072-in. I.D., and the end of each shield was 0.5 in. from the edge of the strut. Each rake was injected into the flow field of the cone by a double-acting pneumatic piston. Because disturbances in the

flow field due to the cover plate were considered a possibility, a fixed-rake assembly without a cover plate was also tested. The fixed-rake assembly consisted of a single strut, a floor plate, and five pitot probes spaced the same as on the movable rake assembly.

The rake assembly had clearance gaps of about 0.003 in. between the cover plate and frame. (See fig. 5.) The frame of the rake assemblies was attached to the outer skin of the cone frustum that was free to grow thermally. Despite the clearance gaps, local thermal distortions of the rake assembly sometimes prevented a rake from fully extending into the flow; thus rake data were not obtained for several model runs. Also, when the rake was retracted, as seen in figure 5(b), an open slot was formed between the lower beveled edge of the cover plate and the underside of the adjacent frame. The slot was about 0.06 in. high by about 2.75 in. long. The gaps and slot allowed some possible venting between the exterior and interior of the cone. Even though the cavity beneath the rake assembly was enclosed to prevent hot gas from entering the interior of the model, venting could still occur through instrumentation holes at the bottom of the rake assembly. In addition to the gaps and backward-facing slot, two other sources of roughness around the rake assemblies were the slight steps between the rake frames and the outer skin of the cone and the screw-heads that were only somewhat smoothed by ceramic cement.

### Instrumentation

The outer skin of the cone frustum was instrumented with 101 chromel-alumel 30-gage thermocouples and 30 surface-pressure orifices. The circumferential angular position  $\varphi$  and the surface distance  $s$ , measured from the stagnation point, are used to locate surface orifices and thermocouples. (See fig. 7.) The distance  $s$  to an instrument on the cone surface thus is different for each nose. Tables I and II give the coordinates for the instrumentation on the cone frustum and on the noses, and the thermocouple locations are shown schematically in figure 8. The thermocouples (denoted by T) are located at  $\varphi$  increments of  $22.5^\circ$ , and the pressure orifices (denoted by P) are at  $\varphi$  increments of  $45^\circ$ . The individual thermocouple wires, with expansion bends, were spot-welded to the inside surface. Special provisions were taken to ensure that each thermocouple lead was secured to prevent shorting and erroneous readings. Thermocouple attachment points were a minimum of 1-in. distance from any lumped mass to minimize conduction errors.

The pressure tubes, 0.090-in. O.D. and 0.060-in. I.D., were welded to the inside of the skin of the cone frustum and connected to strain-gage-type pressure transducers located within the model. Each tube was leak checked after installation. Two pressure tubes, one on the most windward ray and one on the most leeward ray, were attached to the boattail skin 3 in. from the base of the cone to measure the base pressure of the model. Additional thermocouples and pressure gages were mounted inside the cone at various locations to monitor the internal environment.

Nose R-3 had surface-pressure orifices at seven locations (fig. 9(a)). Unfortunately, the orifices were not in the pitch plane of the model because of an alignment problem. The pressure gages used for these seven orifices were small solid-state transducers with an operating-temperature limit of  $860^\circ\text{R}$ . The gages were mounted inside the nose in a region where the temperature remained low.

The ogive frustum used for noses R-1 and R-S contained 24 chromel-alumel 30-gage thermocouples spot-welded to the inside surface along three longitudinal rays

(fig. 9(b)). Nose R-1 also had a single pressure orifice at the axis of symmetry of the tip. Nose R-S contained no pressure orifices.

### Test Facility

The Langley 8-Foot High-Temperature Tunnel (formerly the Langley 8-Foot High-Temperature Structures Tunnel) is a large blowdown tunnel that simulates aerodynamic heating and pressure loading for a nominal Mach number of 7 at altitudes between 80 000 and 120 000 ft. (See fig. 10.) The high energy needed for simulation is obtained by burning a mixture of methane and air under pressure in the combustor and expanding the products of combustion through a conical-contoured nozzle into the open-jet test chamber. The flow enters a supersonic diffuser where it is pumped by an air ejector through a mixing tube and exhausted to the atmosphere through a subsonic diffuser. The tunnel operates at total temperatures from 2400°R to 3600°R, free-stream dynamic pressures from 250 to 1800 psf, free-stream unit Reynolds numbers from  $0.3 \times 10^6$  to  $2.2 \times 10^6$  per foot, and has a maximum run time of 120 sec.

The model is stored in the pod below the test stream to protect it from adverse tunnel start-up loads. Once the desired flow conditions are established, the model is inserted into the test stream on a hydraulically actuated elevator. Insertion time from the position where the top of the cone entered the flow until the nose was at the nozzle centerline was typically 1.5 sec. The model pitch system provides an angle-of-attack range to 20°. More detailed information about the tunnel can be found in reference 16. A single-pass on-axis schlieren system consisting of 2-ft-diameter mirrors, a horizontal knife edge, a 5-μsec-duration xenon-arc lamp, and a 70-mm camera, which operated up to 20 frames per second, was used for obtaining either schlieren or shadowgraph images.

### Test Conditions and Procedures

The model with the three nose configurations was tested in a total of 17 runs, as summarized in table III. The angle of attack was varied from 0° to 10°. (The model was pitched down for angle of attack.) Unit Reynolds number was varied only with nose R-3. The highest Reynolds number condition was selected for the other two configurations to provide the highest heating rates. Table IV gives the test conditions for each run. The total temperature  $T_t$  was measured in the combustor. The free-stream unit Reynolds number and Mach number were calculated by using measured pressures and temperatures from free-stream surveys (a typical survey is reported in ref. 16) and the thermal, transport, and flow properties of methane-air combustion products as reported in reference 17.

The test procedure consisted of first establishing steady flow conditions in the tunnel; next, the model was pitched to the desired angle of attack and inserted into the test stream. (The model was left in the stream for times up to 40 sec to obtain high surface temperatures for a future comparison with tests made with a coolant.) Representative time histories of several tunnel parameters are shown in figure 11. The model static pressure sometimes showed a slight overshoot because of a transient adjustment of the test-chamber pressure with model entry and exit. Cold-wall heating rates were calculated from the thermocouple outputs after the model pressure had stabilized. The three shock flow-field survey rakes were usually extended from the model after the flow was established about the model. For runs 4, 5, and 12, the rakes were fixed in the out position prior to model insertion, and heating results are not presented for these runs.

## Remote Multiplexed System and Data Processing

An advanced fiber-optic-linked data system, the remote multiplexed system (RMS), was housed in the model base area. (See fig. 2.) The advantages of the RMS are (1) it transmitted data from 192 channels through a simple fiber-optic cable, thus providing more room in the sting for additional conventional instrumentation leads; and (2) it provided data with reduced electrical noise because of the fiber-optic transmission line. Each RMS data channel was sampled 20 times per second, and all 192 data channels were scanned in 9.6 msec. The RMS transmitted data through the fiber-optic cable to a main control unit, located outside the wind tunnel, which was hard wired to a minicomputer where the data from the RMS plus data transmitted by conventional wiring were processed. All data signals from the RMS were filtered at 6 Hz; data not going through the RMS were filtered at 10 Hz. Additional information on the RMS and data processing can be found in reference 18.

## Data Reduction and Uncertainties

Pressure data were obtained with strain-gage transducers having an accuracy of 0.25 to 0.40 percent of full scale. Gage ranges were selected to be compatible with anticipated measurements. Thermocouples for measuring model temperature were premium-grade chromel-alumel thermocouple wire which is accurate to within  $\pm 2.0^\circ\text{R}$ ; the thermocouple reference-temperature junction was accurate to within  $\pm 2.0^\circ\text{R}$ .

The overall accuracy of the signal processing and recording equipment is estimated to be within  $\pm 1$  percent. Some features of the equipment that assure data accuracy are: (1) The pressure-gage data are computer compensated for reduced applied voltage at the strain-gage circuit because of line losses; (2) the pressure gages are automatically spanned with a precision resistor just before and after data are obtained as a check against any drift; and (3) the computer performs an automatic calibration of the data-conditioning equipment by using a secondary voltage standard and making any necessary corrections. This calibration also was performed on thermocouple data. (Only (2) was applied to data obtained through the remote multiplexed system.)

Heating rates were calculated from the temperature-time slope by using the one-dimensional transient heat-balance equation:

$$\dot{q}_{T,w} = (\rho c_p)_w \tau (\Delta T_w / \Delta t) \quad (1)$$

The temperature-time slope  $\Delta T_w / \Delta t$  was calculated every 1/20 sec with time steps  $\Delta t$  of 1.0 sec by using a central difference method. More sophisticated difference methods, such as a 5-point central difference approximation used in reference 19 on a model also tested in the 8-ft HTT, were not found to be any more accurate for the present tests. The wall temperature  $T_w$  of the model was generally above ambient temperature ( $540^\circ\text{R}$ ) by the time that the model got to the flow centerline and the model pressures had stabilized. (See fig. 11.) The maximum  $T_w$  reached before equation (1) could be applied was  $720^\circ\text{R}$ . (This was on the windward side at  $\alpha = 10^\circ$ .) The calculated values of the heat-transfer rate were extrapolated to the isothermal (cold) wall temperature of  $540^\circ\text{R}$  by using the following equation, based on the assumption of a constant heat-transfer coefficient:

$$\dot{q} = \dot{q}_{T,w} \frac{T_t - 540^\circ R}{T_t - T_w} \quad (2)$$

The mean combustor temperature  $T_t$  was used in place of the adiabatic wall temperature  $T_{aw}$  as a simplification; this gave a maximum error of about -1.5 percent.

The physical properties of the ogive and cone frustums are given in table V. Heating-rate errors caused by the different radii of curvature between inner and outer surfaces were estimated by the method of reference 20 to be no greater than 2.7 percent, and no corrections were made on the data. The time responses of the ogive- and cone-frustum skins were estimated to be less than the time required for model entry and flow stabilization; this means that for the times at which heating rates were calculated, the inner surface of the skin was fully responding to the heating rate. Heating-rate errors due to circumferential conduction errors in the skin were estimated, by following the procedure of reference 21, and were found to be about -1 percent at the times that the heat rates were calculated. The only significant error in calculating heating rates from the measured temperature-time rates was in conduction in the thermocouple wires. This error was estimated to be about -7 percent according to the methods of reference 22. No corrections were made for the skin and thermocouple-wire conduction errors. The aforementioned errors plus other uncertainties such as material properties, skin thickness, and so forth give a most probable (root-mean-square) overall error in measured heat-transfer rate of  $-5.8 \pm 3.1$  percent.

Shock shapes were obtained from prints of shadowgraph or schlieren images by reading the prints with a magnifying lens having precision grid marks. Errors in reading the prints are about  $\pm 5$  percent. For nose R-3, the shock shape was obtained from schlieren prints; and for the other nose configurations, measurements were made from shadowgraph prints. Because a collimated light beam was used in the test section, no relative displacement errors in shock standoff distance occurred between schlieren and shadowgraph images.

Shock-layer Mach numbers were calculated from measured static- and pitot-pressure measurements by the Rayleigh pitot formula. The survey-rake static pressures were compared with those from a precision low-pressure gage (mounted in the tunnel pod) prior to model insertion, and the pressures were accurate to within  $\pm 2$  percent. Possible sources of error for static pressures after model insertion were investigated. The first was overexpansion of the flow past the cone-cylinder shoulder of the probes. For the present probes, the orifices were six tube diameters downstream from the shoulder. Conventional design would have the orifice 10 diameters from the shoulder (ref. 23). Numerical results from reference 24 indicated that for the present probe design and Mach number range, the static pressures were, at most, 8 percent low because of overexpansion, and the error decreased with lower Mach numbers. A second possible static-pressure error is the induced pressure from the boundary-layer displacement thickness of the probe. The induced pressure was estimated from reference 23 to give a maximum pressure error of about 4 percent. The net result of the aforementioned two errors is an error in Mach number of about 2 percent. No corrections for these errors were made in the data. The error due to separation at the probe struts was not considered significant because the orifices are far (14 diameters) from the struts and the struts have a sharp edge. Thermomolecular effects (ref. 25) on static and pitot pressures were estimated but found to be negligible.

## PREDICTION METHODS

Predictions were obtained by using a series of computer codes which compute the outer inviscid flow field independent of the boundary layer. Perfect gas thermodynamic and transport properties for air at  $\gamma = 1.4$  were used in the analysis. Additional calculations were made for  $\gamma = 1.275$  and are discussed in later sections. For the nominal flow condition,  $N_{Re} = 1.4 \times 10^6$  per foot, the calculated free-stream Mach number, static pressure, and static temperature were 6.7, 0.29 psia, and 400°R, respectively. Pressures and heating rates were nondimensionalized by the stagnation-point values. The stagnation-point heating rate was calculated from the theory of Fay and Riddell (ref. 26) by using properties for methane-air combustion products. The total enthalpy (1000 Btu/lbm) used in the analysis corresponded to that for methane-air combustion products at a total temperature of 3300°R.

The first step in computing the flow about the model was to define the body geometry. This was done by using a computer code (ref. 27) which combines analytical curves to form a continuous body surface. Theoretical pressure distributions on the model were then obtained by first computing the inviscid subsonic-transonic flow over the nose of the model by using a time-asymptotic technique to integrate the three-dimensional time-dependent Euler equations (ref. 28). The solution was continued downstream where the local flow is supersonic by using a finite-difference marching technique, referred to as STEIN (supersonic three-dimensional external inviscid), to integrate the three-dimensional, steady-state Euler equations (refs. 7 and 8).

The coordinate system used in the computations is shown in figure 12. Only half of the flow field is computed, as indicated in figure 12, because of symmetry. For the R-3 and R-1 configurations, a subsonic-transonic code (ref. 28) was used from the stagnation point to  $x/r_n = 0.7$  where the axial Mach number was sufficiently supersonic. The grid specified in this region was  $11 \times 19 \times 19$  in the  $\bar{r}$ -,  $\theta$ -, and  $\varphi$ -directions, respectively. At  $x/r_n = 0.7$ , a  $11 \times 19$  point starting plane grid in the  $r$ - and  $\varphi$ -directions was specified for the supersonic inviscid solution. The grid was changed to 21 points in the  $r$ -direction at  $x/r_n = 1.5$  and to 60 points in the  $\varphi$ -direction at  $x/r_n = 2.0$ . A small amount of smoothing was applied to the inviscid calculation to ensure a smooth solution.

Heat-transfer distributions on the cone were obtained by using two separate codes for the laminar and turbulent calculations. Surface pressures and velocity vectors from the inviscid analysis were used as input to a code which calculated laminar heating rates (ref. 9) by using a method based on the axisymmetric analogue developed by Cooke (ref. 29). Boundary-layer edge properties for the heat-transfer calculation were obtained by assuming isentropic flow from the stagnation point. The inviscid velocity vectors were used to calculate streamlines and metric coefficients along the body. Heating rates were calculated along streamlines by using the axisymmetric analogue. Rather than solving the complete axisymmetric boundary-layer equations, an approximation technique described in appendix C of reference 9 was used to obtain laminar heating rates. Since these relations apply only to laminar boundary layers, a second code described in references 14 and 15 was used to calculate turbulent heating rates. This code solved the complete turbulent axisymmetric boundary-layer equations by using the edge conditions and metric coefficients obtained from the inviscid solution. Also, the code (refs. 14 and 15) was used to calculate boundary-layer thickness for both laminar and turbulent conditions.

The following two equations were used to calculate laminar- and turbulent-flow heating rates on the 12.5° cone frustum for each angle of attack by assuming a sharp

cone at an equivalent angle to the flow (i.e., no crossflow). The laminar and turbulent equations are, respectively,

$$N_{St}^* = (0.575)(N_{Pr}^*)^{-2/3}(N_{Re}^*)^{-1/2} \quad (3)$$

$$N_{St}^* = (2.25)^{1/5}(0.0296)(N_{Pr}^*)^{-2/3}(N_{Re}^*)^{-1/5} \quad (4)$$

The \* signifies that the gas properties were evaluated at Eckert's reference temperature  $T^*$ , which is given by

$$T^* = T_e + 0.50(T_w - T_e) + 0.22(T_{aw} - T_e) \quad (5)$$

and is discussed as equation (35) in chapter 13 of reference 10. The parameters  $N_{Pr}^*$  and  $N_{Re}^*$  were calculated by using oblique shock relations for methane-air combustion products. Equation (3) is presented as equation (30) in reference 11, but in the form of a Nusselt number  $N_{Nu}$ . The  $N_{St}$  is related to Nusselt number as follows:

$$N_{St} = \frac{N_{Nu}}{N_{Pr} N_{Re}}$$

The coefficient 0.575 in equation (3) includes the factor  $(3)^{1/2}$ , which is a transformation from flat plate to conical laminar-flow conditions; this factor is discussed in reference 11 and was derived in references 12 and 13. Equation (4), without the factor  $(2.25)^{1/5}$ , is presented as equation (22) in reference 11, but again in the form of Nusselt number. The factor  $(2.25)^{1/5}$ , which is a transformation from flat plate to conical turbulent-flow conditions, was derived in appendix C of reference 13.

For convenience in the present report, equations (3) and (4) are referred to as the semiempirical methods (ref. 11).

## DISCUSSION OF RESULTS

The results in the present paper consist primarily of model pressures and heating rates. However, shock shapes and shock-layer flow-field surveys were also obtained in order to characterize the flow field around the model, and these data are presented first. Next, pressure and heating-rate data are given in an overview format to characterize data trends and to make comparisons with predictions. Not all model pressure and heating data are discussed in the report; however, all model data are tabulated. The pressure data are given in table VI, and the heat-transfer data are given in table VII. Detailed results of effects of free-stream unit Reynolds number, angle of attack, nose shape, and transition location are discussed in later sections.



## Shock Flow Field

Shock shape.— Schlieren and shadowgraph photographs of the shock shape over the three nose configurations are shown in figure 13 for  $\alpha = 0^\circ$  and a nominal unit Reynolds number of  $1.4 \times 10^6$  per foot. In figure 13(a), weak shocks originating at the surface junctions are present. The shock coming off the backward-facing step at the ogive/cone junction can be seen in figures 13(b) and 13(c). A shock originating at the  $20^\circ$  frustum/ogive junction for nose R-S is seen in figure 13(c), but no shock is visible for nose R-1 (fig. 13(b)). No estimate of the effects of these junction shocks was made; but, as discussed later, pressure measurements were in good agreement with predictions, thus indicating that the shocks were weak and had little effect.

Measured and predicted shock shapes are compared in figure 14. The predictions were obtained from the codes described in references 8 and 28 by using  $\gamma = 1.4$ , which is within  $\pm 1$  percent of the free-stream  $\gamma$  for the 8-ft HTT. In general, predicted shock standoffs are in fair agreement with but exceed the measurements.

Normalized shock-standoff values are presented in figure 15 for the nose R-3 at  $\alpha = 0^\circ$ . At the stagnation point, measured shock standoff is  $x/r_n = -0.114$ . The same value was obtained for a 6-in-radius nose tested at  $M = 6.85$  in the 8-ft HTT (ref. 30). For  $\gamma = 1.4$ , the predicted value of  $-0.144$  is 26 percent greater than that measured at the stagnation point. Downstream from the stagnation point, the percentage agreement improves to about 5 percent at  $x/r_n = 2.9$ . Previous studies have shown that the shock standoff decreases for a real gas compared with an ideal gas and that normal-shock density ratios are higher for real gases. (See ref. 31, for example.) Miller (ref. 32) has shown that ideal-gas-constant  $\gamma$  inviscid codes ( $\gamma$  was kept constant in using the codes of refs. 8 and 28) can predict the shock standoff provided  $\gamma$  is calculated from the correct normal-shock density ratio. In order to approximately assess real-gas effects on shock standoff, an estimated normal-shock density ratio  $\rho_s/\rho_\infty$  of 7.12 was used in the following normal-shock equation (with  $M_\infty = 6.7$ ) to calculate a  $\gamma$  of 1.275:

$$\gamma = \frac{1 + \frac{\rho_s}{\rho_\infty} \left( 1 - \frac{2}{M_\infty^2} \right)}{\frac{\rho_s}{\rho_\infty} - 1} \quad (6)$$

Shock-standoff predictions made with  $\gamma = 1.275$  give  $x/r_n = -0.109$  at the stagnation point, which is within  $\pm 4$  percent of the measured value. As shown in figure 15, the predicted shock-standoff distance for  $\gamma = 1.275$  is in excellent agreement with measured values downstream of the stagnation point. This agreement in shock standoff using a lower  $\gamma$  is consistent with the fact that although the free-stream  $\gamma$  in the 8-ft HTT is close to 1.4 (about 1.38), real-gas effects cause a lower  $\gamma$  in the stagnation-region shock layer.

Flow-field surveys.— Flow-field survey results are presented in figures 16, 17, and 18. In figures 16 and 17 the Mach number is plotted as a function of the distance normal to the cone surface for three rake locations with the model at  $\alpha = 0^\circ$  for noses R-3 and R-1, respectively. Measurements are compared with corresponding predictions for the STEIN code (ref. 8) for  $\gamma = 1.4$  and 1.275. The measured Mach numbers were obtained from the Rayleigh pitot formula by using the measured ratio of

static pressure to pitot pressure. Data in figure 16 were calculated only for  $\gamma = 1.4$ . The effect of  $\gamma = 1.275$  on the data can be seen in figure 17. Estimates of boundary-layer thicknesses at the rake locations were obtained from boundary-layer calculations by using the method described in reference 15. (In the present estimates, turbulent flow was assumed to start at the stagnation point.) In general, the Mach number data agree best with the lower  $\gamma$  predictions from STEIN.

The measured data at  $\eta = 1.75$  in. appear to be diverging from the predictions. (See fig. 16(a).) For nose R-3, pitot-pressure data obtained at  $s_c = 14.8$  in. (run 5 data) without the cover plate were about 11 percent lower at  $\eta = 1.75$  in.; this reduced the Mach number by about 6 percent. (Static pressures from run 4 with the cover plate were used.) This suggests that the cover plate did cause a small flow disturbance on the probes at  $\eta = 1.75$  in. However, this flow disturbance does not fully explain the divergence of the Mach number data from the predictions. Cleary (ref. 33) predicted peaks (which exceed sharp-cone values) in total pressure and Mach number in the shock layer for blunt cones due to overexpansion effects in the shock layer. He also measured pitot-pressure peaks. It is speculated that the present data at  $\eta = 1.75$  in. are indicative of such peaks, which were not predicted by STEIN.

The results in figure 16 for the Reynolds number ranges indicate that the Mach number profiles are independent of Reynolds number over the range tested. A comparison between the R-3 and R-1 results (figs. 16 and 17, respectively) shows lower Mach numbers near the cone (with nose R-3) surface because of higher entropy effects of the blunter nose.

As will be shown later from the heating data, the boundary layers at rakes 1, 2, and 3 were laminar, transitional, and transitional, respectively, for nose R-3; and transitional, transitional, and turbulent, respectively, for nose R-1. This information, together with boundary-layer thickness estimates noted in figures 16 and 17, indicates that the probes at  $\eta = 0.2$  in. for the third rake were well into a turbulent boundary layer.

The corresponding total-temperature profiles at  $\alpha = 0^\circ$  are presented in figure 18 with the measured temperature normalized by the combustor total temperature. The profiles are flat at  $T/T_t = 1.0$  except near the model surface, which indicates that no appreciable loss occurred in total temperature in the shock layer for either nose bluntness.

### Pressure Distributions

The pressure distributions normalized to stagnation values for three runs with nose R-3 for identical conditions at  $\alpha = 0^\circ$  are given in figure 19. These data show the good repeatability in longitudinal and circumferential pressure distributions obtained in the present tests. Measured and predicted longitudinal and circumferential pressure distributions are given for the three nose configurations at  $N_{Re} = 1.4 \times 10^6$  per foot (nominal value) in figures 20, 21, and 22. On the windward ray,  $\phi = 0^\circ$ , the predictions from STEIN (ref. 8) are in agreement with the data for all three nose shapes for the present range of angle of attack. Data on the windward ray converge to the sharp-cone values (ref. 34) for  $\gamma = 1.4$ . All predictions shown from STEIN are for  $\gamma = 1.4$ , except for one prediction using  $\gamma = 1.275$  (fig. 20(a) with  $\phi = 0^\circ$ ) which gave lower pressures by up to 10 percent when compared with  $\gamma = 1.4$  values. From the limited pressure data obtained on the leeward ray,  $\phi = 180^\circ$ , it appears that the STEIN code (ref. 8) overpredicted the pressure

immediately downstream of the nose and predicted the measured pressures near the rear of the cone to within experimental accuracy.

The longitudinal pressure distributions for noses R-1 and R-S, shown in figures 21(a) and 22(a), respectively, indicate the same trends as figure 20(a). The STEIN code predicts the data for nose R-1 better at  $\alpha = 0^\circ$  and  $5^\circ$  than at  $\alpha = 10^\circ$ , where STEIN overpredicts the pressure with increasing error down the length of the model. The probable reason is that as the entropy layer thins, far downstream of the stagnation point, sufficient points cannot be kept in the entropy layer. The version of STEIN used in the analysis does not adjust or cluster the grid spacing, and increasing the number of grid points to improve accuracy would have been cumbersome. The data shown in figure 22 for nose R-S are compared with predictions from the STEIN code for nose R-1.

Circumferential pressures for nose R-3 are shown in figure 20(b) at two longitudinal stations. The uniform distributions at  $\alpha = 0^\circ$  at both stations indicate that the model was in alignment with the tunnel flow. The STEIN code predicted the pressures except near the leeward side for  $\alpha = 5^\circ$  and  $10^\circ$ . For noses R-1 and R-S, circumferential pressure distributions similar to those for nose R-3 are shown in figures 21(b) and 22(b), respectively.

#### Heating-Rate Distributions

The cold-wall heating rates were normalized by the calculated stagnation-point heating rate obtained by the method of Fay and Riddell (ref. 26). For the R-S (sharp) nose configuration, the local heating rates were normalized by the stagnation value of the 1-in-radius nose. Laminar heating rates are compared with the theory of Hamilton (ref. 9), and turbulent heating rates are compared with the method of reference 15 and with the semiempirical turbulent method described in reference 11. Sharp-cone pressures were used in this method since the purpose of comparison was to establish the magnitude of turbulent heating. The detailed results of free-stream unit Reynolds number, angle of attack, nose shape, and transition location are discussed in later sections.

Heat-transfer data are given in table VII and windward-side data are presented in figures 23 to 26 for the three model configurations at the highest Reynolds number test condition,  $N_{Re} = 1.4 \times 10^6$  per foot (nominal value), and at angles of attack of  $0^\circ$ ,  $2.5^\circ$ ,  $5^\circ$ , and  $10^\circ$ . The heating distributions for three runs with nose R-3 at identical conditions at  $\alpha = 0^\circ$  are given in figure 23. The longitudinal distributions in figure 23(a) repeat for the three runs and show that transitional flow is experienced at this condition.

Circumferential heating distributions at  $s = 65.95$  in., where the boundary layer is transitional, are generally repeatable for a range of  $\varphi$  from  $-68.5^\circ$  to  $112.5^\circ$ , which is behind the two retracted rakes indicated in the figure by the arrows. However, the heating varied over the rest of the model for the three runs, thus indicating a randomness of the beginning of transition. Also, note that the increased heating level behind rake 1 ( $\varphi = -45^\circ$ ,  $s = 23.5$  in.) extends over a broader area than that for rake 2 ( $\varphi = 90^\circ$ ,  $s = 47.0$  in.). The indicated spreading effect with longitudinal distance is characteristic of the turbulent wedge produced by tripping of the flow by the retracted rakes. A rake assembly, even when retracted, provided enough of a disturbance to trip the flow, probably because of surface roughness from the screwheads and the beveled leading edge of the cover plate

that formed a spanwise rearward-facing step. Mass flow rates through the rake-assembly gaps (see fig. 5) due to possible venting were estimated by using pressure data, but no pattern of blowing or suction was found that indicated venting was the reason the retracted rakes tripped the flow.

The method of Hamilton (ref. 9) is in good agreement with the laminar data for  $\alpha = 0^\circ$ , as seen in figure 24(a) for nose R-3. At  $\alpha = 10^\circ$  the flow at the rear of the cone was fully turbulent, as shown in figures 24(a) and 24(d); the semiempirical turbulent method predicted the turbulent heating levels within about 15 percent. However, the turbulent method of reference 15 considerably underpredicted the turbulent heating levels. None of the aforementioned three prediction methods include entropy swallowing in the boundary layer. Lack of entropy swallowing will result in underprediction of heating, and greater errors will occur in turbulent flow than in laminar flow. Experimental turbulent heating data for a tangent ogive at Mach 6, when compared with predictions (presented in ref. 35), indicated that neglecting entropy swallowing resulted in an error of about -35 percent, but including entropy swallowing reduced the error to -15 percent or less. Thus, it is possible that lack of entropy swallowing may account for the underprediction by the turbulent method of reference 15. Similar measured longitudinal heating trends for noses R-1 and R-S are seen in figures 25(a) and 26(a), respectively. The laminar theory of Hamilton is in good agreement with the laminar heating data over the ogive portions of these configurations. For nose R-S, the laminar heating prediction shown is for nose R-1.

Circumferential heating distributions for nose R-3 are shown in figures 24(b) to 24(d). The semiempirical method (ref. 11) was used to indicate the level of turbulent heating expected. The circumferential distributions at  $\alpha = 0^\circ$  for three body stations are shown in figure 24(b); at  $s = 16.87$  in. the heating corresponds to laminar flow around the body and is in good agreement with the method of Hamilton (ref. 9). Additional angle-of-attack data and further discussion are given in a subsequent section entitled "Effects of Angle of Attack."

#### Effects of Reynolds Number

The effects of free-stream unit Reynolds number on the pressure and heating are shown in figure 27 for  $\alpha = 0^\circ$ . As seen in figure 27(a) at  $\varphi = 0^\circ$ , both the normalized longitudinal pressure data and the normalized laminar heating data are independent of Reynolds number, and transition moves forward with increasing Reynolds number. The circumferential pressure distribution is independent of Reynolds number, as shown for  $s = 66.73$  in. in figure 27(b). However, the circumferential heating distribution shows that the lowest Reynolds number (thicker) boundary layer is less sensitive to tripping by the retracted rakes, as seen where rake 1 did not trip the boundary layer at  $\varphi = -45^\circ$ .

In figure 28, the longitudinal heating-rate distributions at  $\alpha = 10^\circ$  for two Reynolds numbers are presented for nose R-3. The location of the start of transition on the windward plane,  $\varphi = 0^\circ$ , moves forward with increasing Reynolds number as transition did for  $\alpha = 0^\circ$ . On the leeward side,  $\varphi = 180^\circ$ , the location of transition moves forward for the higher Reynolds number but not to the same extent as on the windward side.

## Effects of Angle of Attack

Pressure data.— The effects of angle of attack on the windward pressure are shown in figures 20(a), 21(a), and 22(a) for the three nose shapes. As the angle of attack is increased, the measured pressure distribution reaches the sharp-cone predictions (ref. 34) closer to the nose of the model, thus indicating that the flow overexpansion at the nose decreases with increasing  $\alpha$ . On the leeward side,  $\varphi = 180^\circ$ , of the model not enough data were obtained to define the pressure distribution.

The circumferential pressure distributions for noses R-3 and R-1 show a gradient reversal near the leeward side at the highest angle of attack near the base. (See figs. 20(b) and 21(b), respectively.) The cause of the reversal is not known but there are three possibilities: (1) The base pressure was higher than the most rearward cone pressure on the leeward side, except for run 10 which was the lowest Reynolds number run. The high base-pressure conditions can be seen by a comparison of base pressure and most leeward surface (P25) pressures in table VI(c); this high base pressure could cause the increased pressure at  $\varphi = 180^\circ$ . (2) At angle of attack the flow overexpanded to a minimum pressure and then recovered at the most leeward ray,  $\varphi = 180^\circ$ . The pressure data from Stetson (ref. 36) for a sharp  $5.6^\circ$  half-angle cone at  $\alpha = 2^\circ$  showed a minimum in pressure at about  $\varphi = 160^\circ$  prior to any flow separation. Rakich and Cleary (ref. 37) indicate that inviscid calculations for blunt cones predict a pressure minimum near  $\varphi = 150^\circ$  with a recompression of the flow approaching  $\varphi = 180^\circ$  even for an angle of attack greater than the cone half-angle. The minimum pressure for  $\varphi$  less than  $180^\circ$  predicted by the STEIN code is probably qualitatively correct but not accurate because of likely numerical limitations at the low pressures on the leeward side (ref. 37), and because the flow field is influenced more by viscous effects on the leeward side than on the windward side. (3) The most likely possibility for the pressure increase at  $\varphi = 180^\circ$  is flow separation with subsequent reattachment. Separation has been observed on slender sharp cones at angles of attack less than the body half-angle (ref. 36). However, pressure data by itself are not sufficient to verify separation.

Heating data.— Figure 29 presents the longitudinal distributions of heating for noses R-3 and R-1 for three angles of attack. The effect of angle of attack on the longitudinal heating distribution on the windward side is to move the start of transition forward. This effect can be seen for noses R-3 and R-1 in figures 29(a) and 29(b), respectively, and for nose R-S in figure 26(a). The forward movement of transition for the R-3 nose shape was greater than for the R-1 nose shape between  $\alpha = 0^\circ$  and  $5^\circ$ , whereas the movement for  $\alpha = 5^\circ$  to  $10^\circ$  was about the same. Similar trends are seen on the leeward side, although angle of attack does not affect the movement of transition as much. The possible effect of flow separation and reattachment heating on the leeward ray,  $\varphi = 180^\circ$ , at  $\alpha = 10^\circ$  can be seen in figure 29(b) past  $s = 65$  in., where the heating data increase above the apparent fully turbulent level established between  $s = 35$  and  $65$  in. For this run (run 14), the base pressure was higher than the cone pressure on the leeward side at the rear of the model (see table VI(c)), and the high base pressure could have caused separated flow with possible reattachment. It is not known if the high base pressure led to the observed increase in heating since separation and reattachment can also be related to angle of attack independently of base pressure. (See ref. 36.) However, it is well-known that reattachment of separated flow increases the heating along the reattachment line.

## Effects of Nose Shape

The effects of nose shape on the longitudinal and circumferential pressure and heating distributions are presented in figures 30 to 33 for the nominal test condition at  $N_{Re} = 1.4 \times 10^6$  per foot. The data are plotted against  $s_c$ , which is the surface distance measured from the start of the cone frustum, to align all the data stations. The longitudinal normalized pressure distributions for all three model configurations are presented in figure 30. Increased bluntness delayed the model pressures from reaching the sharp-cone values because of overexpansion of the flow from the model nose as the flow adjusted to the cone section. The results presented in figure 31 show that the effect of nose shape on the circumferential pressure distribution decreased with increasing distance from the nose.

The effects of nose shape on the longitudinal heating distribution are presented in figure 32 in which the measured values are normalized by the calculated stagnation value for  $r_n = 1$  in. The actual magnitudes of the laminar and turbulent heating rates at given stations were independent of nose shape except on the leeward side. The most prominent effect of increasing bluntness is to move the start of transition rearward. This movement of transition location for an angle of attack greater than  $0^\circ$  is more sensitive to nose shape on the leeward side than on the windward side. The precise start of transition is difficult to determine for nose R-S at  $\alpha = 10^\circ$ , since it apparently occurred very near the sharp tip. The steplike increase in leeward heating that occurs near the base for all three nose shapes was probably due to reattachment of separated flow as discussed earlier.

The circumferential heating distributions, shown in figure 33, indicate that at  $\alpha = 0^\circ$  the boundary layer is turbulent for the R-S and R-1 nose shapes and transitional for the R-3 nose shape. The distribution for nose R-3 illustrates the effects of the rake cover plate in tripping the flow. From the distribution at  $\alpha = 10^\circ$ , it appears that only a narrow band near  $\varphi = 180^\circ$  was affected by the variation in nose bluntness. Apparently, the nose shape significantly affected the structure of the leeward flow, thus causing the differences in surface heating seen in figure 33(b).

The longitudinal heating distribution on the ogive frustum for both noses R-1 and R-S is given at three circumferential locations in figure 34. At  $\alpha = 0^\circ$  (fig. 34(a)), the longitudinal heating is independent of  $\varphi$ , which indicates true zero angle of attack. At  $\alpha = 10^\circ$  (fig. 33(b)), the longitudinal heating for noses R-1 and R-S agrees for both  $\varphi = 0^\circ$  and  $\varphi = -90^\circ$ . However, for  $\varphi = 180^\circ$  (the most leeward ray), the data diverge down the length of the ogive because of transitional flow for nose R-S, whereas the boundary layer for nose R-1 remains laminar.

Longitudinal laminar and turbulent heating data for the R-S and R-1 nose shapes are presented in terms of  $N_{St}^*$  plotted against  $N_{Re}^*$  in figure 35 at  $\alpha = 0^\circ$  for the purpose of comparing with similar data from reference 3. (The two dashed-line curves represent the band of data from ref. 3.) Overall agreement of the present data with data from reference 3 is good for the laminar and fully turbulent heating levels. The present fully turbulent data are lower than the corresponding prediction curve by about 15 percent, whereas the data of reference 3 show better agreement. The present laminar data are lower than the corresponding prediction curve by about 17 percent and are in agreement with the data of reference 3. The difference in the ratio of wall temperature to total temperature and in the free-stream unit Reynolds numbers between the present and the test conditions of reference 3 is accounted for by the correlation method.

## Location of Start of Transition

Several investigators have studied the effect of angle of attack on transition. (For example, see refs. 1 to 3.) However, the question of transition movement with angle of attack still appears to be open. Based on the general agreement between theory and experiment among researchers, Stetson (ref. 1) indicated that increasing the angle of attack for a sharp cone causes a rearward movement of transition on the windward ray and a forward movement on the leeward ray. However, the effect that nose bluntness has on transition movement with angle of attack has not been well established. As noted earlier, the effects of increasing angle of attack and decreasing nose bluntness resulted in moving transition forward on the model for the present data. These effects are summarized in figure 36 in a form used in other studies. The location of the start of transition (surface distance from the stagnation point) normalized by the start of transition for a sharp tip at  $\alpha = 0^\circ$  is plotted against angle of attack. In this figure, an increasing value of normalized  $s_{tr}$  means a rearward movement of the start of transition.

The present data are given in figure 36(a), and the data from references 1, 2, and 3 are given in figures 36(b), (c), and (d), respectively. The present sharp-nose data of figure 36(a) indicate that transition moved forward with angle of attack on both the windward and leeward sides of the model. The data from all three references shown in figure 36 agree with this trend for the leeward side, but they do not agree for the windward side. The present data may differ from the other data because of a bluntness effect of the ogive frustum even though the tip was sharp. All blunt data in figure 36 show, in general, that increasing bluntness moves transition rearward on both the windward and leeward sides. The present data on the windward side at  $\alpha = 10^\circ$  show little effect of bluntness; this is in contrast to the data in figures 36(b) and 36(d), but in agreement with figure 36(c). The blunt leeward-side data of references 1 to 3 show that transition moves forward as angle of attack increases; however, the trend of the present data is significantly more gradual than the other data.

Overall, the movement of transition on the windward side with increasing angle of attack does not show a consistent trend among the four sets of blunt data in figure 36. The present data trends of forward movement are in general agreement with data from references 1 and 2 at larger angles of attack, but in disagreement with data from reference 3. Stetson's data (ref. 1) on the windward side is in disagreement with his earlier data (ref. 2); moreover, he was unable in reference 1 to explain the difference. Muir and Trujillo (ref. 3) questioned the validity of the data from reference 2 (fig. 36(c)) on the basis of incorrect interpretation (by Stetson) of the start of transition. Their data (fig. 36(d)) show a general rearward movement of transition on the windward side.

It has been well established that the start of transition is influenced by tunnel noise. Yet, it is not clear if tunnel noise could be responsible for the disagreement in data shown in figure 36. Clearly, additional data are needed to resolve the windward-side movement of the transition dilemma.

## CONCLUDING REMARKS

A  $12.5^\circ$  half-angle cone having a 3-ft-base diameter was tested in the Mach 6.7 stream of the Langley 8-Foot High-Temperature Tunnel at angles of attack from  $0^\circ$  to  $10^\circ$ . The total temperature was  $3300^\circ\text{R}$ , and nominal free-stream unit Reynolds

numbers ranged from  $0.4 \times 10^6$  to  $1.4 \times 10^6$  per foot. Three nose configurations were tested on the cone: a 3-in-radius tip, a 1-in-radius tip on an ogive frustum, and a sharp tip on an ogive frustum. Cold-wall (ratio of wall temperature to total temperature of 0.16) heating-rate distributions, surface-pressure distributions, shock shapes, and shock-layer profiles were measured and compared with predictions.

Shock-shape predictions by inviscid flow-field codes using a ratio of specific heats  $\gamma$  of 1.4 showed fair agreement with measured shock shapes. Agreement was shown to improve to within  $\pm 4$  percent in the stagnation region by using a lower  $\gamma$  of 1.275 to account for real-gas effects. The shock-layer Mach number profiles, which were independent of free-stream Reynolds number, showed trends and levels that were generally in agreement with predictions. Better agreement was obtained for  $\gamma = 1.275$  than for  $\gamma = 1.4$ . Measured shock-layer temperature profiles indicated good total-temperature recovery within the shock layer.

Surface pressures normalized by the stagnation pressure behind a normal shock were independent of free-stream Reynolds number, for the present flow conditions, and required longer distances to recover to sharp-cone pressures as the nose bluntness increased. Windward pressure distributions were predicted to within experimental accuracy for the present range of angle of attack.

The cold-wall heating data indicated that laminar, transitional, and turbulent boundary layers were experienced in the present study. Laminar heating data normalized by calculated stagnation-point heat transfer were independent of free-stream unit Reynolds number. Laminar heating on the ogive frustum was independent of nose bluntness up to  $90^\circ$  off the windward ray for angles of attack up to  $10^\circ$ . Good agreement between measured and predicted laminar heating was observed on the windward side of the model ( $\pm 90^\circ$  from the most windward ray) over the present range of angle of attack. Turbulent heating levels were in agreement with a semiempirical method. The location of the start of transition moved forward, both on the windward and leeward sides, with increasing free-stream Reynolds number, increasing angle of attack, and decreasing nose bluntness. A comparison of these trends with those from other studies showed general agreement on the leeward side but not on the windward side. However, disagreement on the windward side is not surprising since different trends of windward-side transition movement exist among the other studies.

Langley Research Center  
National Aeronautics and Space Administration  
Hampton, VA 23665  
September 27, 1984



## REFERENCES

1. Stetson, Kenneth F.: Hypersonic Boundary Layer Transition Experiments. AFWAL-TR-80-3062, U.S. Air Force, Oct. 1980. (Available from DTIC as AD A093 819.)
2. Stetson, Kenneth F.; and Rushton, George H.: Shock Tunnel Investigation of Boundary-Layer Transition at  $M = 5.5$ . AIAA J., vol. 5, no. 5, May 1967, pp. 899-906.
3. Muir, James F.; and Trujillo, Amado A.: Experimental Investigation of the Effects of Nose Bluntness, Free-Stream Unit Reynolds Number, and Angle of Attack on Cone Boundary Layer Transition at a Mach Number of 6. AIAA Paper No. 72-216, Jan. 1972.
4. Stultz, J. W.; and Paul, D. B.: Results of a Government and Industry Survey of the Heating Methods Used To Determine Missile Structural Temperatures. Paper 80-ENAS-26, American Soc. Mech. Eng., July 1980.
5. Nestler, D. E.: Hypersonic Laminar Heat Transfer to Cones at Angle of Attack. Heat Transfer 1978, Volume 5, Hemisphere Pub. Corp., 1978, pp. 215-220.
6. Miller, C. G.; Gnoffo, P. A.; and Micol, J. R.: Heat-Transfer Distributions for Biconics at Incidence in Hypersonic-Hypervelocity Real-Gas Flows. Paper presented at the 14th International Symposium on Shock Tubes and Waves (Sydney, Australia), Aug. 1983.
7. Marconi, Frank; Salas, Manuel; and Yaeger, Larry: Development of a Computer Code for Calculating the Steady Super/Hypersonic Inviscid Flow Around Real Configurations. Volume I - Computational Technique. NASA CR-2675, 1976.
8. Marconi, Frank; and Yaeger, Larry: Development of a Computer Code for Calculating the Steady Super/Hypersonic Inviscid Flow Around Real Configurations. Volume II - Code Description. NASA CR-2676, 1976.
9. Hamilton, H. Harris, II: Calculation of Laminar Heating Rates on Three-Dimensional Configurations Using the Axisymmetric Analogue. NASA TP-1698, 1980.
10. Kays, W. M.: Convective Heat and Mass Transfer. McGraw-Hill Book Co., Inc., c.1966.
11. Johnson, H. A.; and Rubesin, M. W.: Aerodynamic Heating and Convective Heat Transfer - Summary of Literature Survey. Trans. ASME, vol. 71, no. 5, July 1949, pp. 447-456.
12. Hantsche and Wendt: The Laminar Boundary Layer on a Circular Cone at Zero Incidence in a Supersonic Stream. Repts. and Translations No. 276, British M.A.P. Völkenrode, Aug. 1946. (Translated from Jahrbuch der deutsche Luftfahrtforschung, pt. 1, 1941, pp. 76-77.)
13. Gazley, C., Jr.: Theoretical Evaluation of the Turbulent Skin-Friction and Heat Transfer on a Cone in Supersonic Flight. Rep. No. R49A0524, General Electric Co., Nov. 1949.

14. Anderson, E. C.; and Lewis, C. H.: Laminar or Turbulent Boundary-Layer Flows of Perfect Gases or Reacting Gas Mixtures in Chemical Equilibrium. NASA CR-1893, 1971.
15. Miner, E. W.; Anderson, E. C.; and Lewis, Clark H.: A Computer Program for Two-Dimensional and Axisymmetric Nonreacting Perfect Gas and Equilibrium Chemically Reacting Laminar, Transitional and/or Turbulent Boundary Layer Flows. VPI-E-71-8, May 1971. (Available as NASA CR-132601.)
16. Deveikis, William D.; and Hunt, L. Roane: Loading and Heating of a Large Flat Plate at Mach 7 in the Langley 8-Foot High-Temperature Structures Tunnel. NASA TN D-7275, 1973.
17. Leyhe, E. W.; and Howell, R. R.: Calculation Procedure for Thermodynamic, Transport, and Flow Properties of the Combustion Products of a Hydrocarbon Fuel Mixture Burned in Air With Results for Ethylene-Air and Methane-Air Mixtures. NASA TN D-914, 1962.
18. Gardner, James E.; and Dixon, S. C.: Loads and Aeroelasticity Division Research and Technology Accomplishments for FY 1983 and Plans for FY 1984. NASA TM-85740, 1984.
19. Avery, Don E.; Kerr, Patricia A.; and Wieting, Allan R.: Experimental Aerodynamic Heating to Simulated Shuttle Tiles. AIAA-83-1536, June 1983.
20. Whitehead, Allen H., Jr.; and Dunavant, James C.: A Study of Pressure and Heat Transfer Over an 80° Sweep Slab Delta Wing in Hypersonic Flow. NASA TN D-2708, 1965.
21. George, A. R.; and Reinecke, W. G.: Conduction in Thin-Skinned Heat Transfer and Recovery Temperature Models. AIAA J., vol. 1, no. 8, Aug. 1963, pp. 1956-1958.
22. Larson, M. B.; and Nelson, E.: Variables Affecting the Dynamic Response of Thermocouples Attached to Thin-Skinned Models. Trans. ASME, Ser. C: J. Heat Transfer, vol. 91, no. 1, Feb. 1969, pp. 166-168.
23. Behrens, Wilhelm: Viscous Interaction Effects on a Static Pressure Probe at  $M = 6$ . AIAA J., vol. 1, no. 12, Dec. 1963, pp. 2864-2866.
24. Clippinger, R. F.; Giese, J. H.; and Carter, W. C.: Tables of Supersonic Flows About Cone Cylinders. Part I: Surface Data. Rep. No. 729, Ballistic Res. Labs., Aberdeen Proving Ground, July 1950.
25. Arney, G. D., Jr.; and Bailey, A. B.: Effect of Temperature on Pressure Measurements. AIAA J., vol. 1, no. 12, Dec. 1963, pp. 2863-2864.
26. Fay, J. A.; and Riddell, F. R.: Theory of Stagnation Point Heat Transfer in Dissociated Air. J. Aeronaut. Sci., vol. 25, no. 2, Feb. 1958, pp. 73-85, 121.
27. Vachris, Alfred F., Jr.; and Yaeger, Larry S.: QUICK-GEOMETRY - A Rapid Response Method for Mathematically Modeling Configuration Geometry. Applications of Computer Graphics in Engineering, NASA SP-390, 1975, pp. 49-73.

28. Moretti, Gino; and Bleich, Gary: Three-Dimensional Flow Around Blunt Bodies. AIAA J., vol. 5, no. 9, Sept. 1967, pp. 1557-1562.
29. Cooke, J. C.: An Axially Symmetric Analogue for General Three-Dimensional Boundary Layers. R. & M. No. 3200, British A.R.C., 1961.
30. Weinstein, Irving: Heat-Transfer and Pressure Distributions on Hemisphere-Cylinders in Methane-Air Combustion Products at Mach 7. NASA TN D-7104, 1973.
31. Balakrishnan, A.; Davy, W. C.; and Lambard, C. K.: Real Gas Flow Fields About Three Dimensional Configurations. AIAA-83-0581, Jan. 1983.
32. Miller, Charles G., III: Measured Pressure Distributions, Aerodynamic Coefficients, and Shock Shapes on Blunt Bodies at Incidence in Hypersonic Air and  $CF_4$ . NASA TM-84489, 1982.
33. Cleary, Joseph W.: An Experimental and Theoretical Investigation of the Pressure Distribution and Flow Fields of Blunted Cones at Hypersonic Mach Numbers. NASA TN D-2969, 1965.
34. Ames Research Staff: Equations, Tables, and Charts for Compressible Flow. NACA Rep. 1135, 1953. (Supersedes NACA TN 1428.)
35. DeJarnette, Fred R.: Aerodynamic Heating on Complex Configurations. Technical Papers - Conference on Advanced Technology for Future Space Systems, May 1979, pp. 179-188. (Available as AIAA Paper 79-0891.)
36. Stetson, Kenneth F.: Boundary-Layer Separation on Slender Cones at Angle of Attack. AIAA J., vol. 10, no. 5, May 1972, pp. 642-648.
37. Rakich, John V.; and Cleary, Joseph W.: Theoretical and Experimental Study of Supersonic Steady Flow Around Inclined Bodies of Revolution. AIAA Paper No. 69-187, Jan. 1969.

TABLE I.- LOCATION OF THERMOCOUPLES<sup>a</sup> ON MODEL

Thermocouple locations at circumferential positions $\varphi$ of -																$s_c$ in., for -		$s$ , in., for -			
-180.0°	-157.5°	-135.0°	-112.5°	-90.0°	-67.5°	-45.0°	-22.5°	0°	22.5°	45.0°	67.5°	90.0°	112.5°	135.0°	157.5°	180.0°	12.5° cone	Nose R-3	Nose R-1	Nose R-S	
Ogive nose frustum																					
T142									T126							T142			3.19	4.51	
T143									T127							T143			4.21	5.53	
T144									T128							T144			5.32	6.64	
T145									T129							T145			6.19	7.51	
T146									T130							T146			7.25	8.57	
T147									T131							T147			8.30	9.62	
T148									T132							T148			9.37	10.69	
T149									T133							T149			10.42	11.74	
12.5° cone frustum																					
T51																	$b_0$	$b_{8.73}$	$b_{12.07}$	$b_{13.39}$	
T52									T1								T51	.81	9.54	12.88	14.20
T53									T2								T52	1.81	10.54	13.88	15.20
T54									T3								T53	3.91	12.64	15.98	17.30
T55									T4								T54	6.16	14.89	18.23	19.55
T56									T5								T55	8.14	16.87	20.21	21.53
T57									T6								T56	10.38	19.11	22.45	23.77
T58									T7								T57	12.91	21.64	24.98	26.30
T59									T8								T58	15.38	24.11	27.45	28.77
T60									T9								T59	17.94	26.67	30.01	31.33
T61									T10								T60	22.88	31.61	34.95	36.27
T62									T11								T61	26.23	34.96	38.30	39.62
T63									T12								T62	29.66	38.39	41.73	43.05
T64									T13								T63	35.81	44.54	47.88	49.20
T65									T14								T64	38.85	47.58	50.92	52.24
T66									T15								T65	40.69	49.42	52.76	54.08
T67									T16								T66	47.31	56.04	59.38	60.70
T68									T17								T67	49.79	58.52	61.86	63.18
T69									T18								T68	51.75	60.48	63.82	65.14
T70									T19								T69	57.22	65.95	69.29	70.61
																	T70	60.31	69.04	72.38	73.70

<sup>a</sup>Thermocouple numbers are designed by the notation "T\_\_".<sup>b</sup>Start of cone frustum.

TABLE II.- LOCATION OF PRESSURE ORIFICES<sup>a</sup>

## (a) Nose tips

Orifice	$\phi$ , deg	$\theta$ , deg	s, in.	Nose
P31	0	0	0	R-1
P32	0	0	0	R-3
P33	-58	25	1.31	R-3
P34	-58	50	2.62	R-3
P35	-58	77.5	4.06	R-3
P36	-58		6.26	R-3
P37	122	-77.5	4.06	R-3
P38	122		6.26	R-3

## (b) 12.5° cone frustum

Orifice	$\phi$ , deg	$s_c$ , in., for -	s, in., for -		
		12.5° cone	Nose R-3	Nose R-1	Nose R-S
P1	0	0.73	9.46	12.80	14.12
P2	0	2.83	11.56	14.90	16.22
P3	0	5.03	13.76	17.10	18.42
P4	0	7.03	15.76	19.10	20.42
P5	0	9.06	17.79	21.13	22.45
P6	0	11.60	20.33	23.67	24.99
P7	0	14.14	22.87	26.21	27.53
P8	0	16.52	25.25	28.59	29.91
P9	0	18.90	27.63	30.97	32.29
P10	0	24.38	33.11	36.45	37.77
P11	0	27.79	36.52	39.86	41.18
P12	0	31.23	39.96	43.30	44.62
P13	0	36.70	45.43	48.77	50.09
P14	0	42.62	51.35	54.69	56.01
P15	0	48.12	56.85	60.19	61.51
P16	0	52.64	61.37	64.71	66.03
P17	0	58.00	66.73	70.07	71.39
P18	0	62.19	70.92	74.26	75.58
P19	45	9.06	17.79	21.13	22.45
P20	90	9.06	17.79	21.13	22.45
P21	90	58.00	66.73	70.07	71.39
P22	135	9.06	17.79	21.13	22.45
P23	135	58.00	66.73	70.07	71.39
P24	180	9.06	17.79	21.13	22.45
P25	180	58.00	66.73	70.07	71.39
P26	-135	9.06	17.79	21.13	22.45
P27	-90	9.06	17.79	21.13	22.45
P28	-90	58.00	66.73	70.07	71.39
P29	-45	9.06	17.79	21.13	22.45
P30	-45	58.00	66.73	70.07	71.39

<sup>a</sup>Pressure-orifice numbers are designated by the notation "P\_\_."

TABLE III.- RUN NUMBERS FOR NOMINAL TEST CONDITIONS

$\alpha$ , deg	Run numbers for noses at $N_{Re}$ per foot of -				
	$0.4 \times 10^6$	$0.9 \times 10^6$	$1.4 \times 10^6$	$1.4 \times 10^6$	
	Nose R-3			Nose R-1	Nose R-S
0	7	6	1, 2, 3, 4, 5	11, 12	15, 16
2.5				13	
5			8		
10	10		9	14	17

TABLE IV.- TEST CONDITIONS

Test	Run	Model test time, sec	T <sub>t</sub> , °R	N <sub>Re</sub> , ft <sup>-1</sup>	M	p <sub>s</sub> , psia	$\dot{q}_s$ , Btu/ft <sup>2</sup> -sec	$\alpha$ , deg
Nose R-3								
98-4	a <sub>1</sub>	10	3320	1.42 × 10 <sup>6</sup>	6.7	17.95	79.4	0
98-7	a <sub>2</sub>	15	3460	1.34	6.8	18.10	82.4	0
98-8	3	40	3260	1.45	6.6	17.80	74.6	0
98-9	a <sub>4</sub>	4	3430	1.36	6.8	18.00	80.8	0
98-10	a <sub>5</sub>	4	3450	1.35	6.8	18.10	82.0	0
98-6	a <sub>6</sub>	40	3320	.88	6.9	10.74	59.6	0
98-5	7	40	3170	.40	6.8	4.75	36.6	0
98-11	8	30	3230	1.46	6.6	18.00	74.0	5
98-12	9	15	3180	1.48	6.6	18.27	72.8	10
98-13	10	40	3030	.42	6.7	4.74	33.6	10
Nose R-1								
98-14	11	25	3250	1.45 × 10 <sup>6</sup>	6.6	17.92	129.2	0
98-17	a <sub>12</sub>	4	3050	1.51	6.4	17.80	115.0	0
98-15	13	25	3380	1.41	6.7	18.1	133.4	2.5
98-16	14	15	3180	1.47	6.6	18.16	126.1	10
Nose R-S								
98-18	15	5	3110	1.50 × 10 <sup>6</sup>	6.5	17.96	<sup>b</sup> 119.9	0
98-19	16	15	3520	1.29	6.8	17.65	<sup>b</sup> 143.8	0
98-21	17	10	3430	1.35	6.8	17.84	<sup>b</sup> 139.6	10

<sup>a</sup>Survey-rake data obtained.<sup>b</sup>Values for nose R-1.

TABLE V.- PHYSICAL PROPERTIES OF OGIVE-FRUSTUM AND  
12.5° CONE-FRUSTUM SKINS

Physical property	Ogive frustum	12.5° cone frustum
Material . . . . .	Stainless steel	René 41
Thickness, in. . . . .	0.083	0.060
Density, lb/in <sup>3</sup> . . . . .	0.29	0.30
Specific heat, Btu/lb-°R . . . . .	0.12	0.11
Thermal conductivity at 640°R, Btu-in/ft <sup>2</sup> -hr-°R . . . . .	112.0	71.0



TABLE VI.- PRESSURE-DATA RESULTS

(a) Nose R-3

Run	$\alpha$ , deg	Values of $p/p_g$ at various locations on model						
		P32	P33	P34 (a)	P35	P36	P37	P38
1	0	1.000	0.806	0.384	0.107	0.0830	0.108	0.0830
2	0	1.000			.107	.0829	.108	.0823
3	0	1.000	.817		.106	.0820	.108	.0815
4	0	1.000	.816		.107	.0833	.106	.0811
5	0	1.000	.817		.107	.0829	.106	.0823
6	0	1.000	.791		.103	.0810	.105	.0810
7	0	1.000	.794		.105	.779	.0989	.0758
8	5	.984	.867		.131	.102	.080	.061
9	10	.970	.909		.171	.139	.061	.047
10	10	.970	.954		.162	.125	.059	.046

<sup>a</sup>p34 instrumentation failed after run 1.

TABLE VI.- Continued

(b) 12.5° cone frustum

Run	Values of $p/p_s$ at various locations on model														
	P1	P2	P3	P4	P5	P6	P7	P8	P9	P10	P11	P12	P13	P14	P15 (a)
Nose R-3															
1	0.0674	0.0596	0.0585	0.0563	0.0535	0.0513	0.0518	0.0546	0.0557	0.0613	0.0652	0.0657	0.0691	0.0696	0.0741
2	.0669	.0591	.0580	.0564	.0539	.0514	.0519	.0541	.0544	.0597	.0630	.0641	.0680	.0682	
3	.0680	.0601	.0590	.0573	.0551	.0522	.0534	.0562	.0562	.0612	.0652	.0666	.0702	.0708	
4	.0667	.0594	.0583	.0567	.0539	.0517	.0522	.0550	.0556	.0628	.0661	.0667	.0689	.0678	
5	.0669	.0594	.0580	.0564	.0536	.0514	.0525	.0541	.0547	.0602	.0635	.0652	.0674	.0680	
6	.0661	.0596	.0596	.0587	.0549	.0512	.0512	.0540	.0549	.0614	.0642	.0661	.0689	.0708	
7	.0632	.0589	.0611	.0653	.0611	.0505	.0505	.0568	.0547	.0653	.0632	.0674	.0674	.0737	
8	.0928	.0850	.0867	.0867	.0883	.0906	.0944	.0989	.1017	.1128	.1200	.1211	.1244	.1183	
9	.1434	.1418	.1527	.1560	.1620	.1691	.1719	.1730	.1691	.1719	.1795	.1762	.1773	.1697	
10	.1371	.1371	.1519	.1624	.1646	.1624	.1688	.1762	.1709	.1793	.1814	.1835	.1835	.1814	
Nose R-1															
11	0.0636	0.0625	0.0647	0.0658	0.0647	0.0636	0.0653	0.0681	0.0670	0.0714	0.0742	0.0714	0.0731	0.0703	
12	.0562	.0607	.0640	.0652	.0652	.0640	.0663	.0685	.0674	.0730	.0758	.0747	.0758	.0725	
13	.0834	.0862	.0884	.0878	.0862	.0851	.0862	.0923	.0901	.0923	.0967	.0950	.0972	.0928	
14	.1795	.1680	.1707	.1635	.1685	.1680	.1657	.1707	.1602	.1663	.1751	.1729	.1751	.1702	
Nose R-S															
15	0.0629	0.0635	0.0651	0.0663	0.0657	0.0635	0.0651	0.0696	0.0679	0.0713	0.0741	0.0718	0.0713	0.0677	
16	.0635	.0623	.0640	.0657	.0657	.0635	.0646	.0686	.0663	.0720	.0754	.0742	.0737	.0708	
17	.1889	.1771	.1771	.1687	.1738	.1743	.1732	.1788	.1682	.1743	.1822	.1822	.1850	.1822	

ap15 instrumentation failed after run 1.

TABLE VI.- Continued

(b) Concluded

Run	Values of $p/p_s$ at various locations on model														
	P16	P17	P18	P19	P20	P21	P22	P23	P24	P25	P26	P27	P28	P29	P30
Nose R-3															
1	0.0713	0.0724	0.0752	0.0529	0.0513	0.0735	0.0513	0.0696	0.0501	0.0641	0.0524	0.0524	0.0669	0.0479	0.0685
2	.0713	.0729	.0746	.0530	.0530	.0729	.0514	.0691	.0497	.0657	.0519	.0525	.0674	.0497	.0669
3	.0719	.0739	.0764	.0545	.0537	.0744	.0522	.0702	.0494	.0663	.0517	.0525	.0674	.0483	.0680
4	.0694	.0700	.0722	.0531	.0528	.0689	.0517	.0711	.0494	.0650	.0522	.0528	.0653	.0500	.0656
5	.0702	.0718	.0762	.0530	.0519	.0702	.0508	.0696	.0483	.0624	.0519	.0525	.0649	.0497	.0674
6	.0736	.0773	.0773	.0531	.0512	.0745	.0503	.0689	.0475	.0642	.0512	.0521	.0689	.0466	.0698
7	.0716	.0800	.0716	.0526	.0505	.0779	.0484	.0653	.0442	.0611	.0484	.0484	.0674	.0421	.0674
8	.1178	.1161	.1194	.0764	.0522	.0739	.0378	.0422	.0322	.0394	.0383	.0522	.0639	.0733	.0994
9	.1724	.1702	.1795	.1188	.0536	.0668	.0274	.0213	.0230	.0263	.0285	.0569	.0618	.1111	.1324
10	.1793	.1846	.1835	.1181	.0527	.0749	.0243	.0200	.0158	.0179	.0285	.0549	.0633	.1055	.1382
Nose R-1															
11	0.0709	0.0720	0.0742	0.0647	0.0614	0.0776	0.0619	0.0725	0.0603	0.0614	0.0631	0.0625	0.0647	0.0575	0.0692
12	.0719	.0725	.0736	.0652	.0618	.0697	.0624	.0697	.0607	.0596	.0635	.0652	.0646	.0601	.0697
13	.0956	.0939	.0972	.0801	.0608	.0718	.0475	.0558	.0431	.0536	.0492	.0635	.0635	.0713	.0840
14	.1751	.1707	.1735	.1272	.0573	.0644	.0215	.0259	.0204	.0270	.0220	.0617	.0584	.1189	.1316
Nose R-S															
15	0.0696	0.0690	0.0713	0.0663	0.0607	0.0718	0.0629	0.0668	0.0618	0.0579	0.0640	0.0668	0.0612	0.0612	0.0685
16	.0725	.0725	.0742	.0657	.0635	.0754	.0657	.0708	.0635	.0601	.0663	.0669	.0657	.0612	.0720
17	.1861	.1839	.1883	.1328	.0577	.0645	.0224	.0235	.0179	.0224	.0241	.0645	.0617	.1300	.1413

TABLE VI.- Concluded

(c) Cone interior and surroundings ( $p/p_s$  results)

Run	$\alpha$ , deg	Values of $p/p_s$ at various locations on model					
		Free-stream static-pressure ratio	Cone interior	Boattail interior	Base	Cone P18 windward	Cone P25 leeward
Nose R-3							
1	0	0.016	0.067	0.066	0.067	0.075	0.064
2	0	.016	.066	.065	.066	.075	.066
3	0	.017	.069	.067	.068	.076	.066
4	0	.017	.064	.063	.067	.072	.065
5	0	.016	.064	.063	.066	.076	.062
6	0	.015	.062	.061	.063	.077	.064
7	0	.015	.034	.032	.011	.072	.061
8	5	.017	.067	.065	.065	.119	.039
9	10	.017	.061	.060	.061	.180	.026
10	10	.016	.027	.023	.009	.183	.018
Nose R-1							
11	0	0.017	0.066	0.065	0.073	0.074	0.061
12	0	.017	.067	.066	.074	.074	.060
13	2.5	.016	.065	.063	.070	.097	.054
14	10	.017	.052	.052	.051	.0174	.027
Nose R-S							
15	0	0.017	0.067	0.066	0.075	0.071	0.058
16	0	.016	.068	.067	.071	.074	.060
17	10	.016	.053	.053	.055	.188	.022

TABLE VII.- HEAT-TRANSFER DATA

(a) Ogive frustum

Run	Values of $\dot{q}/\dot{q}_s$ at thermocouples -											
	T126	T127	T128	T129	T130	T131	T132	T133	T134	T135	T136	T137
Nose R-1												
11	0.1250	0.1207	0.1036	0.1001	0.0876	0.0774	0.0761	0.0692	0.1215	0.1097	0.0979	0.0923
12	.1410	.1304	.1167	.1080	.0917	.0846	.0835	.0769	.1330	.1199	.1076	.1015
13	.1538	.1429	.1336	.1205	.1116	.0991	.0969	.0892	.1206	.1088	.0962	.0940
14	.2445	.2311	.2147	.2052	.1842	.1833	.1930	.2100	.1254	.1116	.1033	.1065
Nose R-S												
15		0.1344	0.1266	0.1115	0.1029	0.0954	0.0937	0.0862	0.1436	0.1301	0.1123	0.1081
16		.1364	.1209	.1084	.0951	.0880	.0845	.0755	.1537	.1346	.1133	.1056
17	0.2552	.2368	.2088	.1915	.1773	.1753	.1795	.1857	.1482	.1255	.1101	.1065

TABLE VII.- Continued

(a) Concluded

Run	Values of $\dot{q}/\dot{q}_s$ at thermocouples -											
	T138	T139	T140	T141	T142	T143	T144	T145	T146	T147	T148	T149
Nose R-1												
11	0.0853	0.0743	0.0706	0.0687	0.1303	0.1097	0.0998	0.0938	0.0853	0.0778	0.0729	0.0675
12	.0927	.0821	.0764	.0735	.1395	.1164	.1061	.1006	.0920	.0786	.0760	.0700
13	.0854	.0775	.0689	.0696	.1048	.0829	.0716	.0650	.0582	.0505	.0486	.0437
14	.0903	.0822	.0811	.0819	.0596	.0420	.0310	.0261	.0186	.0127	.0116	.0091
Nose R-S												
15	0.1013	0.0885	0.0843	0.0768	0.1188	0.1265	0.1124	0.1064	0.0989	0.0868	0.0834	0.0777
16	.0957	.0849	.0792	.0717	.1232	.1338	.1156	.1056	.0958	.0825	.0783	.0724
17	.0926	.0816	.0782	.0778	.0459	.0523	.0517	.0485	.0493	.0524	.0528	.0496

TABLE VII.- Continued

(b) 12.5° cone frustum

Run	Values of $\dot{q}/\dot{q}_s$ at thermocouples -																			
	T1	T2	T3	T4	T5	T6	T7	T8	T9	T10	T11	T12	T13	T14	T15	T16	T17	T18	T19	T20
Nose R-3																				
1	0.0798	0.0723	0.0708	0.0665	0.0650	0.0636	0.0620	0.0620	0.0586	0.0584	0.0605	0.0654	0.0684	0.0660	0.0800	0.0903	0.1058	0.1501	0.1704	0.0628
2	.0852	.0780	.0732	.0699	.0674	.0663	.0641	.0655	.0647	.0614	.0624	.0661	.0661	.0711	.0915	.1020	.1136	.1434	.1737	.0657
3	.0873	.0800	.0768	.0731	.0700	.0700	.0675	.0662	.0656	.0590	.0614	.0653	.0719	.0711	.0915	.1020	.1136	.1561	.1927	.0698
4	.0831	.0745	.0707	.0684	.0657	.0648	.0639	.0623	.0597	.0500	.0545	.0750	.1158	.0981	.1730	.1865	.1976	.2233	.2418	.0672
5	.0872	.0783	.0746	.0713	.0705	.0679	.0700	.0686	.0683	.0618	.0631	.0667	.0746	.0716	.0681	.1055	.1148	.1501	.1841	.0661
6	.0860	.0809	.0759	.0725	.0692	.0675	.0675	.0675	.0624	.0608	.0625	.0642	.0611	.0636	.0663	.0689	.0715	.0867	.1040	.0700
7	.0874	.0824	.0756	.0726	.0713	.0698	.0671	.0671	.0630	.0605	.0600	.0617	.0619	.0635	.0620	.0631	.0628	.0628	.0671	.0709
8	.1253	.1212	.1186	.1186	.1176	.1204	.1235	.1251	.1322	.1451	.1761	.2475	.3306	.3077	.4061	.4300	.4360	.4300	.4470	.1090
9	.1757	.1805	.1881	.2029	.2472	.2984	.3558	.3783	.4630	.4900	.5400	.5880	.6260	.6180	.6380	.6420	.6420	.6000	.6070	.1733
10	.1660	.1623	.1681	.1706	.1676	.1688	.1724	.1708	.1686	.1749	.2033	.2484	.2986	.2862	.3373	.3492	.3679	.3672	.3799	.1538
Nose R-1																				
11	0.0536	0.0523	0.0516	0.0524	0.0538	0.0602	0.0656	0.0787	0.1023	0.1140	0.1315	0.1483	0.1655	0.1650	0.1728	0.1755	0.1760	0.1751	0.1808	0.0479
12	.0577	.0535	.0563	.0554	.0616	.0670	.0784	.0884	.1134	.1328	.1571	.1777	.1957	.1893	.2052	.2066	.2069	.1932	.1954	.0545
13	.0719	.0753	.0792	.0929	.1071	.1229	.1451	.1646	.1838	.1896	.2002	.2061	.2162	.2125	.2173	.2205	.2225	.2083	.2156	.0811
14	.4160	.3970	.3779	.3706	.3758	.3592	.3540	.3481	.3446	.3312	.3381	.3373	.3535	.3510	.3452	.3573	.3535	.3364	.3386	.3190
Nose R-S																				
15	0.0677	0.0746	0.1021	0.1219	0.1626	0.1878	0.1958	0.1968	0.1950	0.1888	0.1898	0.1811			0.1816	0.1815	0.1885	0.1937	0.1960	0.1020
16	.0545	.0597	.0704	.0970	.1193	.1518	.1723	.1826	.1875	.1826	.1857	.1767			.1779	.1807	.1862	.1845	.1913	.0786
17	.4130	.3873	.3694	.3633	.3722	.3579	.3519	.3429	.3369	.3254	.3339	.3316			.3537	.3542	.3533	.3372	.3403	.3528

TABLE VII.- Continued

(b) Continued

Run	Values of $\dot{q}/\dot{q}_s$ at thermocouples -																			
	T21	T22	T23	T24	T25	T26	T27	T28	T29	T30	T31	T32	T33	T34	T35	T36	T37	T38	T39	T40
Nose R-3																				
1	0.0598	0.0639	0.0947	0.1388	0.0637	0.0621	0.0628	0.0914	0.0637	0.0620	0.0824	0.1453	0.0666	0.0918	0.2195	0.0594	0.0601	0.0853	0.1006	0.1465
2	0.0632	0.0661	0.0842	0.1346	0.0635	0.0584	0.0639	0.0798	0.0682	0.0634	0.0646	0.1231	0.0661	0.0624	0.2346	0.0633	0.0611	0.0679	0.0697	0.1416
3	0.0640	0.0667	0.0994	0.1455	0.0694	0.0605	0.0668	0.0919	0.0706	0.0665	0.0695	0.1421	0.0693	0.0624	0.2457	0.0650	0.0644	0.0713	0.0835	0.1312
4	0.0592	0.0608	0.1078	0.1542	0.0633	0.0548	0.0628	0.1004	0.0653	0.0623	0.0674	0.1744	0.0643	0.0594	0.2166	0.0631	0.0711	0.0839	0.2201	0.2273
5	0.0613	0.0659	0.1014	0.1458	0.0668	0.0589	0.0662	0.0961	0.0696	0.0644	0.0691	0.1706	0.0677	0.0630	0.2205	0.0663	0.0738	0.0961	0.2249	0.2276
6	0.0625	0.0618	0.0704	0.0851	0.0683	0.0608	0.0624	0.0677	0.0708	0.0649	0.0625	0.0762	0.0683	0.0607	0.2036	0.0640	0.0606	0.0610	0.0518	0.0710
7	0.0633	0.0628	0.0645	0.0657	0.0700	0.0613	0.0632	0.0655	0.0737	0.0653	0.0624	0.0657	0.0710	0.0622	0.0831	0.0650	0.0609	0.0615	0.0531	0.0578
8	0.1255	0.2906	0.4170	0.4320	0.0953	0.1017	0.2273	0.3352	0.0878	0.0855	0.1453	0.3188	0.0715	0.0679	0.2403	0.0569	0.0531	0.0559	0.1778	0.2025
9	0.4280	0.5920	0.6120	0.5760	0.1318	0.2923	0.4660	0.4800	0.1036	0.1902	0.3307	0.3534	0.0700	0.0994	0.2411	0.0481	0.0466	0.1052	0.1465	0.1562
10	0.1810	0.2731	0.3538	0.3667	0.1193	0.1427	0.1842	0.2666	0.0985	0.1048	0.1425	0.2114	0.0701	0.0665	0.1396	0.0477	0.0412	0.0508	0.0598	0.0748
Nose R-1																				
11	0.1192	0.1685	0.1816	0.1982	0.0510	0.1168	0.1628	0.1696	0.0516	0.1186	0.1571	0.1709	0.0515	0.1189	0.1754	0.0470	0.1235	0.1633	0.1640	0.1674
12	0.1426	0.1940	0.2085	0.1992	0.0571	0.1324	0.1816	0.1828	0.0580	0.1371	0.1312	0.1776	0.0570	0.1351	0.1583	0.0518	0.1434	0.1784	0.1945	0.1828
13	0.1962	0.2200	0.2200	0.2123	0.0742	0.1734	0.1993	0.1914	0.0688	0.1664	0.1755	0.1721	0.0580	0.1431	0.1613	0.0430	0.1235	0.1495	0.1443	0.1473
14	0.3218	0.3416	0.3383	0.3252	0.2571	0.2681	0.2788	0.2735	0.1912	0.2053	0.2055	0.2022	0.1237	0.1432	0.1356	0.0660	0.1003	0.1003	0.0895	0.0888
Nose R-S																				
15	0.1951	0.1910	0.1896	0.2045	0.1036	0.1850	0.1834	0.1738	0.1237	0.1900	0.1727	0.1694	0.1198	0.1864	0.1665	0.1146	0.1902	0.1848	0.1649	0.1667
16	0.1888	0.1893	0.1877	0.1941	0.0759	0.1804	0.1805	0.1716	0.0829	0.1874	0.1691	0.1594	0.0808	0.1818	0.1580	0.0745	0.1862	0.1704	0.1587	0.1573
17	0.3284	0.3350	0.3425	0.3283	0.1705	0.2687	0.2729	0.2688	0.1281	0.2063	0.1997	0.1943	0.0891	0.1456	0.1271	0.0620	0.0988	0.0941	0.0821	0.0826



TABLE VII.- Continued

(b) Continued

Values of $\dot{q}/\dot{q}_g$ at thermocouples -																				
Run	T41	T42	T43	T44	T45	T46	T47	T48	T49	T50	T51 (a)	T52	T53	T54	T55	T56	T57	T58	T59	T60
Nose R-3																				
1	0.0607	0.0551	0.0625	0.0892	0.1230	0.0576	0.0530	0.0574	0.0861	0.1139		0.0732	0.0675	0.0637	0.0613	0.0569	0.0544	0.0550	0.0530	0.0538
2	0.0650	0.0563	0.0722	0.1253	0.1598	0.0633	0.0578	0.0833	0.1238	0.1399		0.0792	0.0730	0.0692	0.0677	0.0626	0.0587	0.0586	0.0558	0.0549
3	0.0663	0.0584	0.0695	0.1235	0.1637	0.0643	0.0623	0.1070	0.1528	0.1681		0.0788	0.0745	0.0707	0.0676	0.0636	0.0609	0.0608	0.0575	0.0556
4	0.0621	0.0613	0.0749	0.1085	0.1389	0.0596	0.0527	0.0569	0.0905	0.1502		0.0745	0.0694	0.0652	0.0623	0.0588	0.0571	0.0584	0.0556	0.0575
5	0.0639	0.0652	0.0806	0.1148	0.1519	0.0623	0.0557	0.0712	0.1355	0.1478		0.0768	0.0733	0.0690	0.0659	0.0612	0.0561	0.0579	0.0543	0.0575
6	0.0657	0.0573	0.0558	0.0627	0.0763	0.0665	0.0556	0.0541	0.0609	0.0651		0.0801	0.0758	0.0724	0.0682	0.0648	0.0614	0.0614	0.0581	0.0590
7	0.0652	0.0589	0.0562	0.0597	0.0624	0.0664	0.0561	0.0551	0.0565	0.0530		0.0822	0.0767	0.0726	0.0706	0.0657	0.0610	0.0602	0.0580	0.0594
8	0.0490	0.0377	0.0408	0.0524	0.0872	0.0406	0.0291	0.0353	0.0503	0.0762		0.0563	0.0515	0.0463	0.0419	0.0365	0.0331	0.0315	0.0270	0.0252
9	0.0324	0.0275	0.0444	0.0843	0.0940	0.0219	0.0174	0.0214	0.0497	0.0661		0.0329	0.0274	0.0240	0.0208	0.0173	0.0155	0.0140	0.0125	0.0107
10	0.0298	0.0253	0.0283	0.0349	0.0400	0.0214	0.0149	0.0125	0.0128	0.0122		0.0358	0.0280	0.0250	0.0217	0.0187	0.0155	0.0128	0.0119	0.0098
Nose R-1																				
11	0.0502	0.1221	0.1656	0.1741	0.1706	0.0486	0.1064	0.1554	0.1739	0.1524		0.0516	0.0520	0.0509	0.0517	0.0502	0.0538	0.0614	0.0716	0.0907
12	0.0509	0.1397	0.1818	0.1950	0.1876	0.0535	0.1243	0.1769	0.1949	0.1720		0.0560	0.0551	0.0552	0.0561	0.0579	0.0579	0.0694	0.0782	0.1066
13	0.0363	0.0962	0.1362	0.1428	0.1397	0.0256	0.0660	0.1131	0.1378	0.1183		0.0301	0.0301	0.0301	0.0301	0.0286	0.0279	0.0370	0.0500	0.0861
14	0.0354	0.0686	0.0753	0.0718	0.0652	0.0087	0.0499	0.0660	0.0705	0.0693		0.0111	0.0170	0.0198	0.0226	0.0260	0.0286	0.0319	0.0329	0.0369
Nose R-S																				
15	0.1335	0.1890	0.1795	0.1767	0.1707	0.1189	0.1765	0.1775	0.1808	0.1563		0.0846	0.0974	0.1043	0.1316	0.1625	0.1783	0.1860	0.1808	0.1800
16	0.0892	0.1854	0.1753	0.1672	0.1611	0.0763	0.1721	0.1679	0.1698	0.1469		0.0584	0.0627	0.0706	0.0833	0.1160	0.1503	0.1685	0.1721	0.1773
17	0.0420	0.0695	0.0651	0.0631	0.0682	0.0352	0.0634	0.0578	0.0553	0.0609		0.0481	0.0563	0.0596	0.0611	0.0603	0.0614	0.0643	0.0636	0.0600

aT51 instrumentation failed.

TABLE VII.- Continued

(b) Continued

Run	Values of $\dot{q}/\dot{q}_s$ at thermocouples -														
	T61	T62	T63	T64	T65	T66	T67 (a)	T68	T69	T70	T71	T72	T73	T74	T75
Nose R-3															
1	0.0532	0.0513	0.0365	0.0532	0.0579	0.0795		0.0987	0.1271	0.1419	0.0593	0.0611	0.1135	0.1680	0.1976
2	0.0551	0.0545	0.0448	0.0573	0.0586	0.0647		0.0834	0.1142	0.1343	0.0629	0.0585	0.0619	0.0761	0.1300
3	0.0542	0.0556	0.0507	0.0530	0.0590	0.0702		0.0913	0.1221	0.1472	0.0630	0.0595	0.0583	0.0732	0.1136
4	0.0540	0.0523	0.0463	0.0547	0.0549	0.0800		0.0913	0.1552	0.1679	0.0602	0.0572	0.0573	0.0901	0.1553
5	0.0548	0.0529	0.0464	0.0564	0.0569	0.0811		0.1009	0.1305	0.1603	0.0633	0.0598	0.0564	0.0886	0.1478
6	0.0573	0.0523	0.0479	0.0490	0.0532	0.0541		0.0592	0.0695	0.0814	0.0655	0.0607	0.0574	0.0567	0.0695
7	0.0570	0.0553	0.0350	0.0548	0.0562	0.0549		0.0552	0.0590	0.0601	0.0655	0.0605	0.0578	0.0549	0.0582
8	0.0229	0.0203	0.0173	0.0190	0.0181	0.0353		0.0502	0.0816	0.1007	0.0412	0.0261	0.0271	0.0544	0.0939
9	0.0110	0.0099	0.0178	0.0321	0.0364	0.0495		0.0563	0.0678	0.0854	0.0232	0.0355	0.0398	0.0746	0.1061
10	0.0080	0.0074	0.0080	0.0119	0.0131	0.0208		0.0250	0.0298	0.0324	0.0241	0.0164	0.0164	0.0140	0.0182
Nose R-1															
11	0.0152	0.1264	0.0899	0.1487	0.1541	0.1682	0.1686	0.1713	0.1622	0.1682	0.0609	0.1732	0.1688	0.1733	0.1641
12	0.1270	0.1456	0.1652	0.1679	0.1724	0.1831		0.1903	0.1785	0.1829	0.0474	0.1350	0.1769	0.1816	0.1873
13	0.1012	0.1084	0.1237	0.1173	0.1148	0.1323		0.1214	0.1219	0.1357	0.1140	0.1223	0.1282	0.1343	0.1534
14	0.0400	0.0400	0.0353	0.0404	0.0387	0.0433		0.0441	0.0590	0.0688	0.0111	0.0561	0.0670	0.0672	0.0691
Nose R-S															
15	0.1722	0.1739	0.1705	0.1669	0.1609	0.1678	0.1704	0.1754	0.1616	0.1751	0.1231	0.1817	0.1687	0.1663	0.2127
16	0.1741	0.1684	0.1634	0.1589	0.1567	0.1592	0.1617	0.1634	0.1493	0.1607	0.0759	0.1788	0.1670	0.1604	0.1664
17	0.0625	0.0625	0.0604	0.0585	0.0618	0.0601	0.0605	0.0795	0.0936	0.0865	0.0332	0.0658	0.0566	0.0501	0.0874

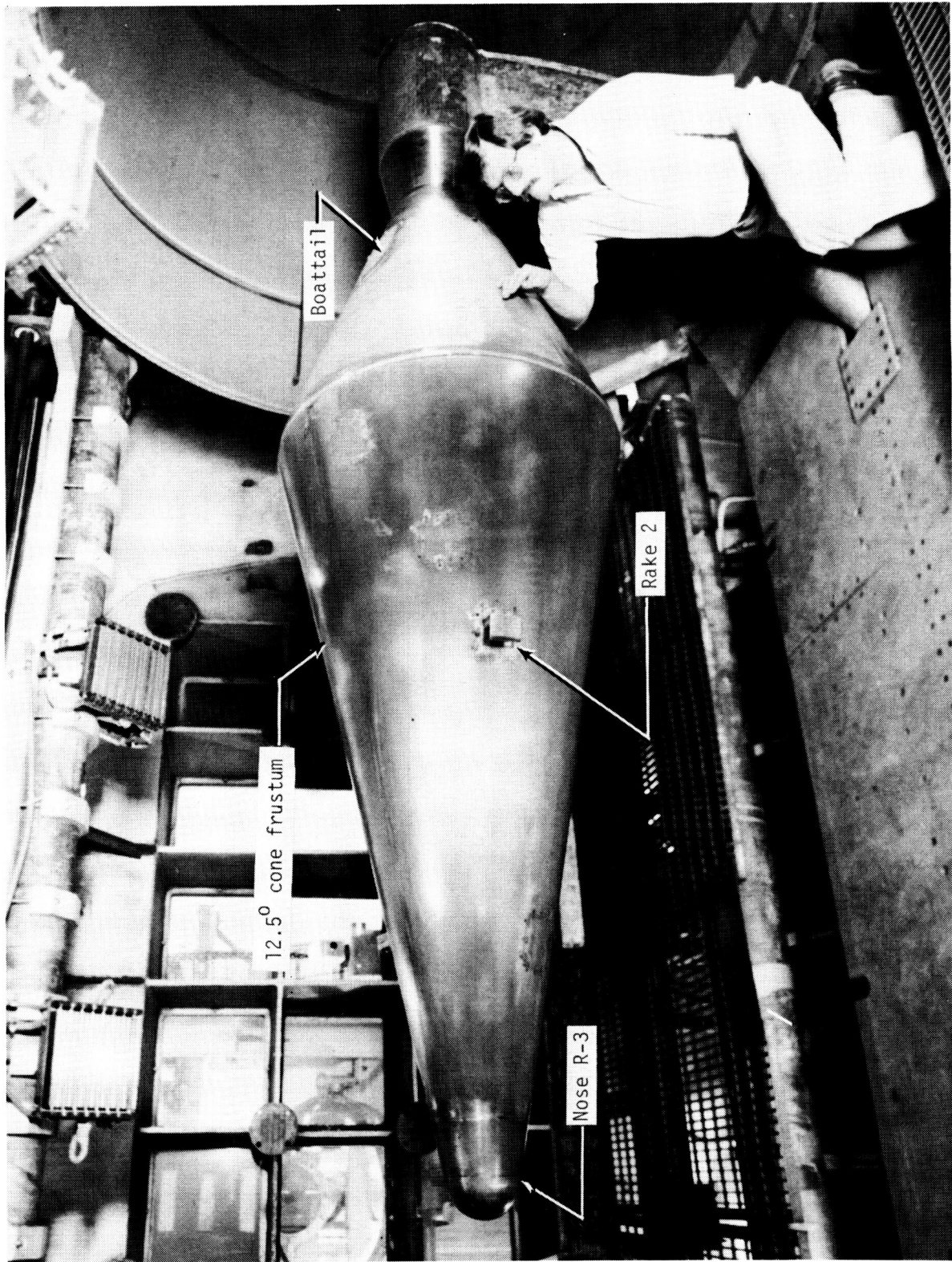
<sup>a</sup>T67 instrumentation was not always functional.

TABLE VII.- Concluded

(b) Concluded

Values of $\dot{q}/\dot{q}_s$ at thermocouples -																					
Run	T81	T82	T83	T84	T85	T86	T87	T88	T89 (a)	T90	T91	T92	T93	T94	T95	T96	T97	T98	T99	T100	T101
Nose R-3																					
1	0.1362	0.1855	0.2151	0.0611	0.0529	0.1555	0.0630	0.0680		0.2126	0.2234	0.0686	0.1838	0.2043	0.2140	0.2210	0.0666	0.0751	0.1436	0.2091	0.2173
2	0.0579	0.0562	0.1174	0.0658	0.0582	0.1142	0.0688	0.0660		0.2088	0.2226	0.0679	0.1883	0.2072	0.2211	0.2291	0.0669	0.0754	0.1474	0.2140	0.2251
3	0.0570	0.0544	0.1231	0.0674	0.0570	0.1352	0.0705	0.0993		0.2302	0.2374	0.0709	0.2050	0.2192	0.2285	0.2372	0.0702	0.0831	0.1838	0.2280	0.2401
4	0.0572	0.0502	0.1571	0.0619	0.0515	0.1912	0.0683	0.2161		0.2249	0.2304	0.0662	0.1934	0.1759	0.1807	0.1902	0.0645	0.2138	0.2175	0.2255	0.2316
5	0.0567	0.0551	0.1259	0.0651	0.0538	0.1679	0.0685	0.2105		0.2232	0.2261	0.0695	0.1952	0.2055	0.2234	0.2330	0.0685	0.0761	0.1986	0.2250	0.2301
6	0.0590	0.0540	0.0598	0.0691	0.0565	0.0754	0.0725	0.0641		0.1865	0.1914	0.0708	0.0849	0.1673	0.1897	0.2031	0.0708	0.0682	0.1116	0.1812	0.1715
7	0.0584	0.0548	0.0610	0.0663	0.0589	0.0596	0.0726	0.0637		0.0605	0.0627	0.0708	0.0664	0.0616	0.0602	0.0614	0.0714	0.0648	0.0613	0.0592	0.0595
8	0.0656	0.0883	0.2241	0.0692	0.1051	0.2512	0.0967	0.2691		0.3215	0.3390	0.1021	0.3034	0.3140	0.3600	0.3832	0.1102	0.1241	0.2643	0.3900	0.4120
9	0.0552	0.1453	0.1817	0.0946	0.2356	0.2333	0.1113	0.3400		0.3886	0.3881	0.1389	0.4120	0.4790	0.4860	0.4790	0.2806	0.4430	0.5520	0.5710	0.5540
10	0.0417	0.0831	0.1168	0.0665	0.0987	0.1636	0.0985	0.2104		0.2438	0.2352	0.1275	0.1481	0.2054	0.2665	0.2978	0.1556	0.1747	0.2544	0.3221	0.3367
Nose R-1																					
11	0.1187	0.1581	0.1711	0.0441	0.1166	0.1515	0.0531	0.1320		0.1784	0.1767	0.0474	0.1831	0.1770	0.1726	0.1796	0.0493	0.1171	0.1746	0.1780	0.1700
12	0.1343	0.1726	0.1837	0.0518	0.1290	0.1637	0.0615	0.2183		0.1945	0.1894	0.0543	0.0868	0.1620	0.1674	0.1723	0.0526	0.2121	0.2071	0.1994	0.1905
13	0.1150	0.1388	0.1553	0.0520	0.1334	0.1442	0.0694	0.2004		0.1799	0.1713	0.0702	0.2174	0.2037	0.1948	0.1904	0.0770	0.1825	0.2003	0.2066	0.2020
14	0.1082	0.0978	0.1045	0.1252	0.1585	0.1318	0.2207	0.2119		0.2143	0.2105	0.2837	0.2692	0.2784	0.2702	0.2735	0.3508	0.3134	0.3257	0.3125	0.3070
Nose R-5																					
15	0.1863	0.1672	0.1751	0.1121	0.1845	0.1472	0.1172	0.1882		0.1711	0.1918	0.1078	0.1848	0.1773	0.1696	0.1880	0.1113	0.0912	0.1791	0.1752	0.1699
16	0.1850	0.1635	0.1643	0.0769	0.1819	0.1448	0.0828	0.1864		0.1723	0.1840	0.0734	0.1796	0.1788	0.1748	0.1810	0.0780	0.1570	0.1754	0.1707	0.1700
17	0.1020	0.0882	0.1125	0.0855	0.1532	0.1263	0.1736	0.2032		0.2106	0.2089	0.2807	0.2647	0.2731	0.2723	0.2765	0.3440	0.1570	0.3141	0.3211	0.3122

aT89 instrumentation failed.



L-82-7048

Figure 1.- Model in Langley 8-Foot High-Temperature Tunnel.



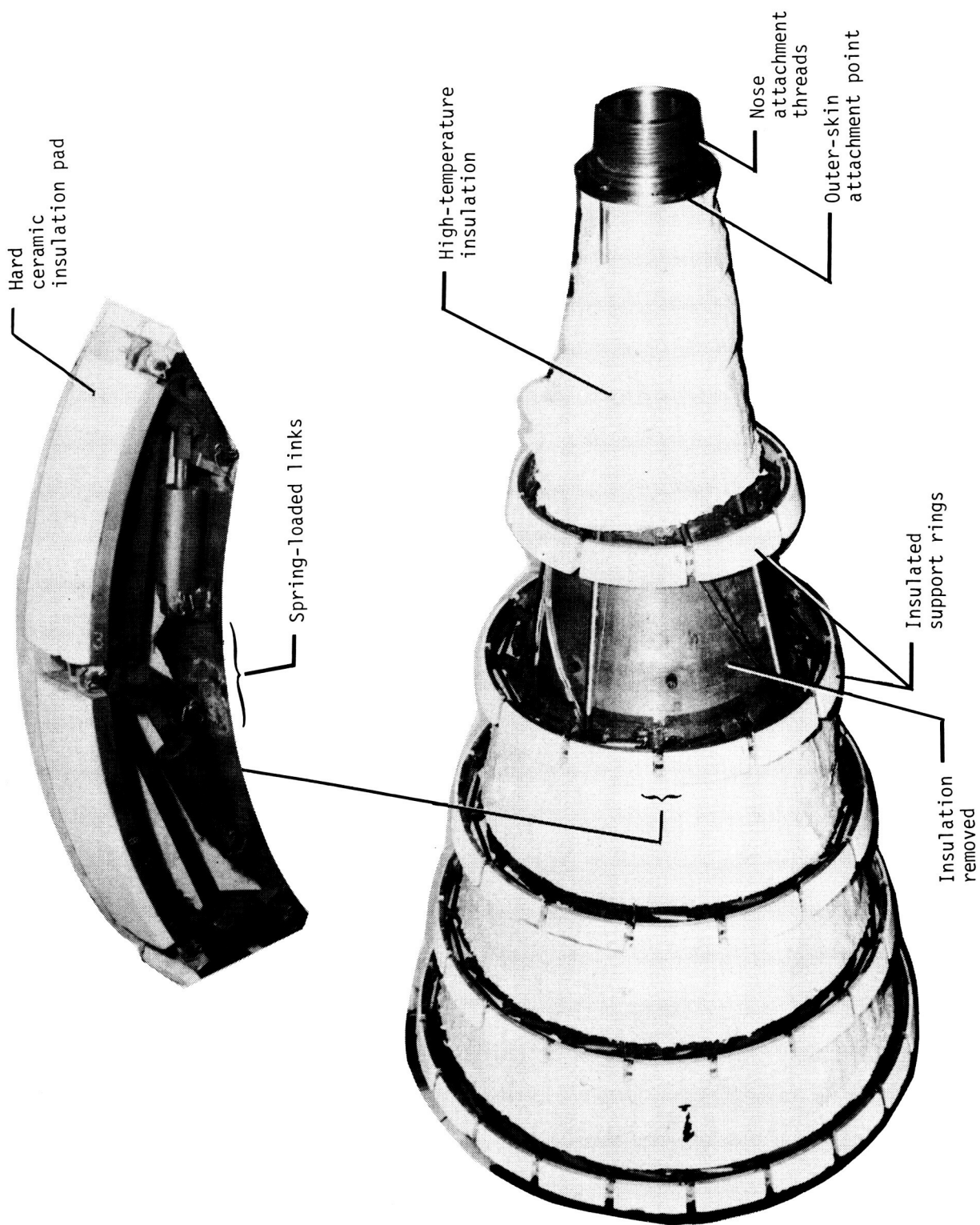
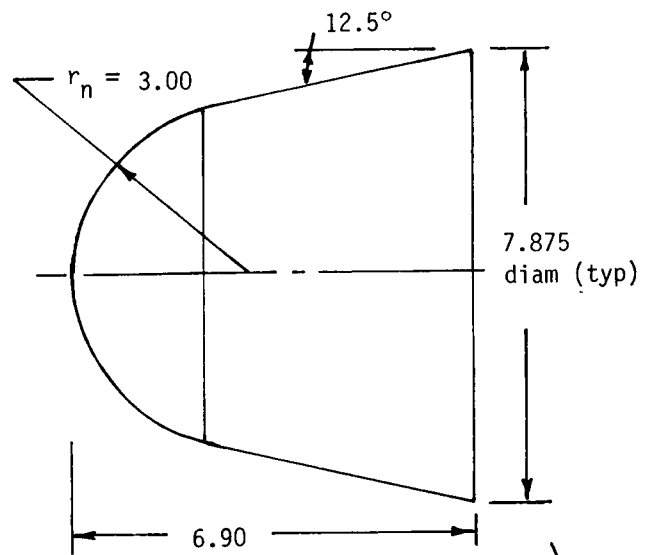


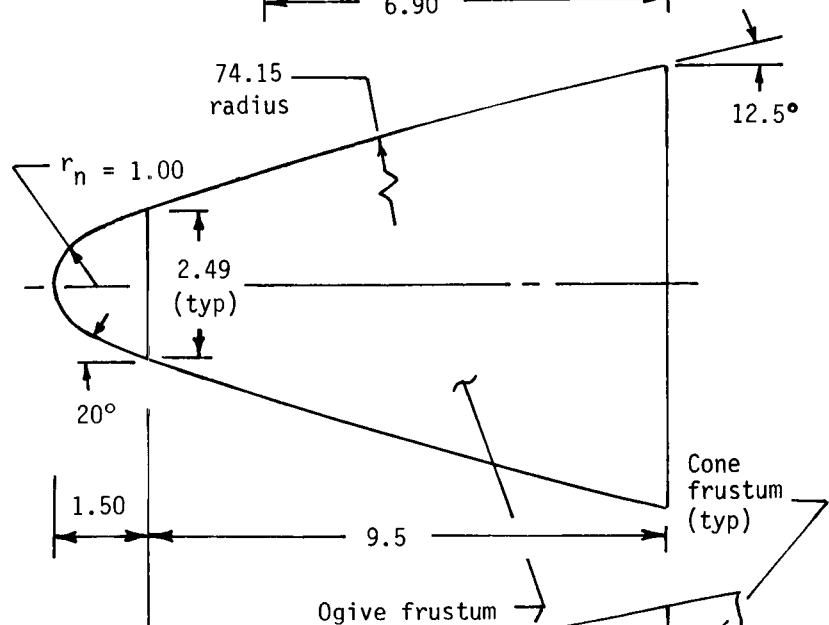
Figure 3.- Inner shell of 12.5° cone frustum. Model with outer skin removed.

L-84-12,922

(a) Nose R-3. 3-in-radius tip on 12.5° cone frustum.



(b) Nose R-1. 1-in-radius tip on ogive frustum.



(c) Nose R-S. Sharp tip on ogive frustum.

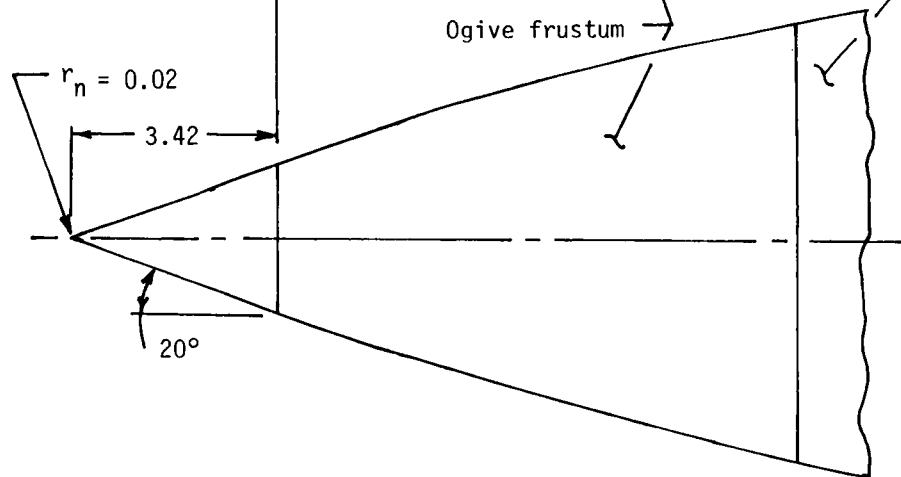


Figure 4.- Nose shapes for attachment to 12.5° cone frustum. Dimensions are given in inches unless otherwise specified.

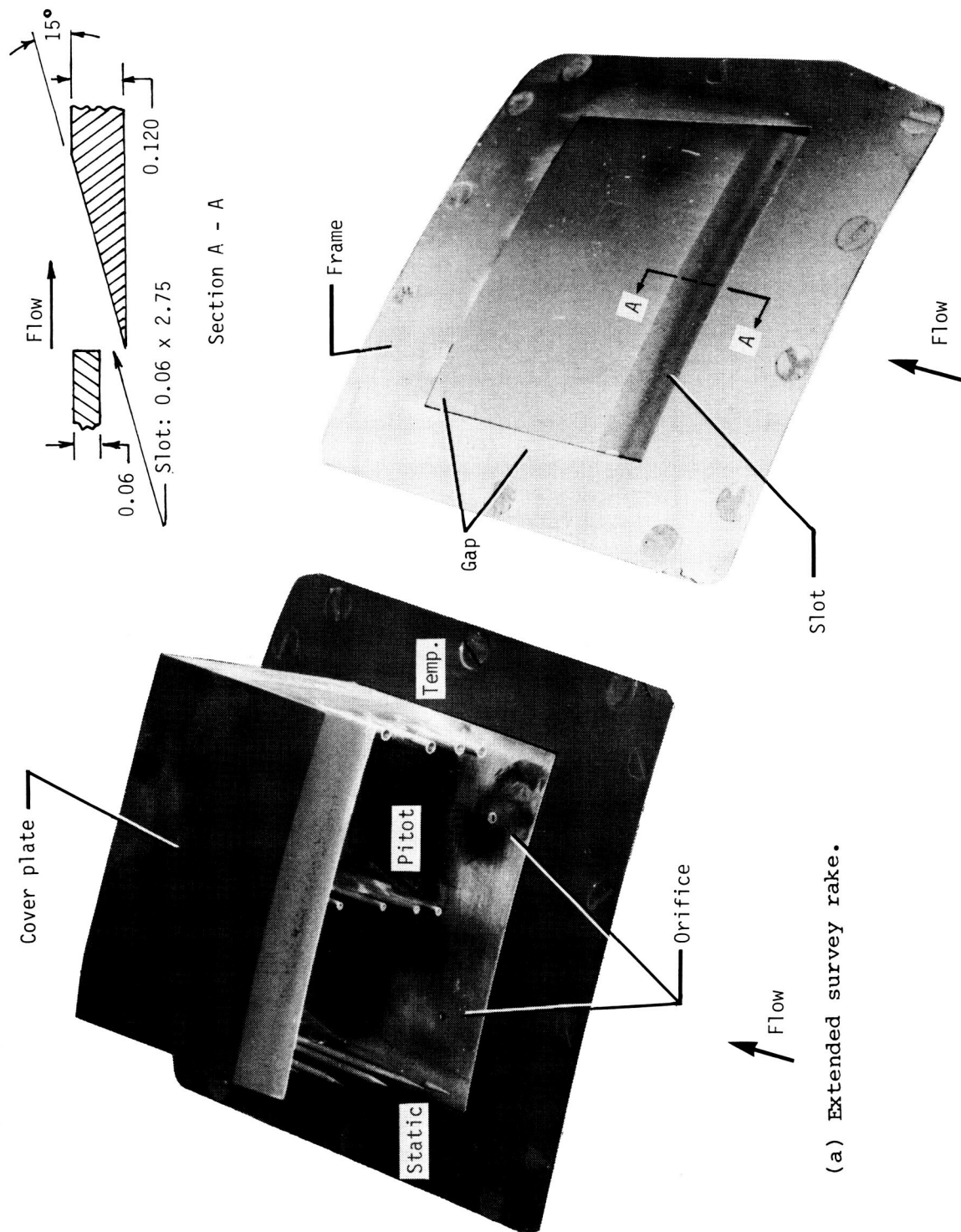


Figure 5.- Photographs of shock flow-field survey rake. Dimensions are given in inches unless otherwise specified. L-84-12,923



Rake location		
No.	$s_c$ , in.	$\varphi$ , deg
1	14.8	-45
2	38.3	90
3	58.6	-135

Note:  $s_c$  measured to orifice reference line

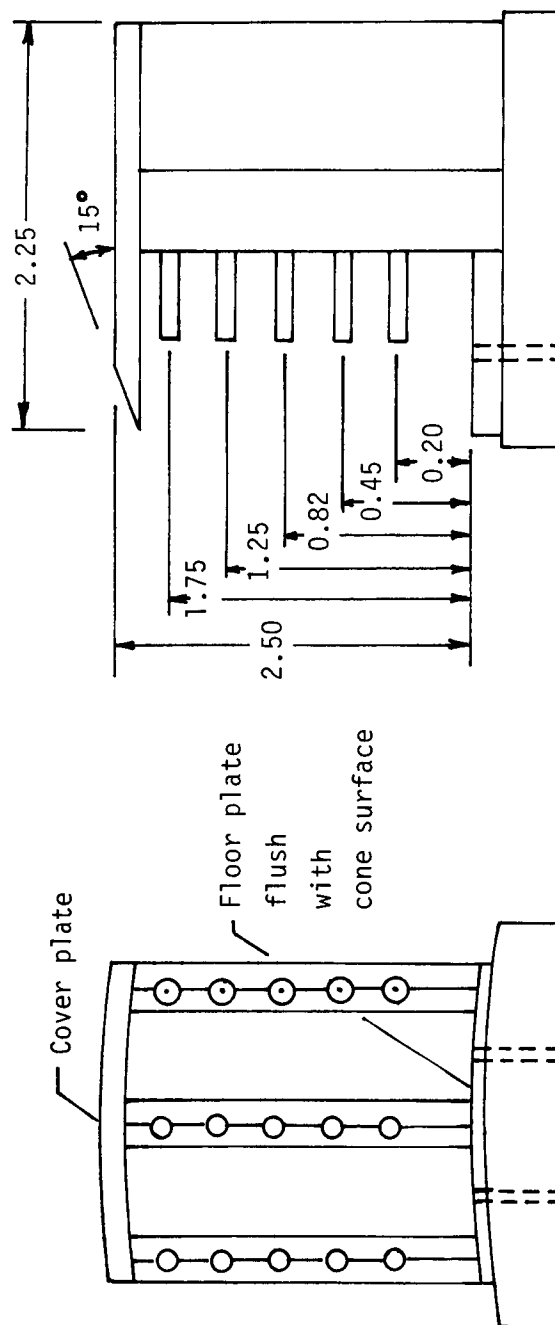
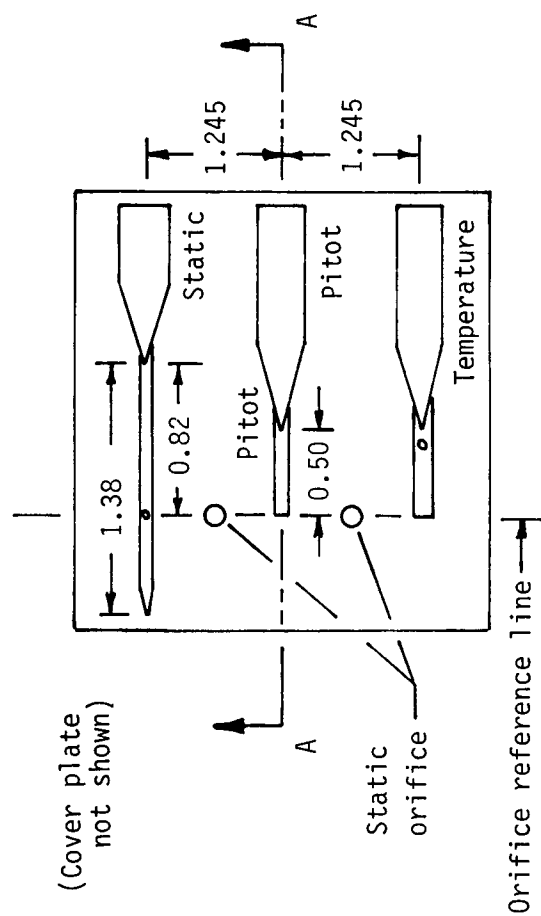


Figure 6.- Assembly of flow-field survey rake. Dimensions are given in inches unless otherwise specified.

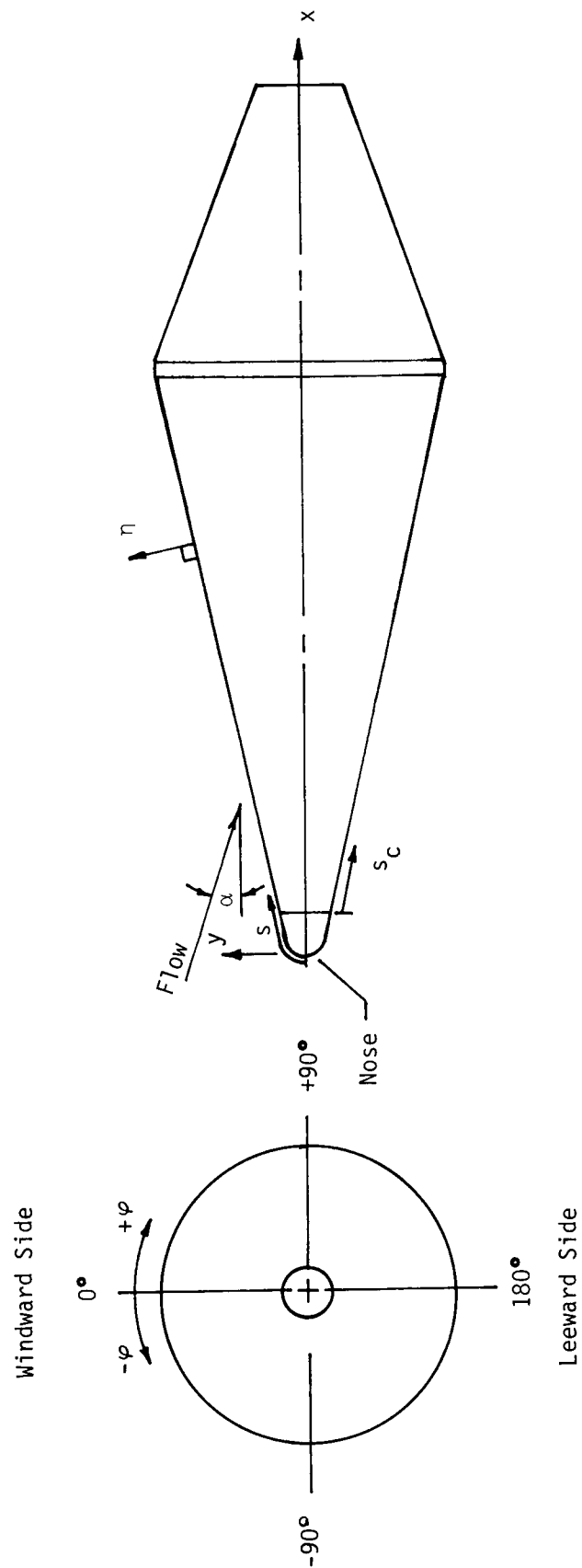


Figure 7.- Model coordinate system.

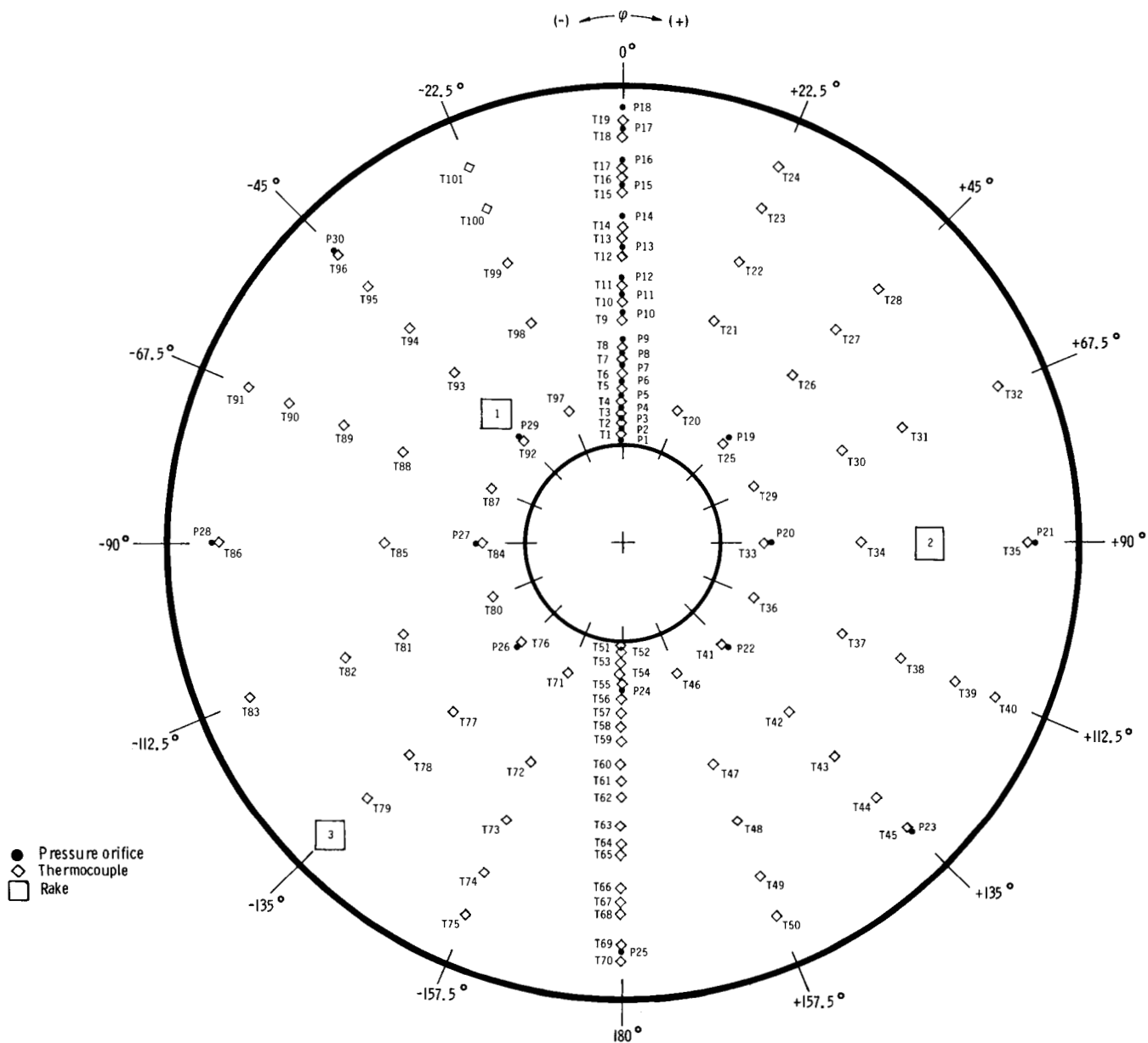


Figure 8.- Thermocouple and pressure-orifice locations on cone frustum.  
Front view.

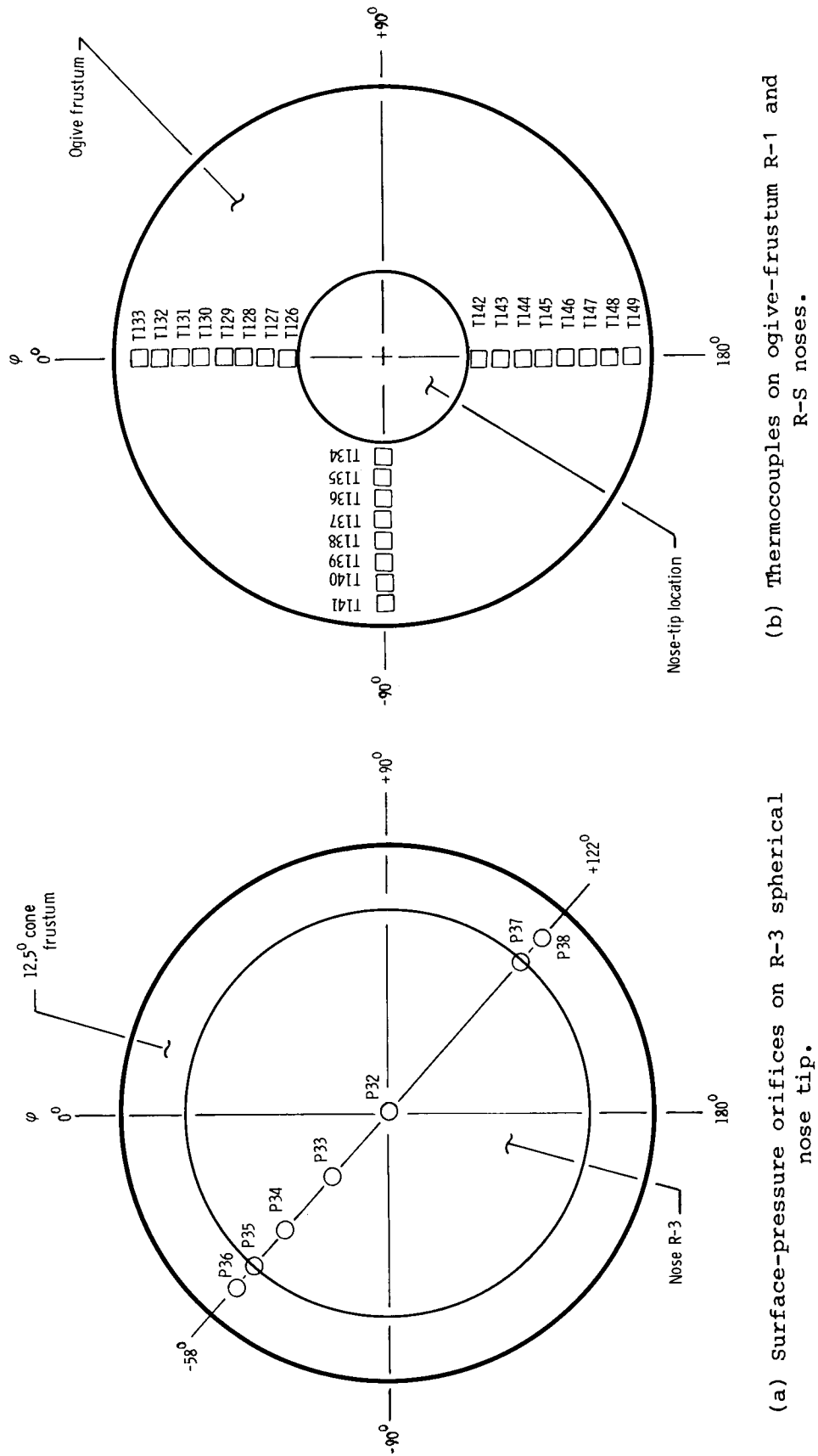


Figure 9.- Nose instrumentation. Front view.

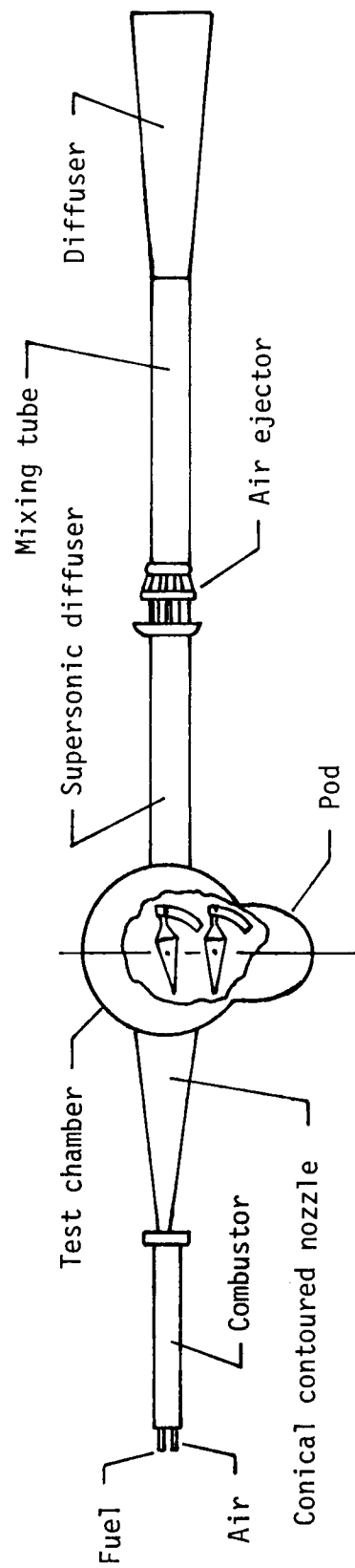


Figure 10.- Schematic drawing of the Langley 8-Foot High-Temperature Tunnel.

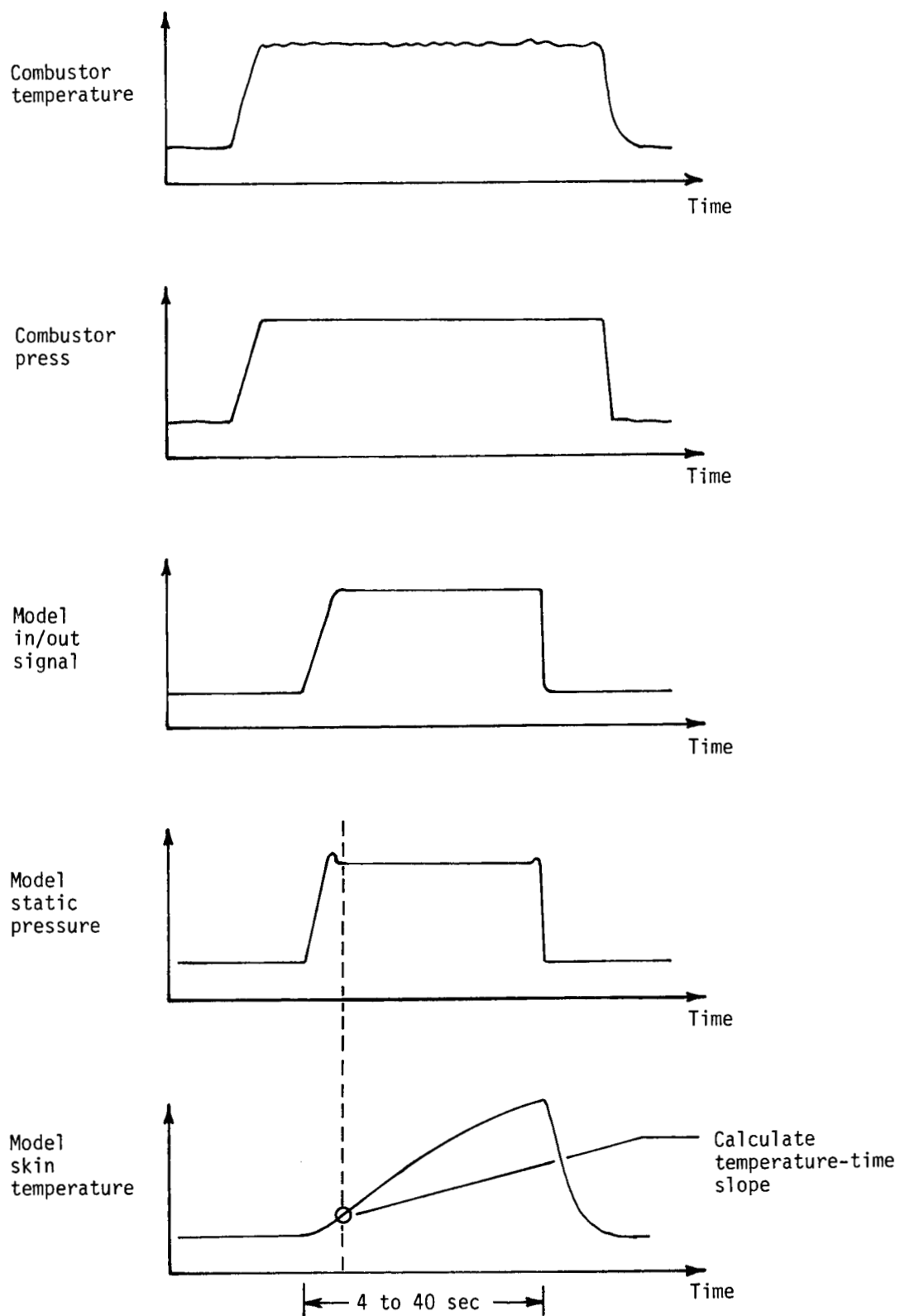


Figure 11.- Nominal test time histories.

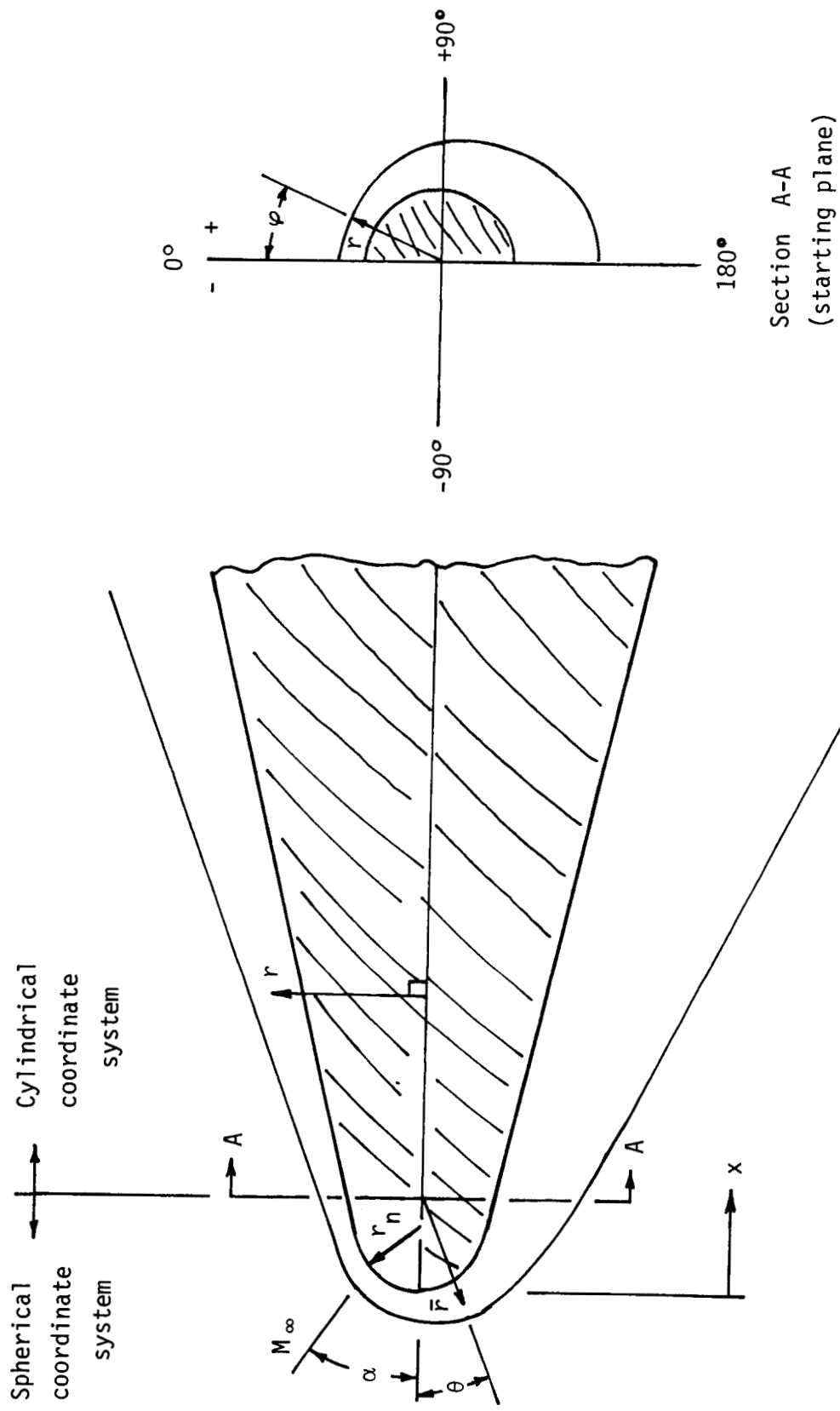
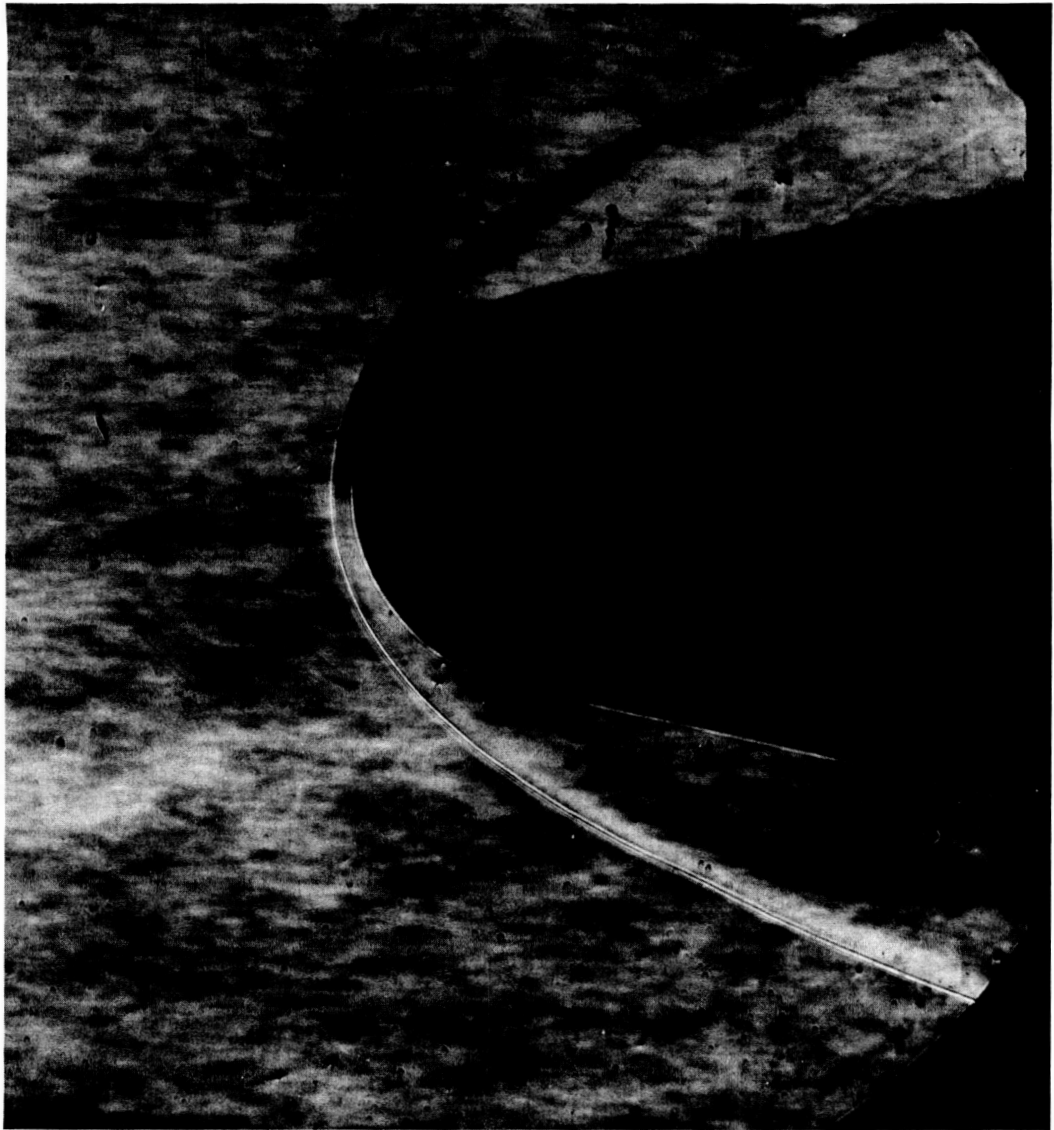


Figure 12.- Coordinate system for computational grid.

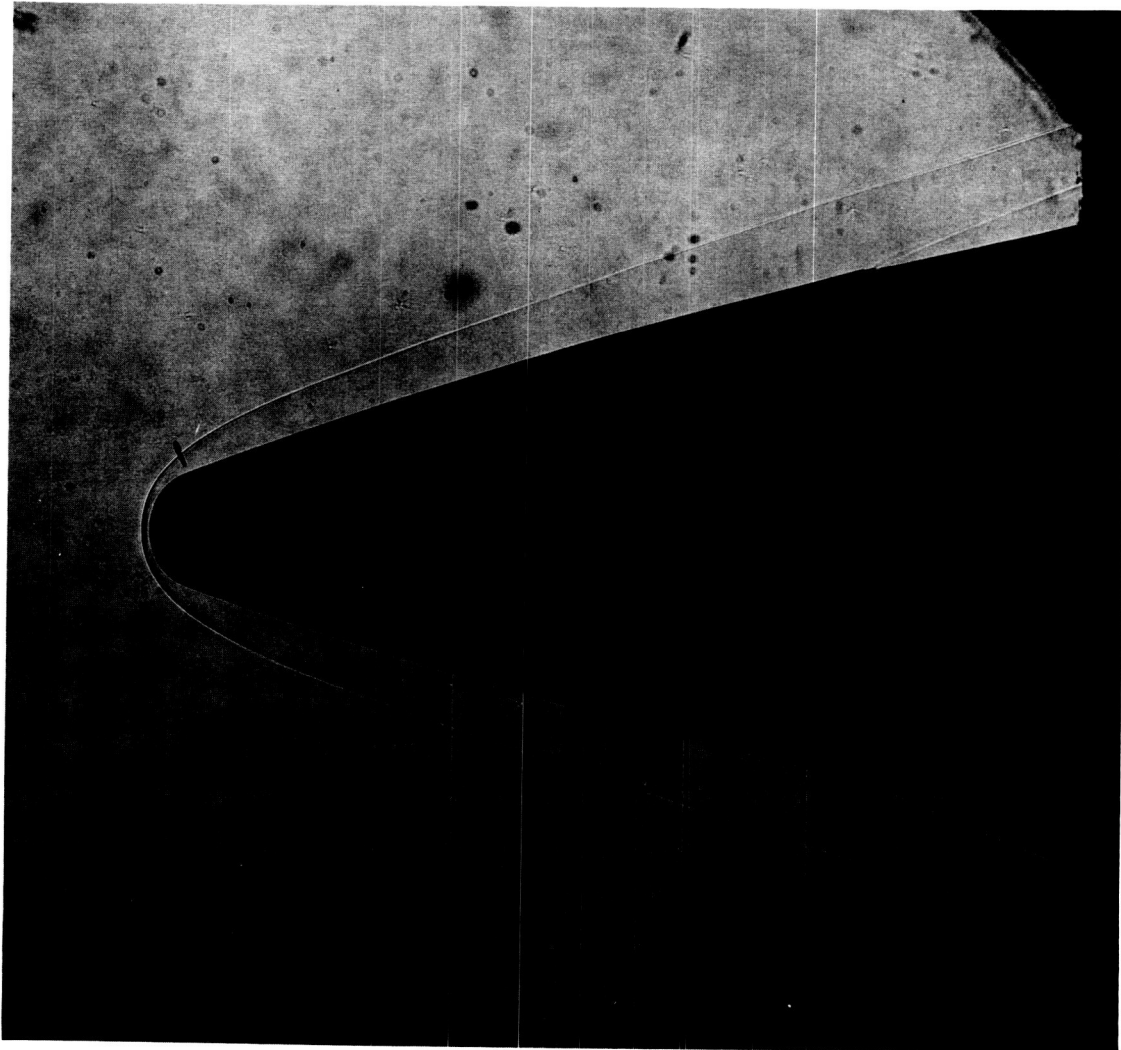


L-84-100

(a) Schlieren photograph of nose R-3. Run 3.

Figure 13.- Representative photographs of shock shape over nose.  
 $\alpha = 0^\circ$ ; nominal  $N_{Re} = 1.4 \times 10^6$  per foot.

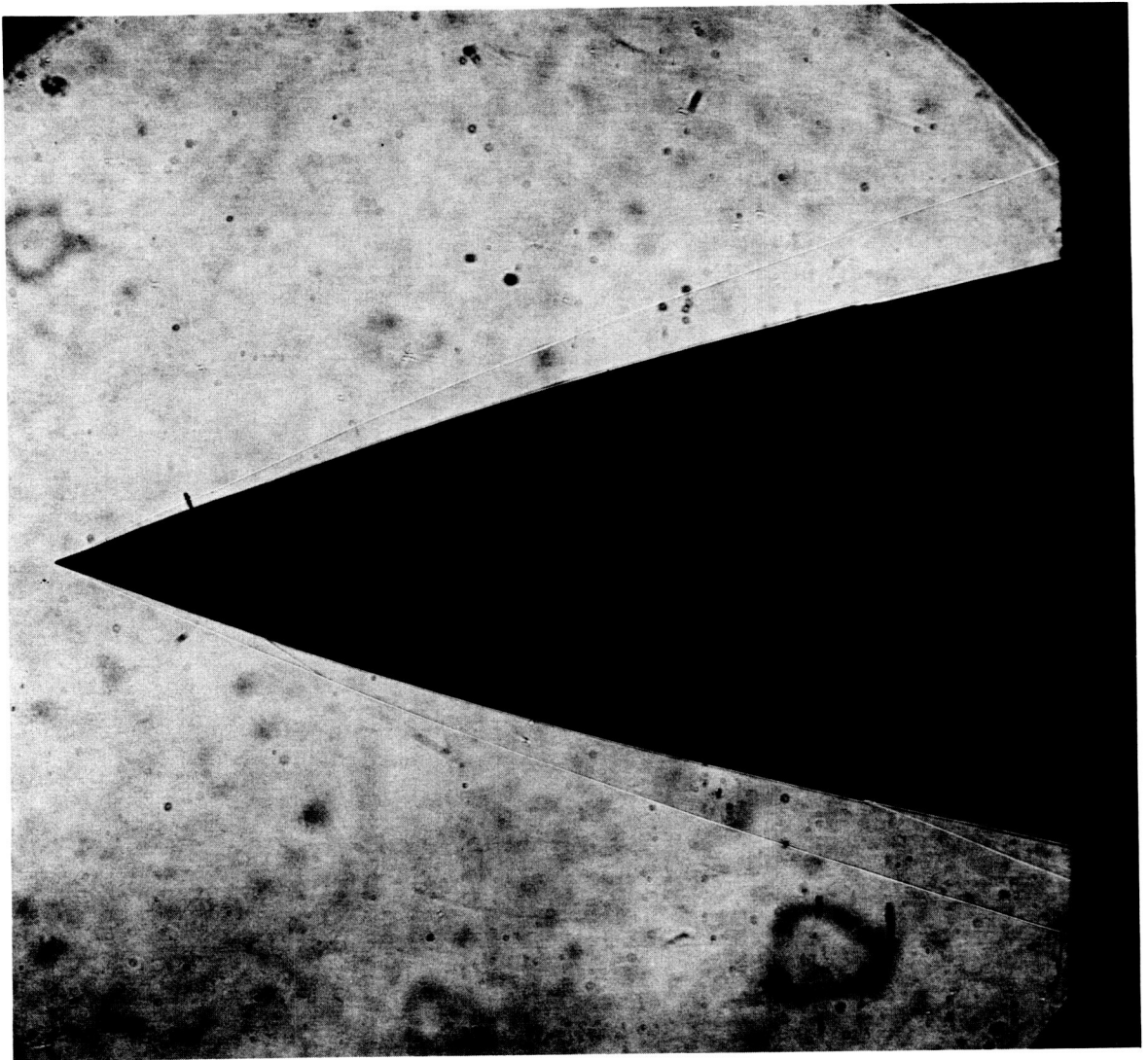




(b) Shadowgraph of nose R-1. Run 12.

L-84-101

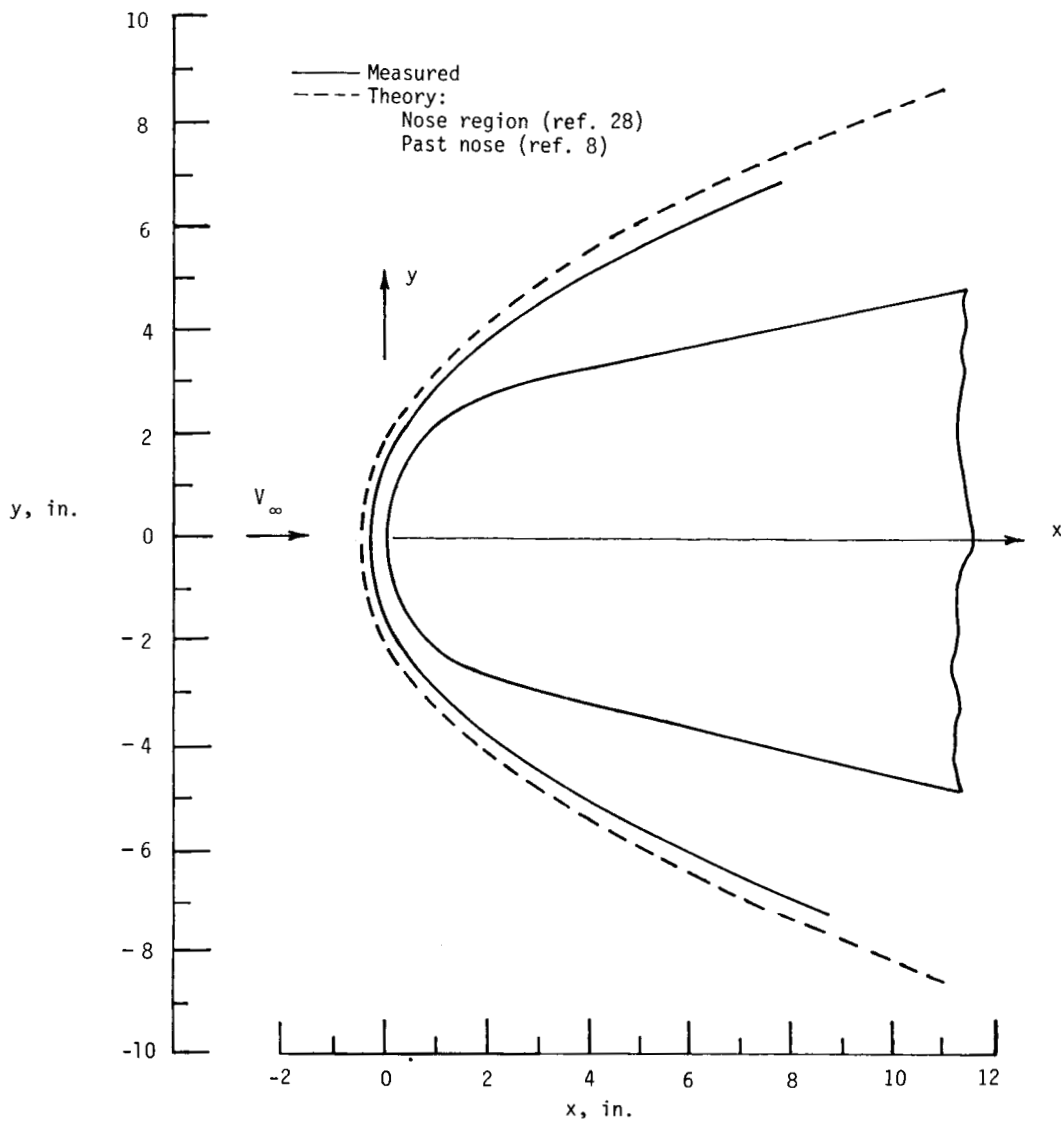
Figure 13.- Continued.



(c) Shadowgraph of nose R-S. Run 16.

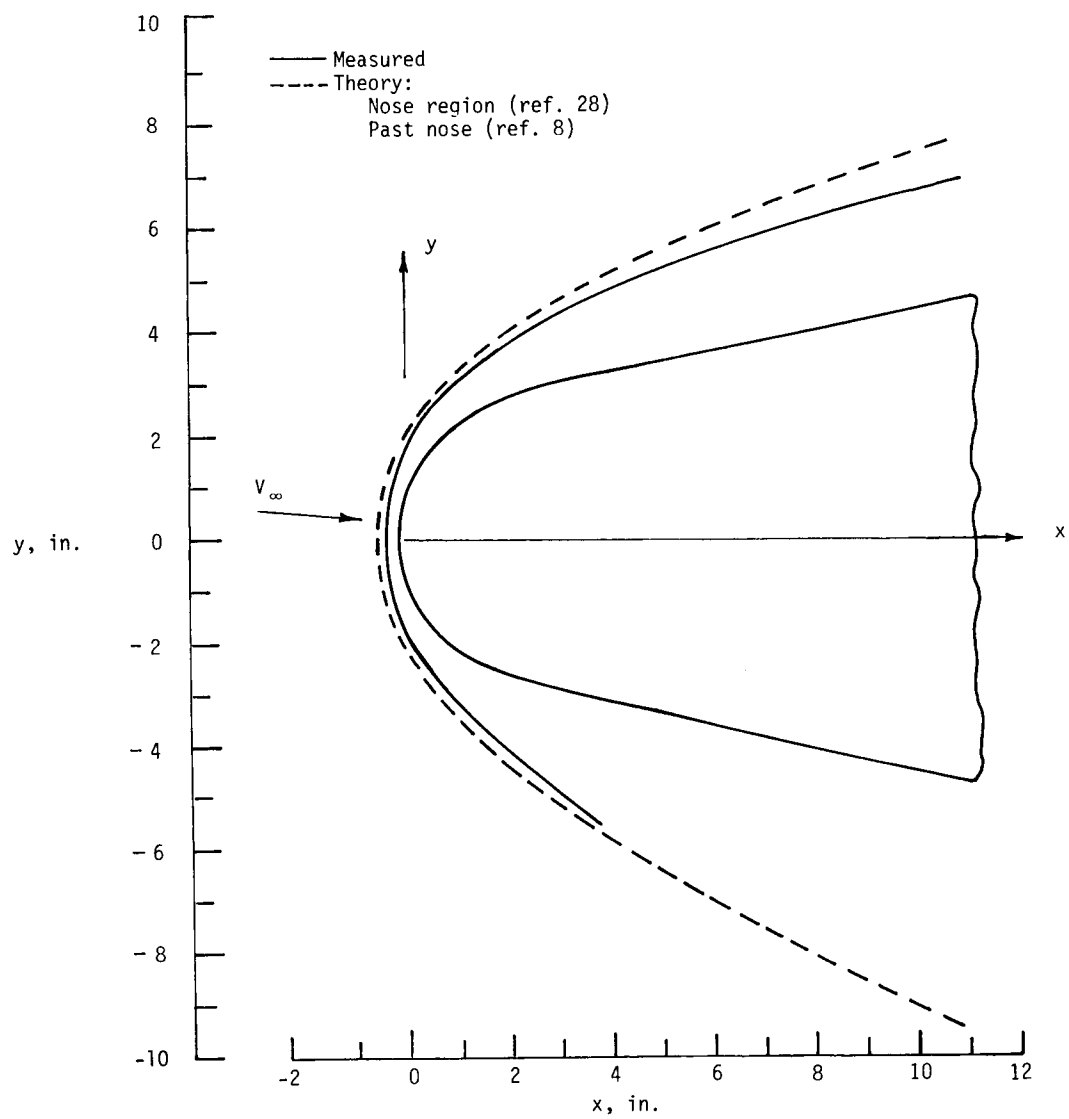
L-84-102

Figure 13.- Concluded.



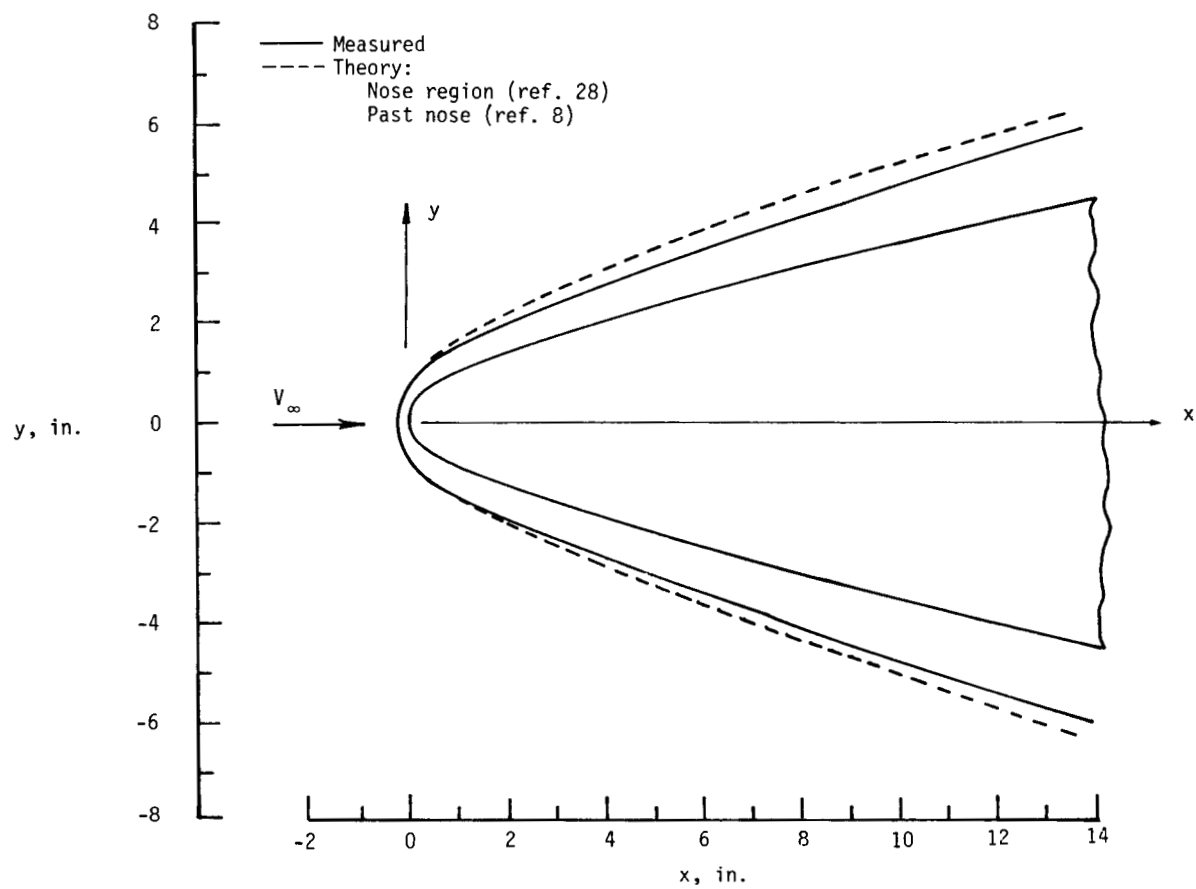
(a) Nose R-3.  $\alpha = 0^\circ$ .

Figure 14.- Measured and predicted shock shapes.



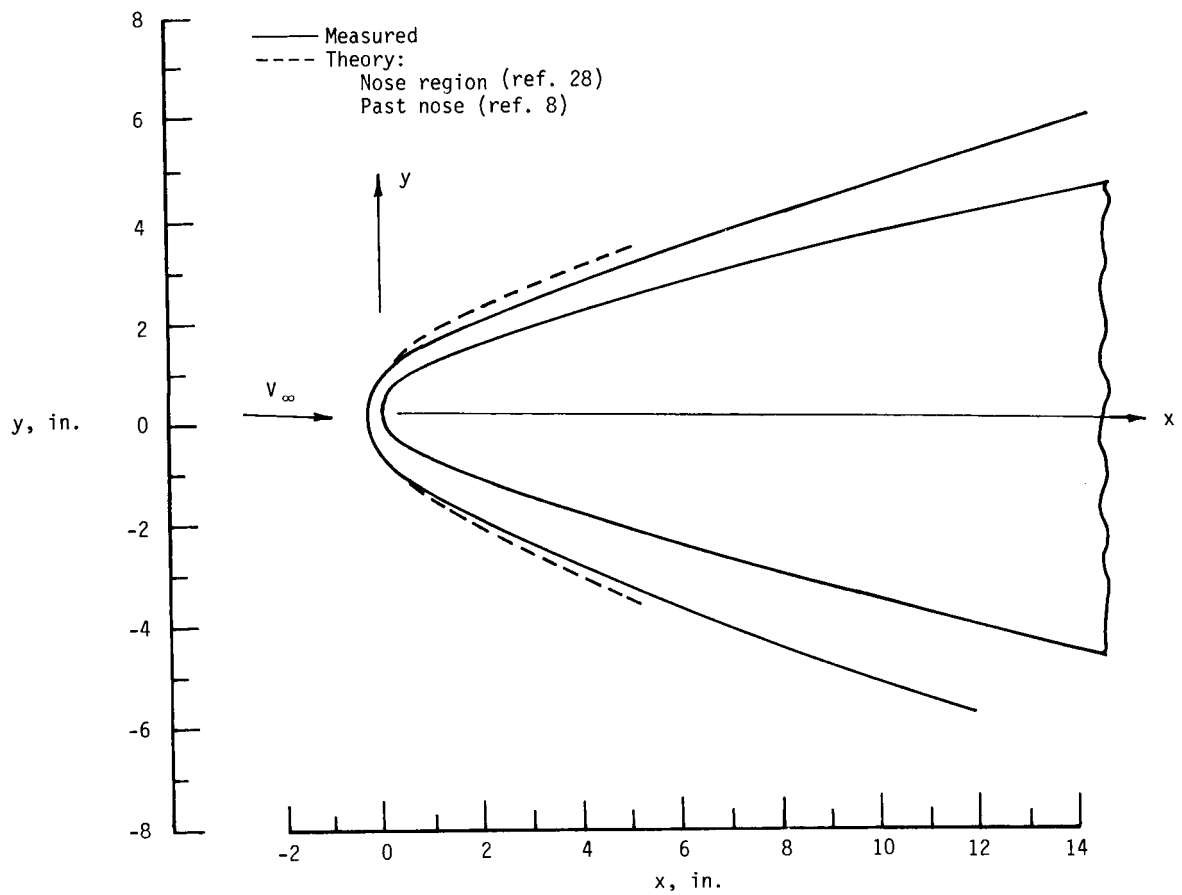
(b) Nose R-3.  $\alpha = 5^\circ$ .

Figure 14.- Continued.



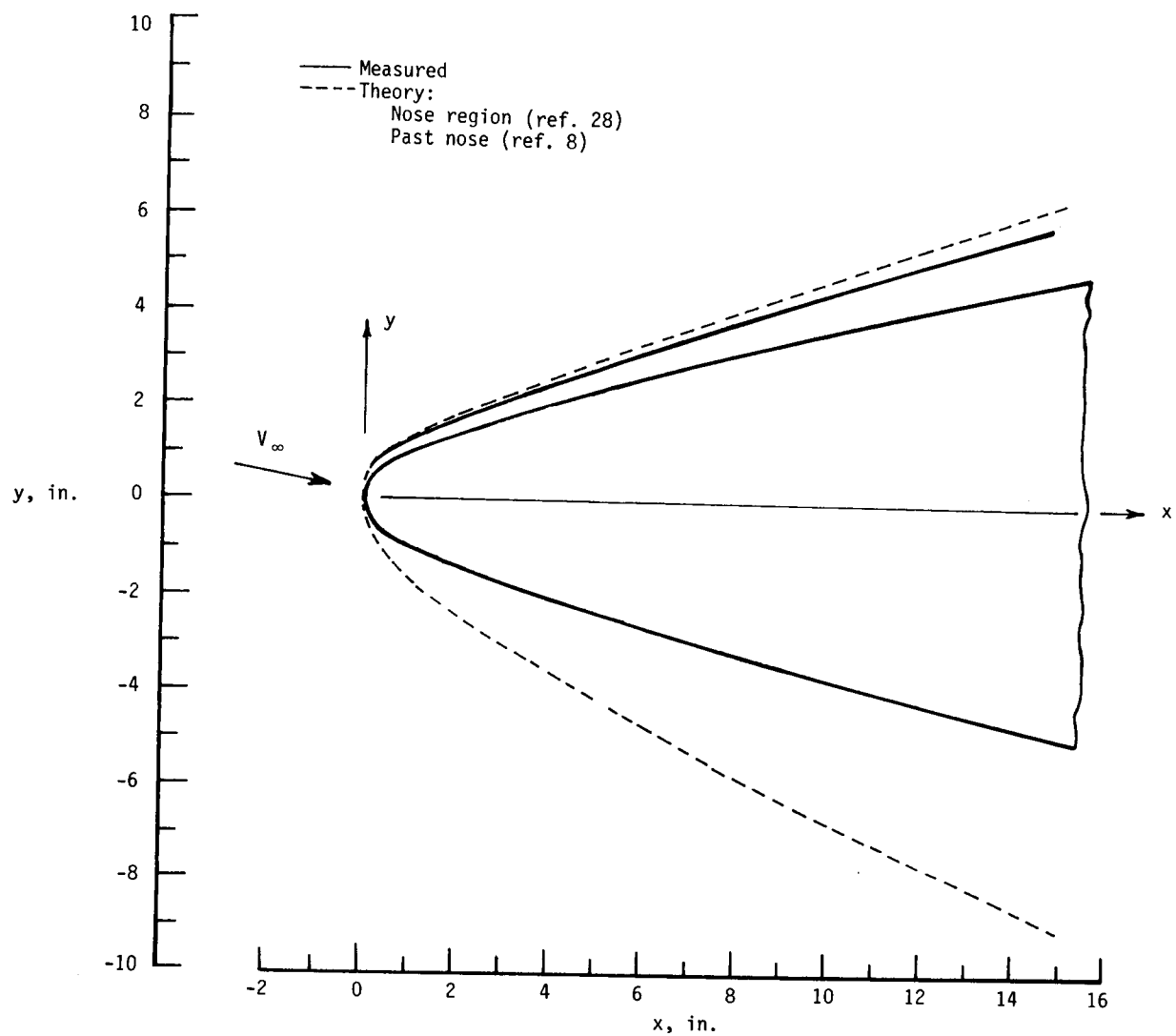
(c) Nose R-1.  $\alpha = 0^\circ$ .

Figure 14.- Continued.



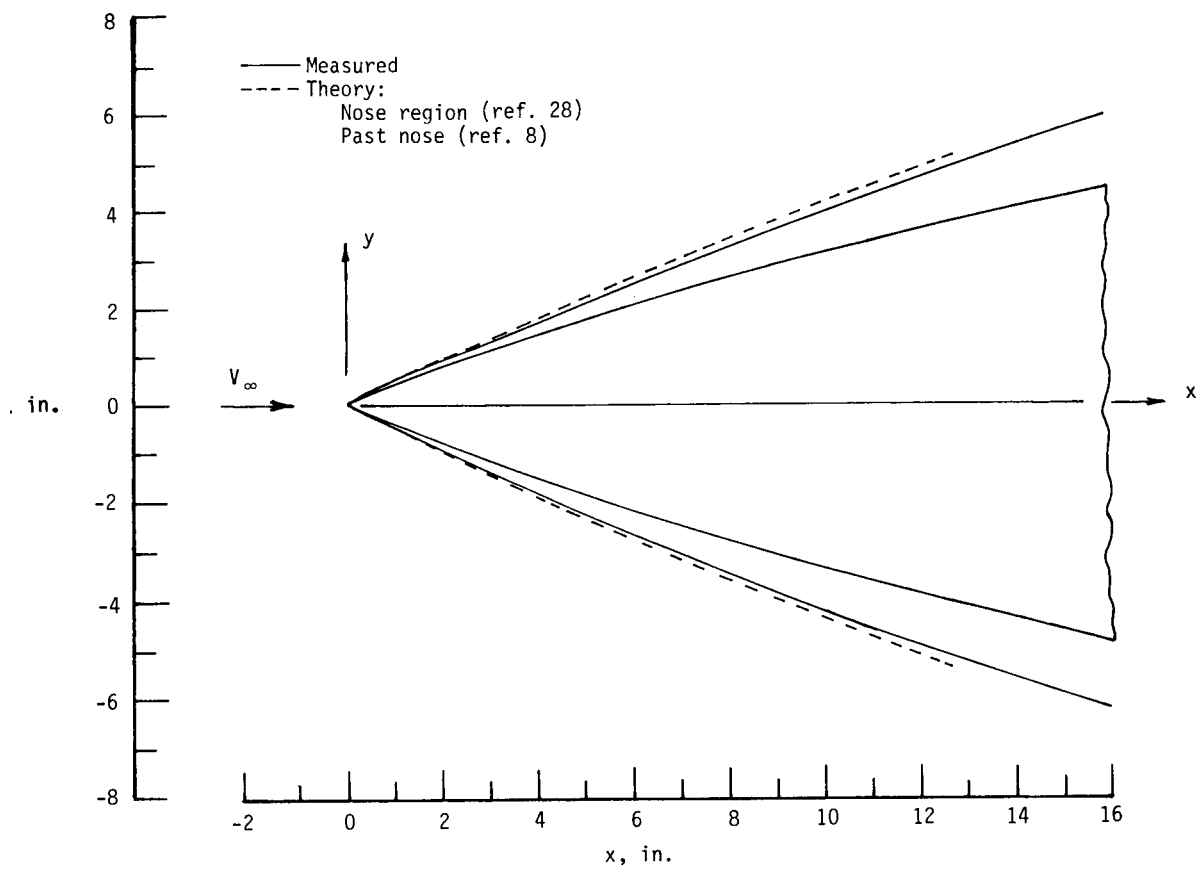
(d) Nose R-1.  $\alpha = 2.5^\circ$ .

Figure 14.- Continued.



(e) Nose R-1.  $\alpha = 10^\circ$ .

Figure 14.- Continued.



(f) Nose R-S.  $\alpha = 0^\circ$ .

Figure 14.- Concluded.



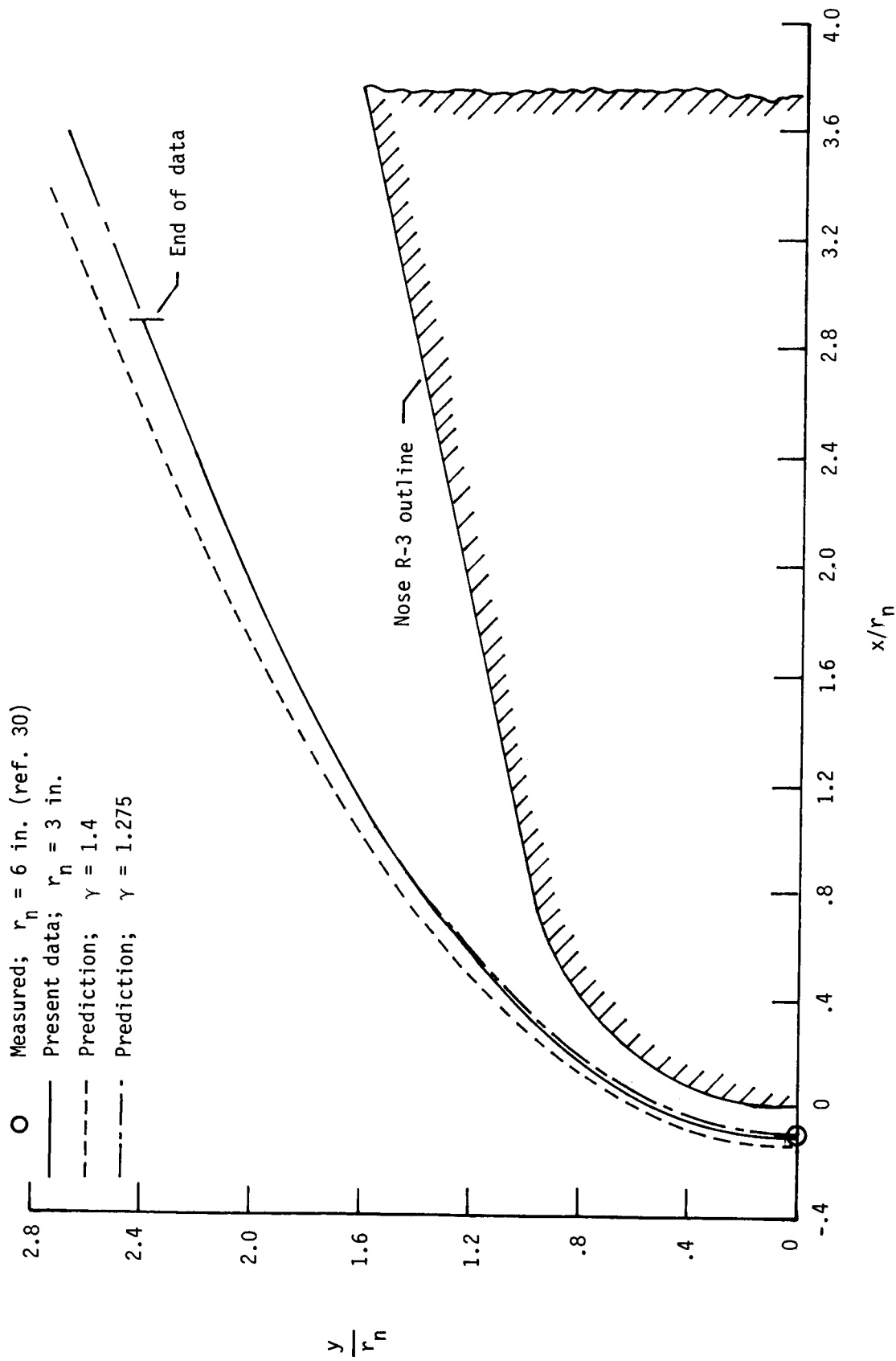
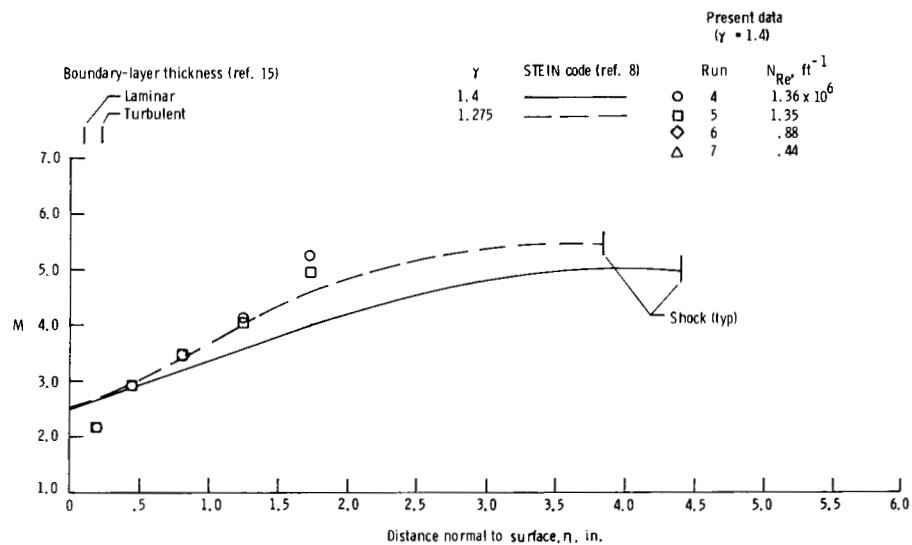
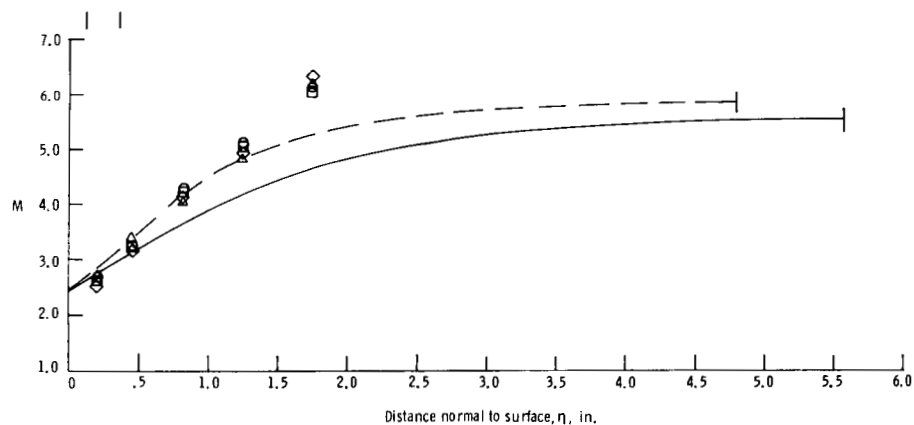


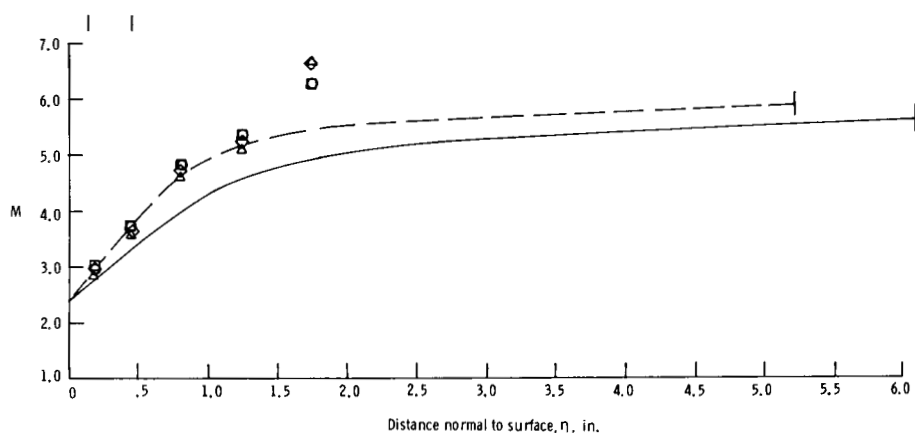
Figure 15.- Normalized shock-standoff distance for nose R-3 at  $\alpha = 0^\circ$ .



(a) Rake 1.  $s_c = 14.8$  in.

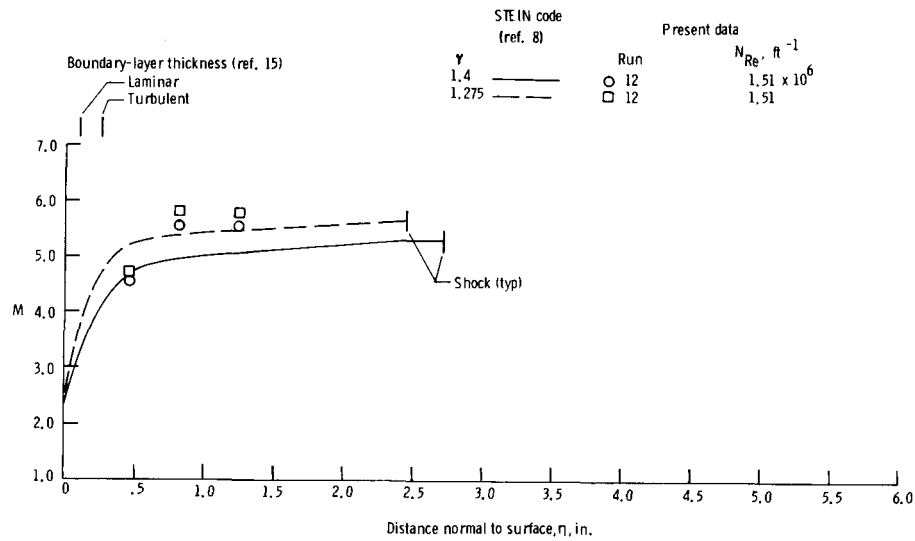


(b) Rake 2.  $s_c = 38.3$  in.

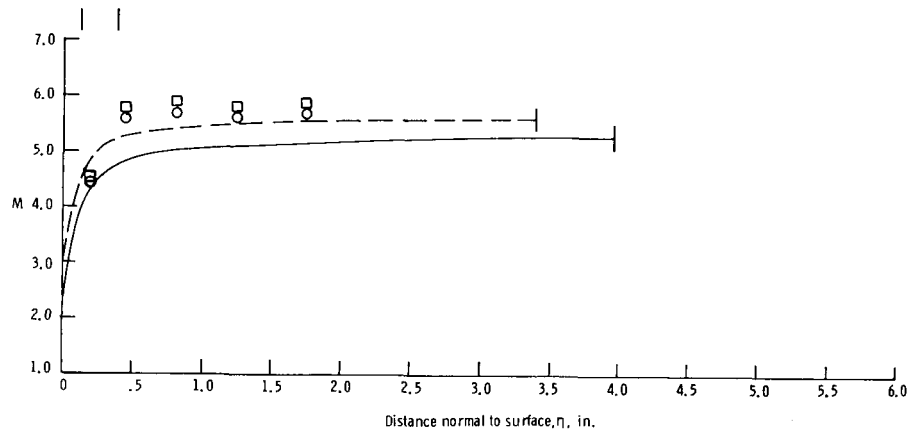


(c) Rake 3.  $s_c = 58.6$  in.

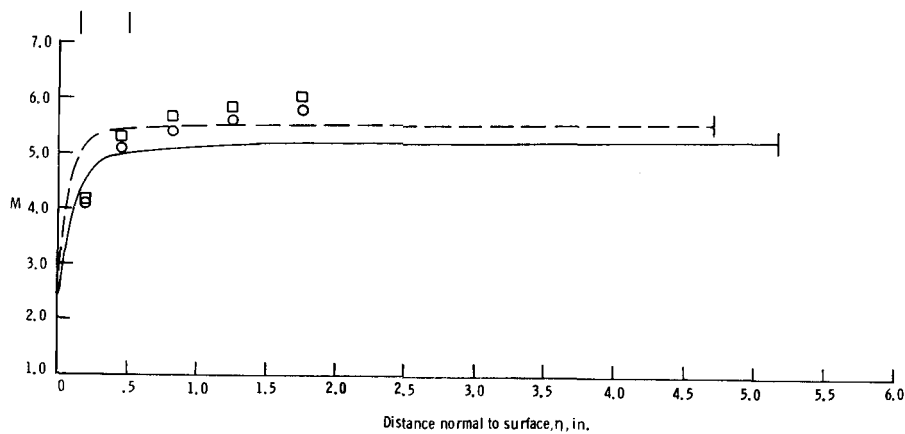
Figure 16.- Mach number profiles for nose R-3 at  $\alpha = 0^\circ$ .



(a) Rake 1.  $s_c = 14.8$  in.



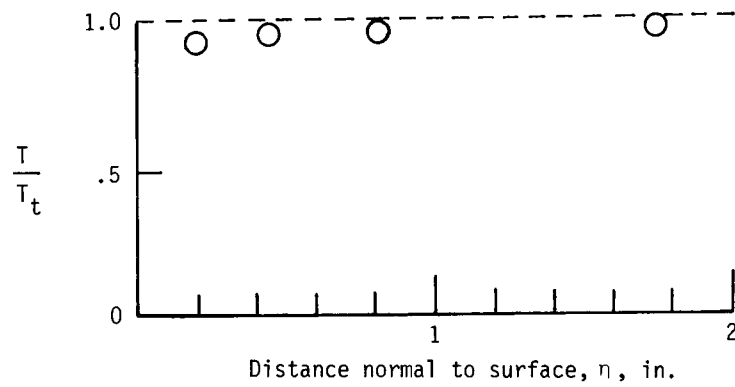
(b) Rake 2.  $s_c = 38.3$  in.



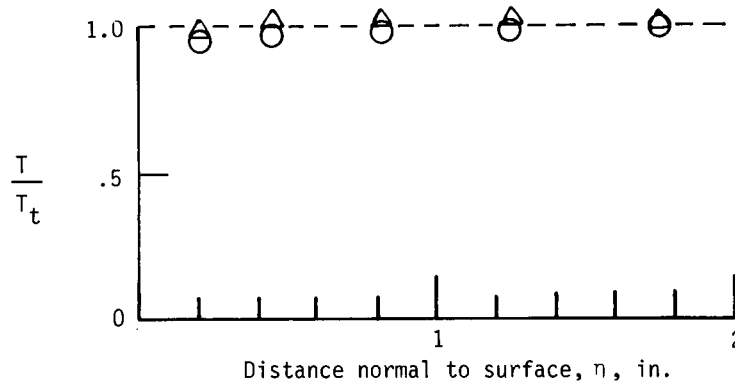
(c) Rake 3.  $s_c = 58.6$  in.

Figure 17.- Mach number profiles for nose R-1 at  $\alpha = 0^\circ$ .

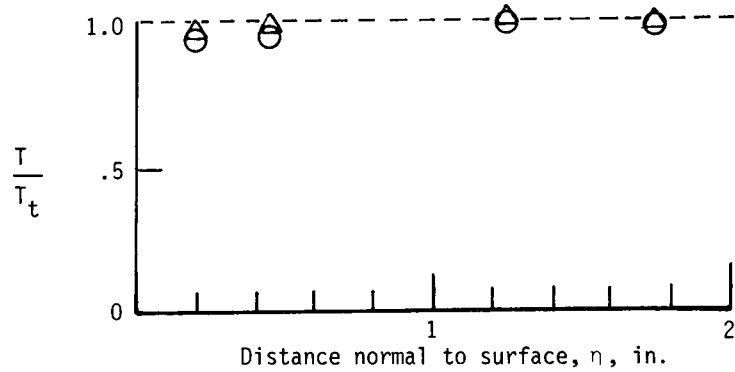
	Run	Nose	$N_{Re}, ft^{-1}$
○	4	R-3	$1.36 \times 10^6$
△	12	R-1	1.51
--- $T/T_t = 1$			



(a) Rake 1.  $s_c = 14.8$  in.;  $\varphi = 45^\circ$ .

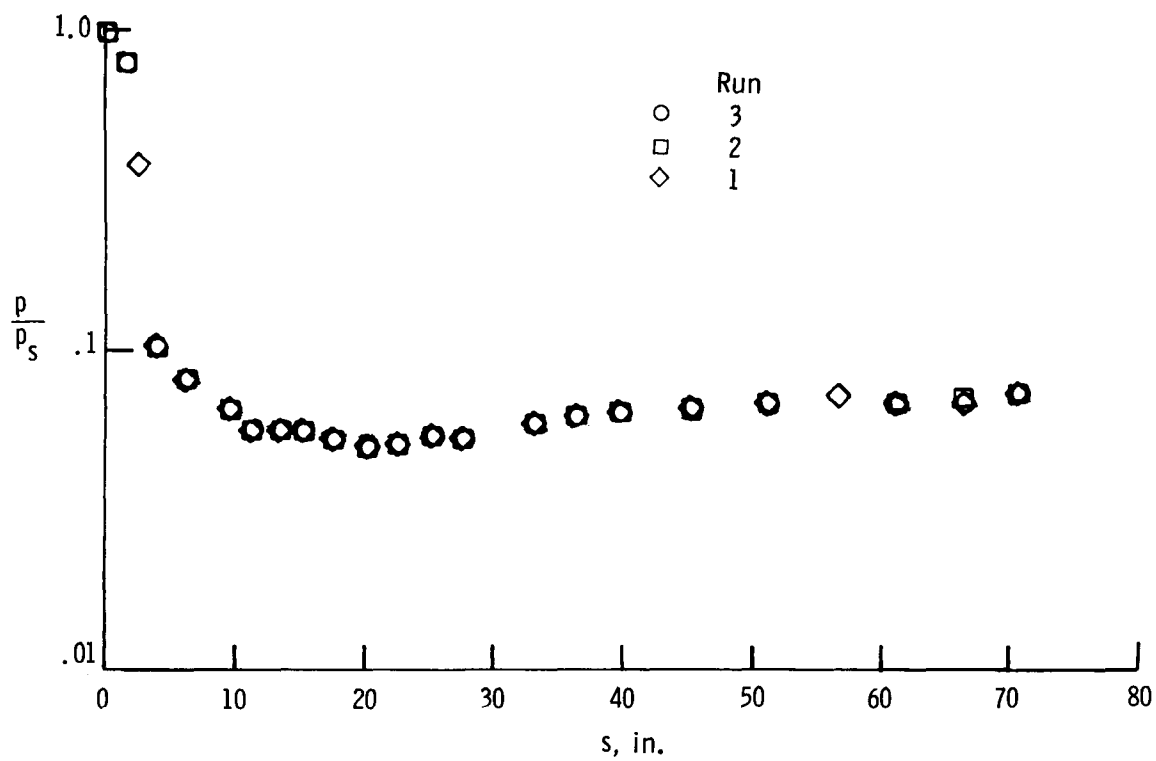


(b) Rake 2.  $s_c = 38.3$  in.;  $\varphi = 90^\circ$ .

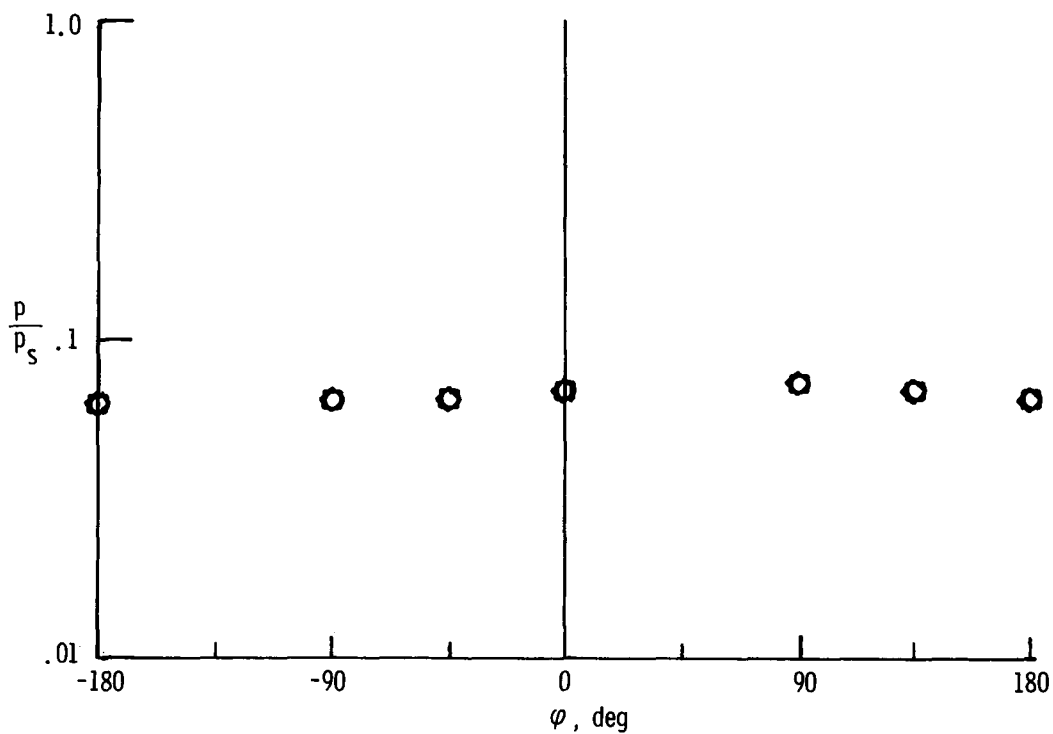


(c) Rake 3.  $s_c = 58.6$  in.;  $\varphi = -135^\circ$ .

Figure 18.- Total-temperature profiles at  $\alpha = 0^\circ$ .



(a) Longitudinal pressure distribution.  $\varphi = 0^\circ$ .



(b) Circumferential pressure distribution.  $s = 66.73$  in.

Figure 19.- Surface-pressure repeatability for blunt cone at  $\alpha = 0^\circ$  for nose R-3.

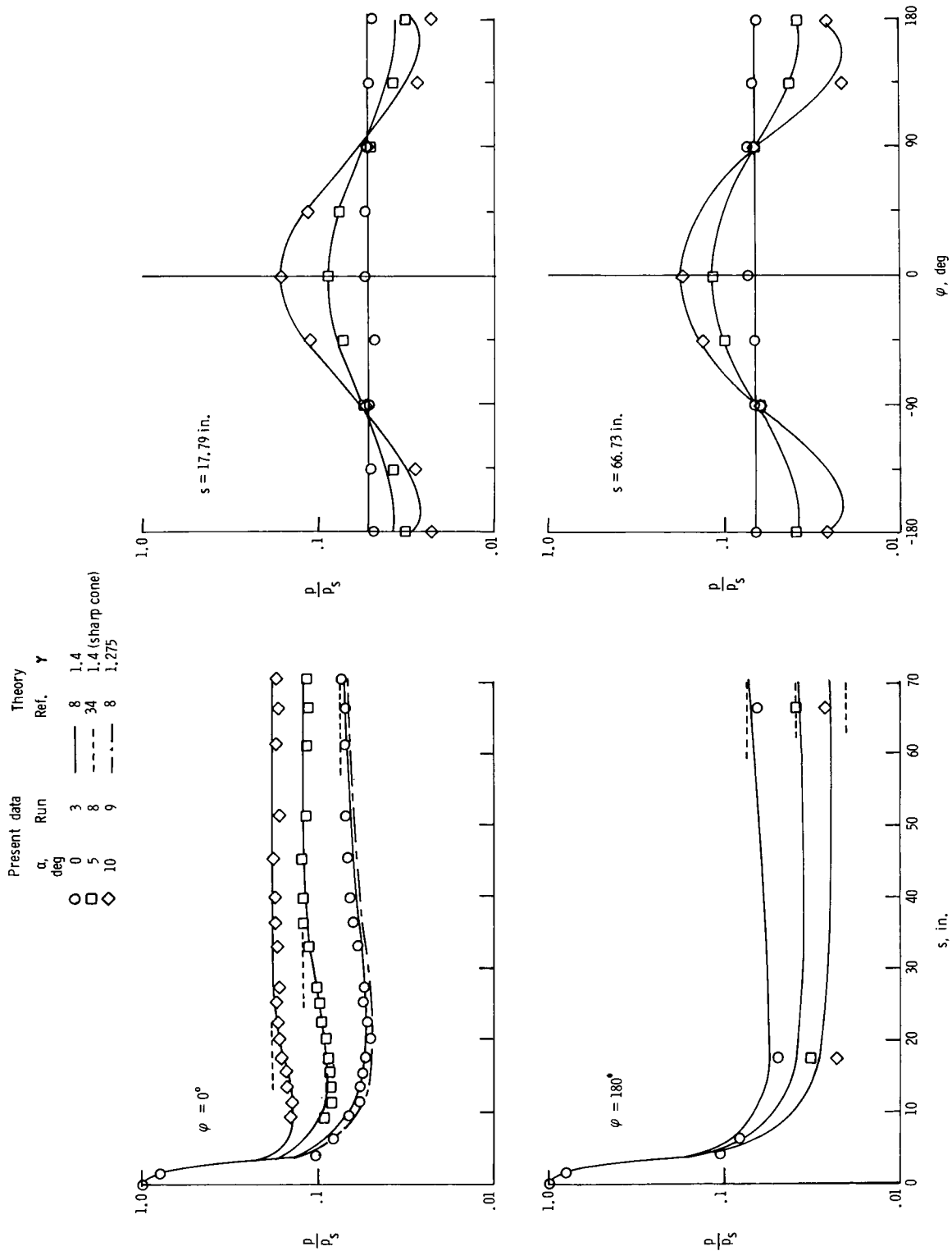
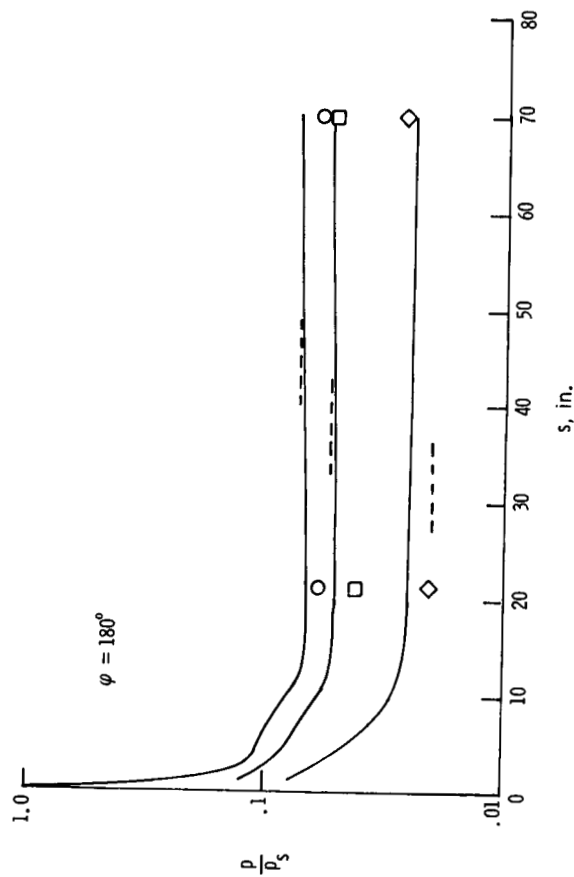
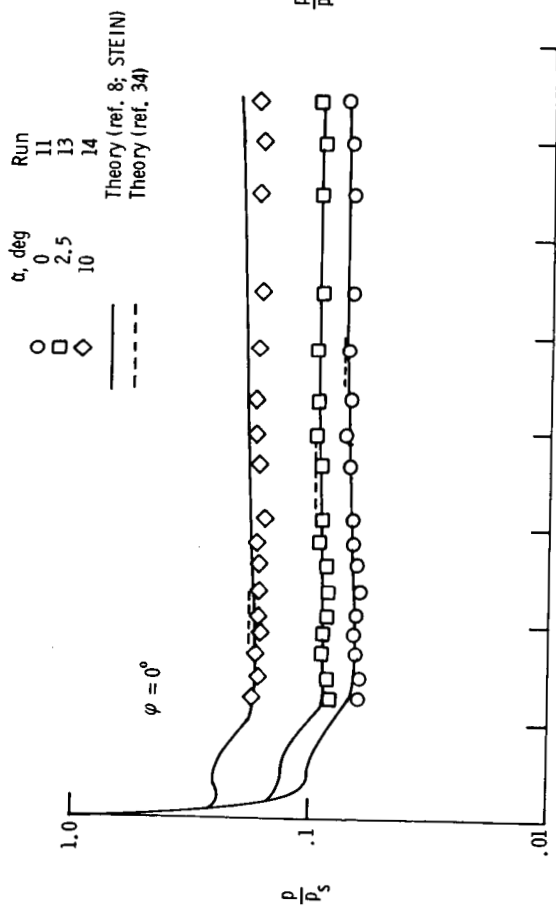
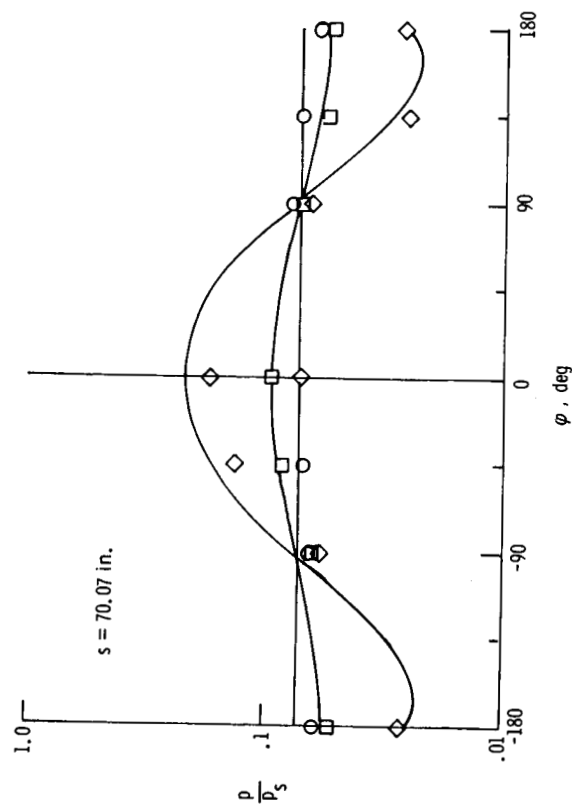
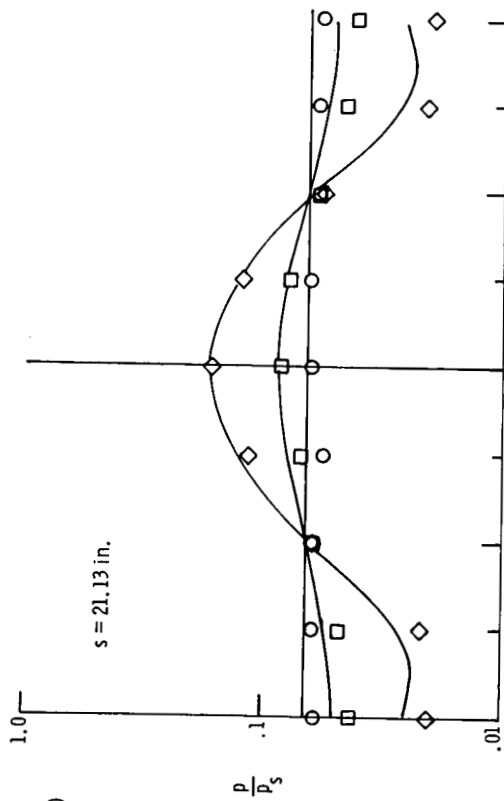


Figure 20.- Surface-pressure distribution for 12.5° cone frustum at various angles of attack for nose R-3.  $N_{Re} = 1.4 \times 10^6$  per foot.

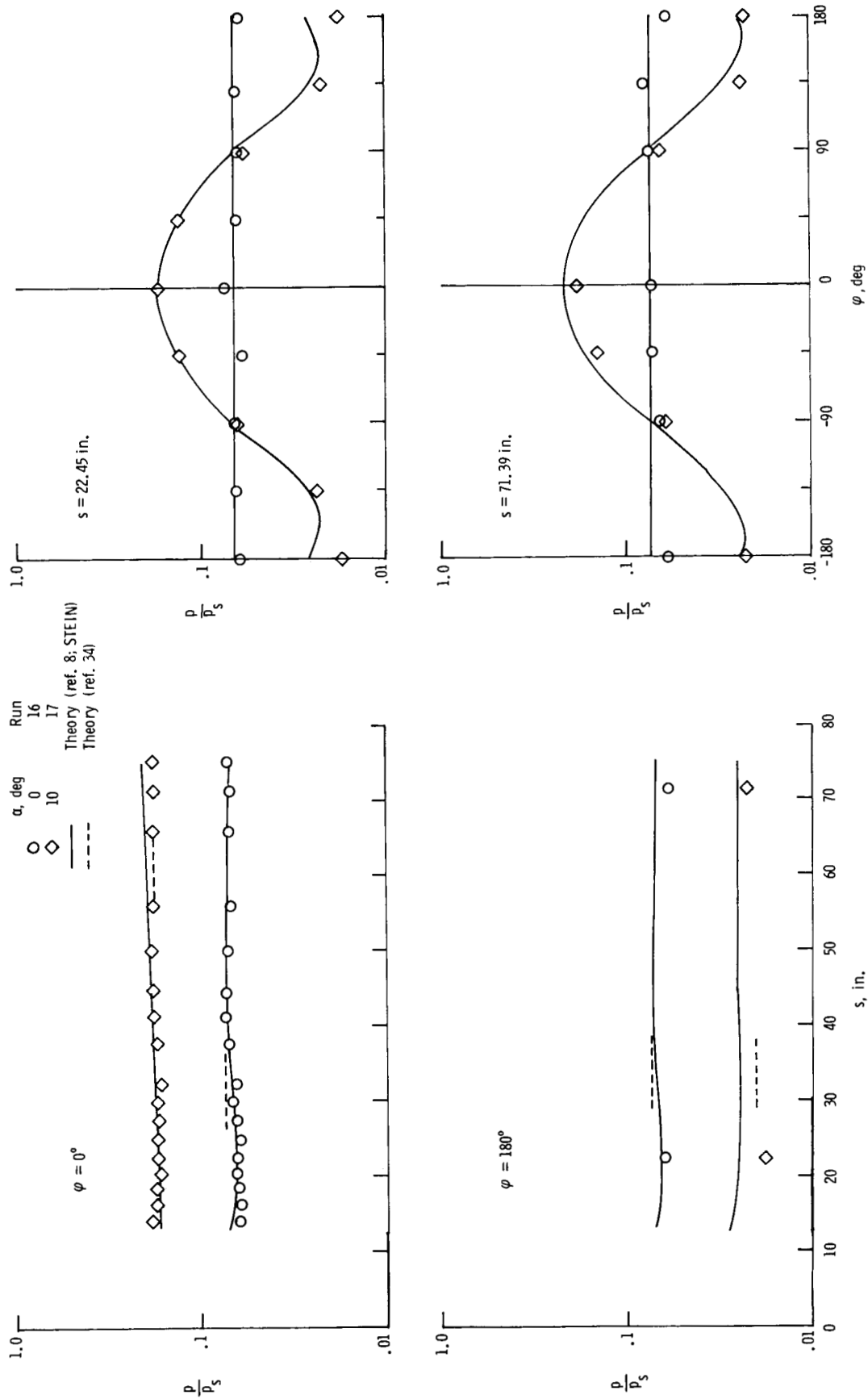


(a) Longitudinal pressure distribution.



(b) Circumferential pressure distribution.

Figure 21.- Surface-pressure distribution for  $12.5^\circ$  cone frustum at various angles of attack for nose R-1.  $N_{Re} = 1.4 \times 10^6$  per foot.

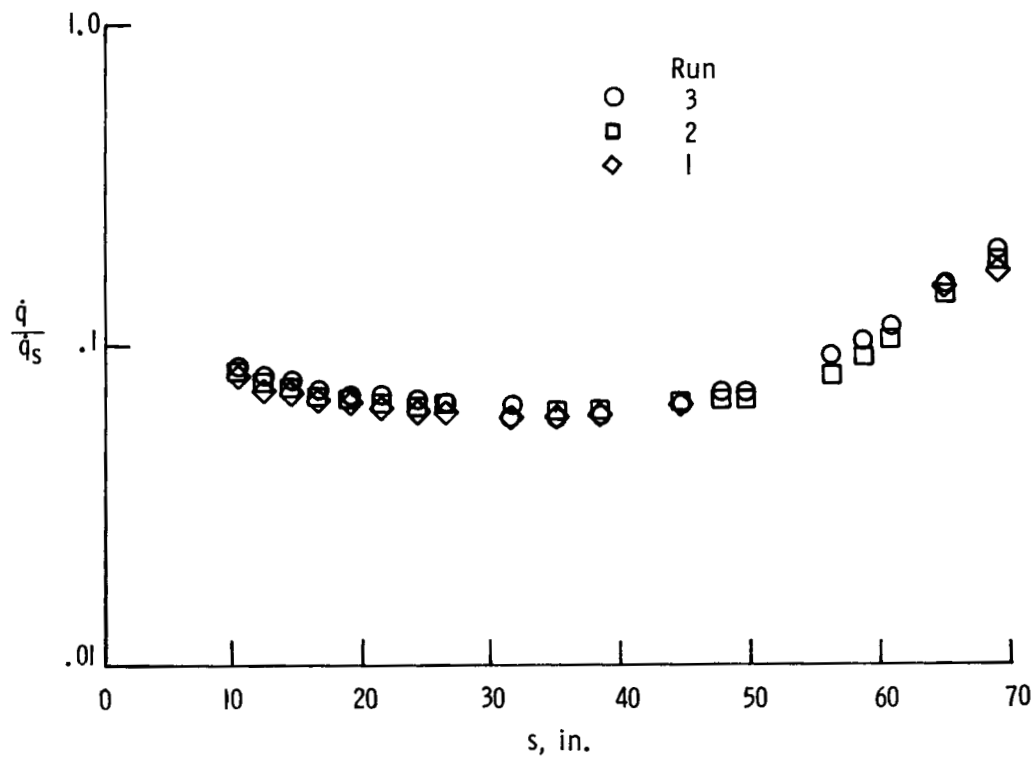


(a) Longitudinal pressure distribution.

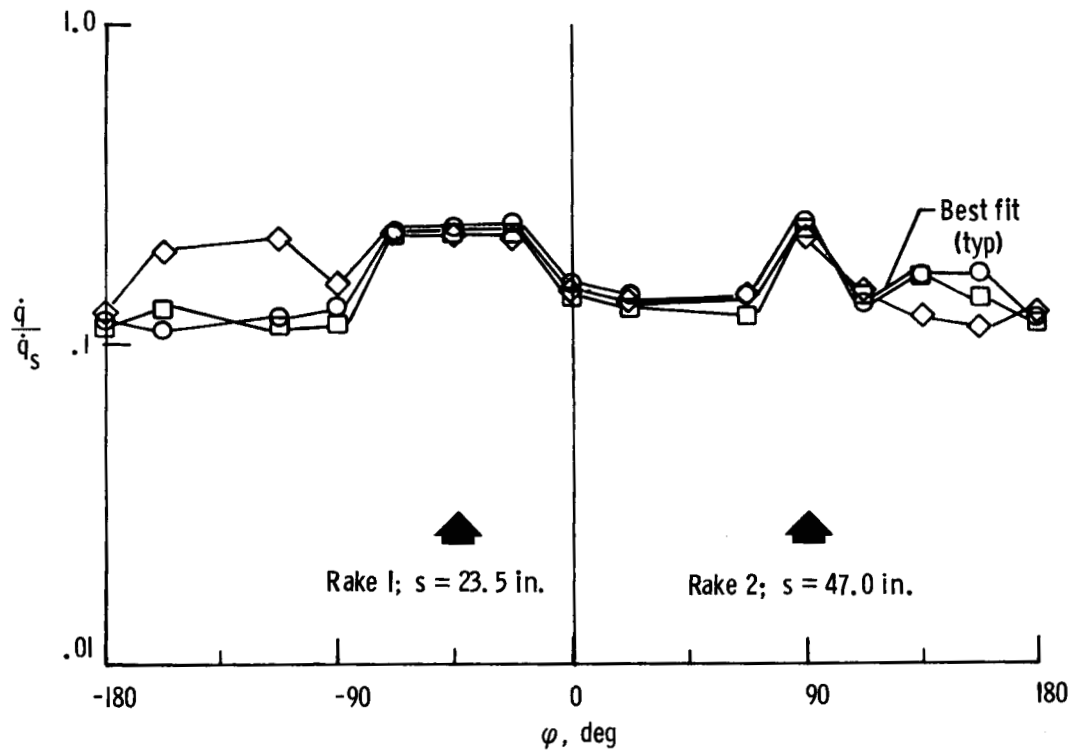
(b) Circumferential pressure distribution.

Figure 22.- Surface-pressure distribution for 12.5° cone frustum at various angles of attack for nose R-S.  $N_{Re} = 1.4 \times 10^6$  per foot.





(a) Longitudinal heating distributions.  $\phi = 0^\circ$ .



(b) Circumferential heating distributions.  $s = 65.95$  in.

Figure 23.- Cold-wall heat-flux repeatability for blunt cone at  $\alpha = 0^\circ$  for nose R-3.  $N_{Re} = 1.4 \times 10^6$  per foot.

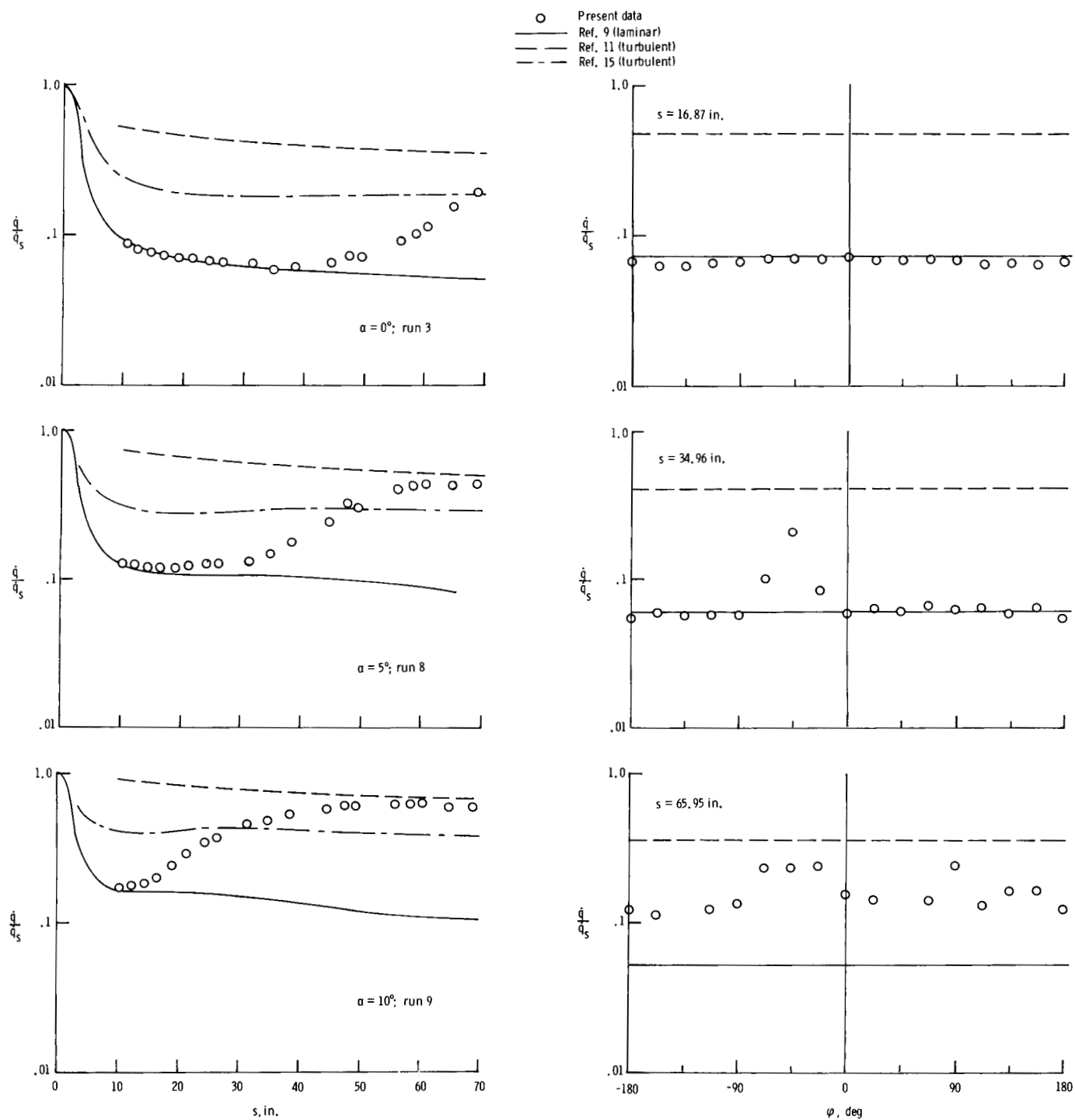
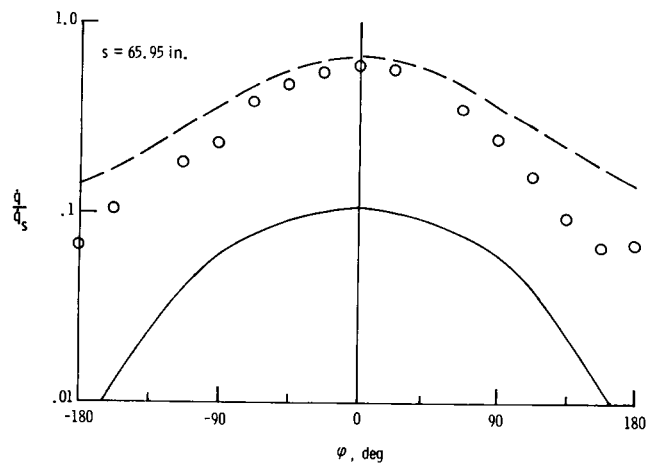
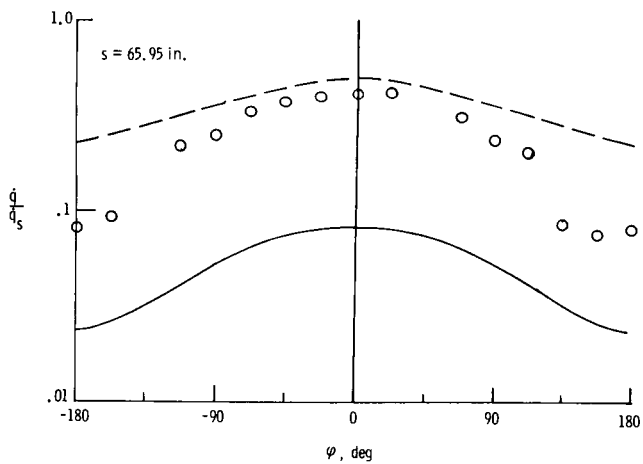
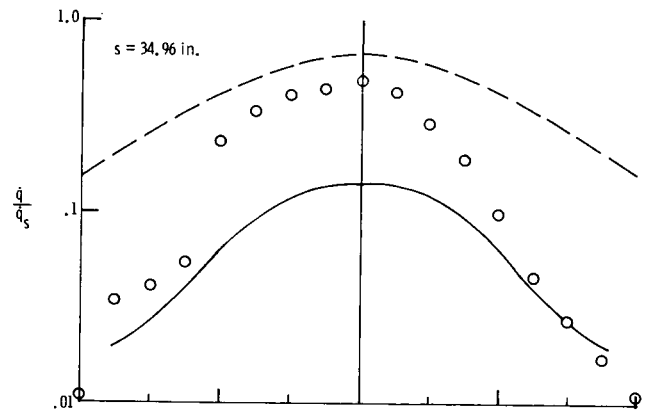
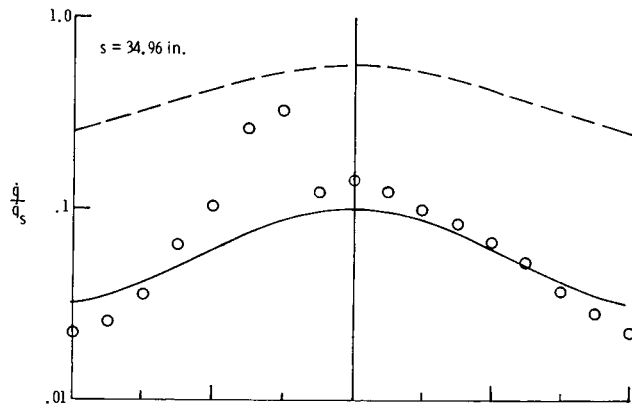
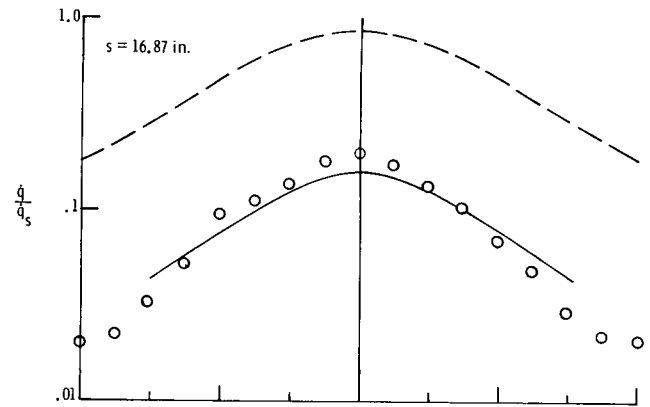
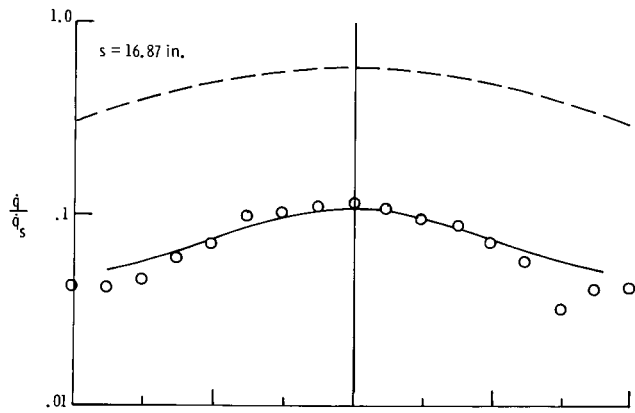


Figure 24.- Longitudinal and circumferential heating-rate distributions at various angles of attack for nose R-3.  $N_{Re} = 1.4 \times 10^6$  per foot.

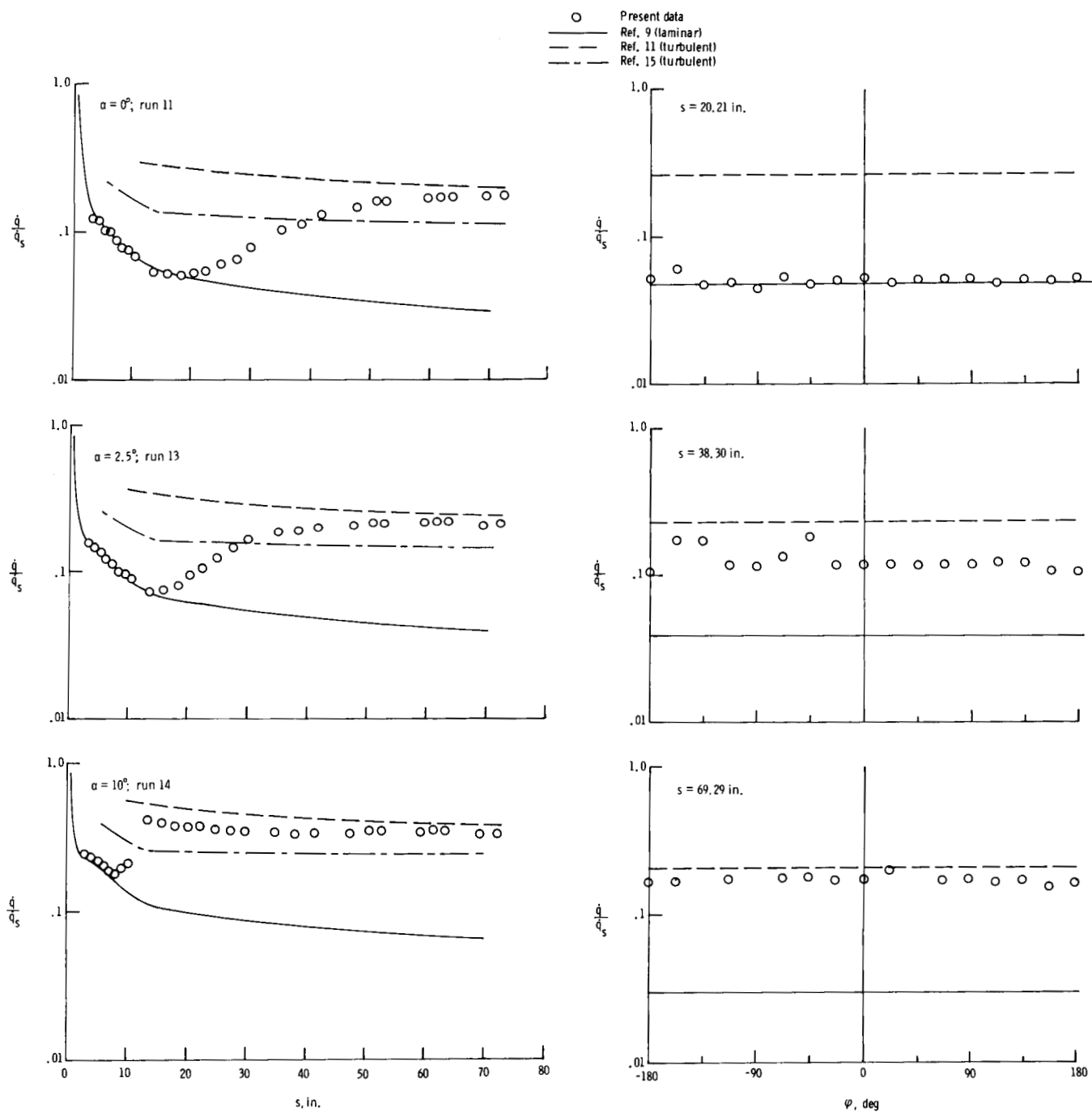
○ Present data  
 — Ref. 9 (laminar)  
 - - - Ref. 11 (turbulent)



(c)  $\alpha = 5^\circ$ ; run 8.

(d)  $\alpha = 10^\circ$ ; run 9.

Figure 24.- Concluded.

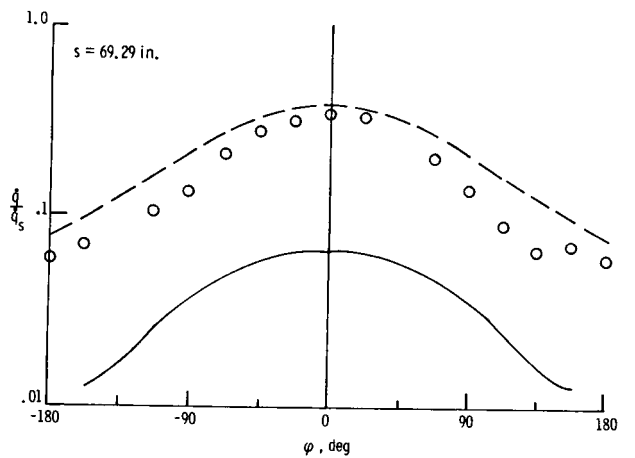
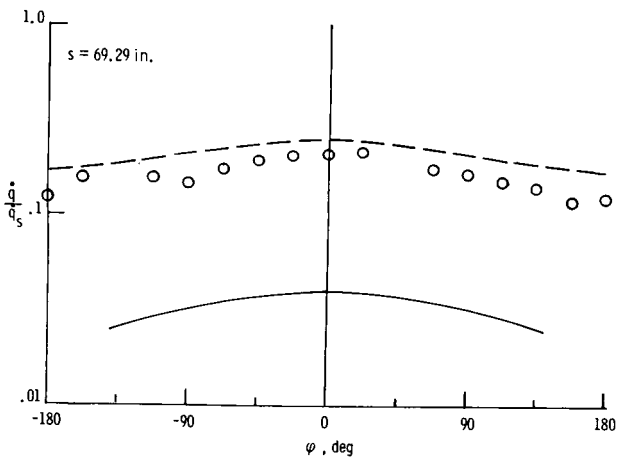
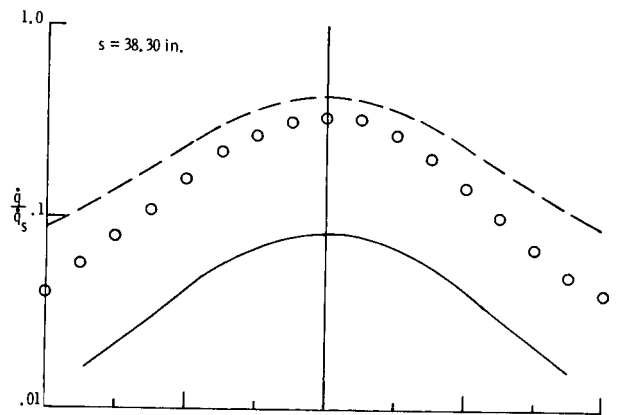
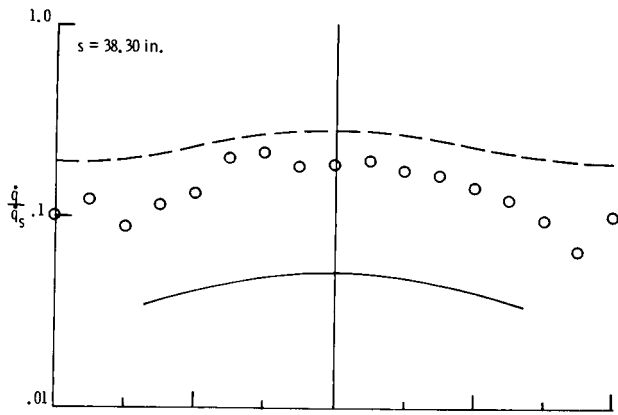
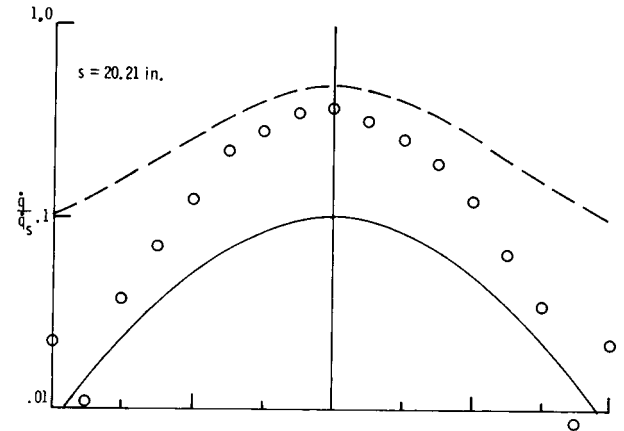
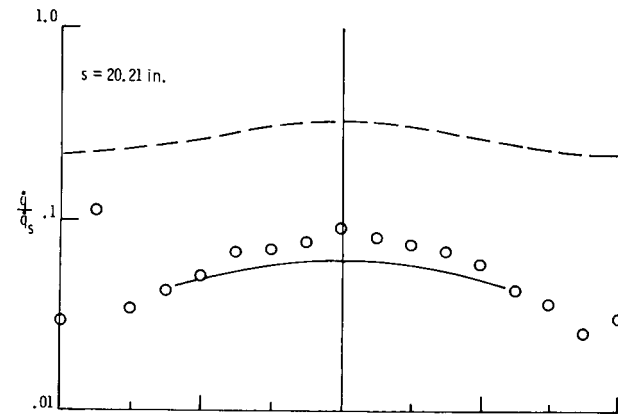


(a)  $\phi = 0^\circ$ .

(b)  $\alpha = 0^\circ$ ; run 11.

Figure 25.- Longitudinal and circumferential heating-rate distributions for 12.5° cone frustum at various angles of attack for nose R-1.  
 $N_{Re} = 1.4 \times 10^6$  per foot.

○ Present data  
 — Ref. 9 (laminar)  
 - - - Ref. 11 (turbulent)



(c)  $\alpha = 2.5^\circ$ ; run 13.

(d)  $\alpha = 10^\circ$ ; run 14.

Figure 25.- Concluded.

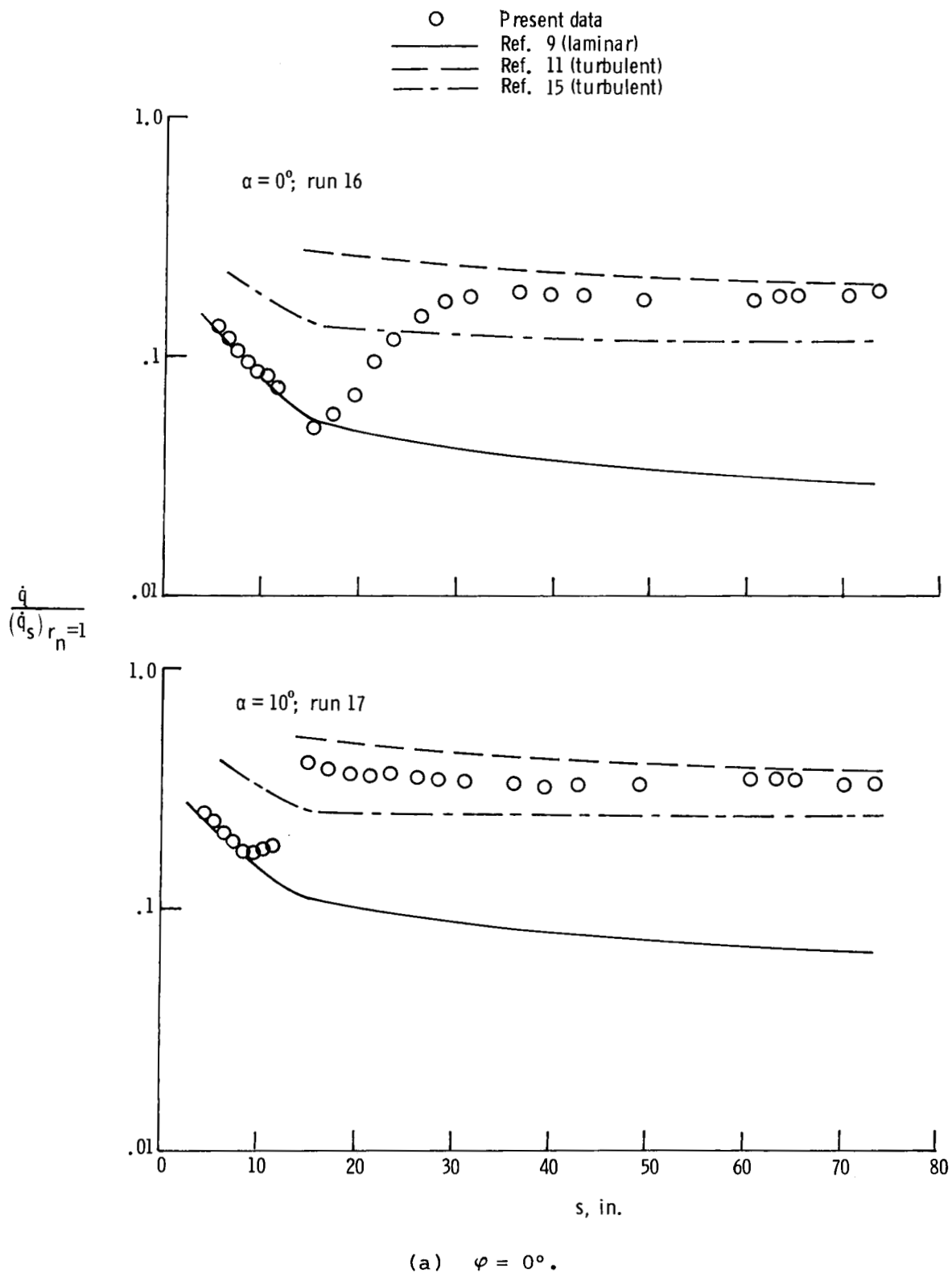
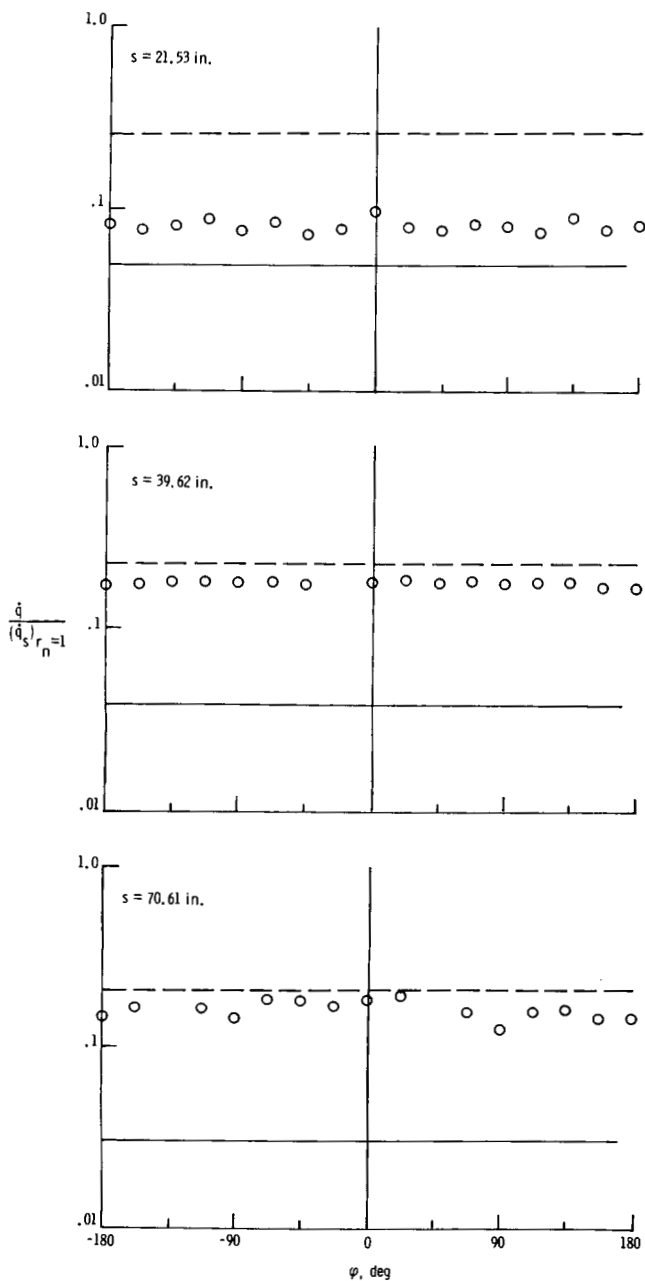
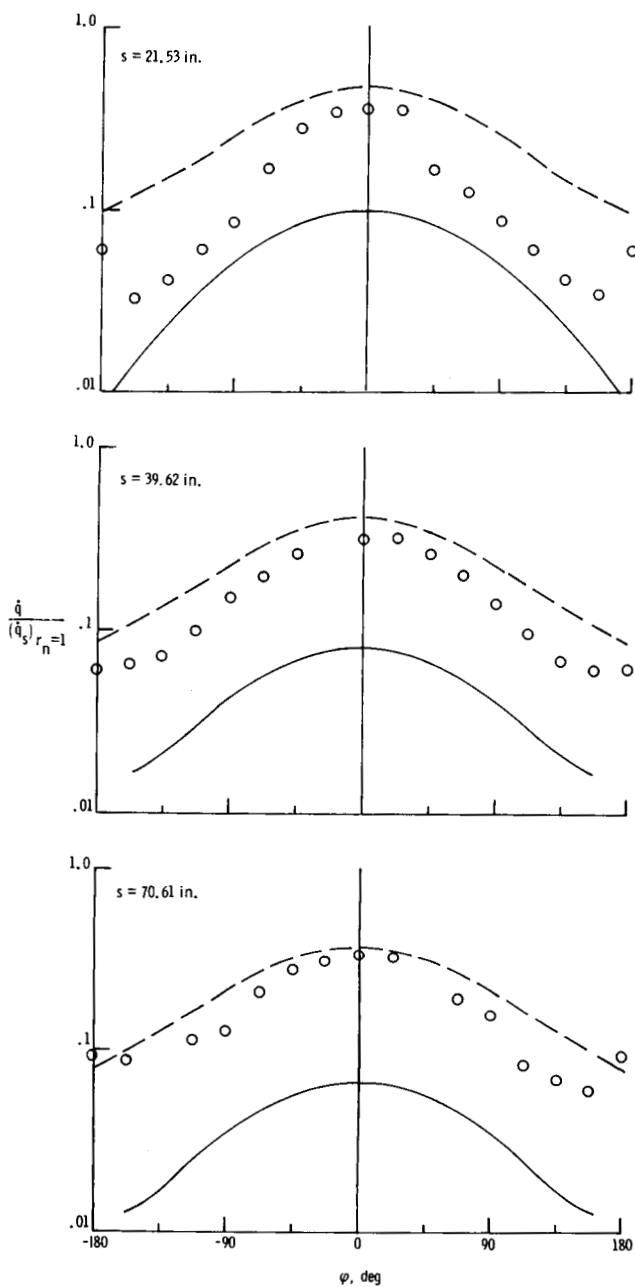


Figure 26.- Longitudinal and circumferential heating-rate distributions for  $12.5^\circ$  cone frustum at various angles of attack for nose R-S.  $N_{Re} = 1.4 \times 10^6$  per foot.

○ Present data  
 — Ref. 9 (laminar)  
 - - - Ref. 11 (turbulent)

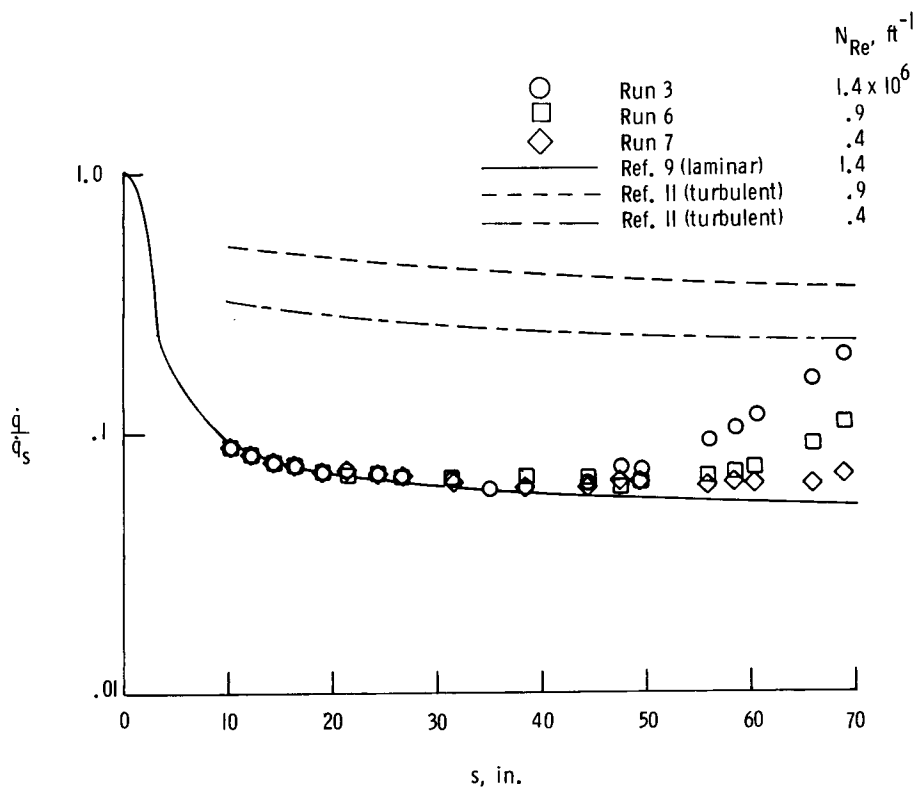
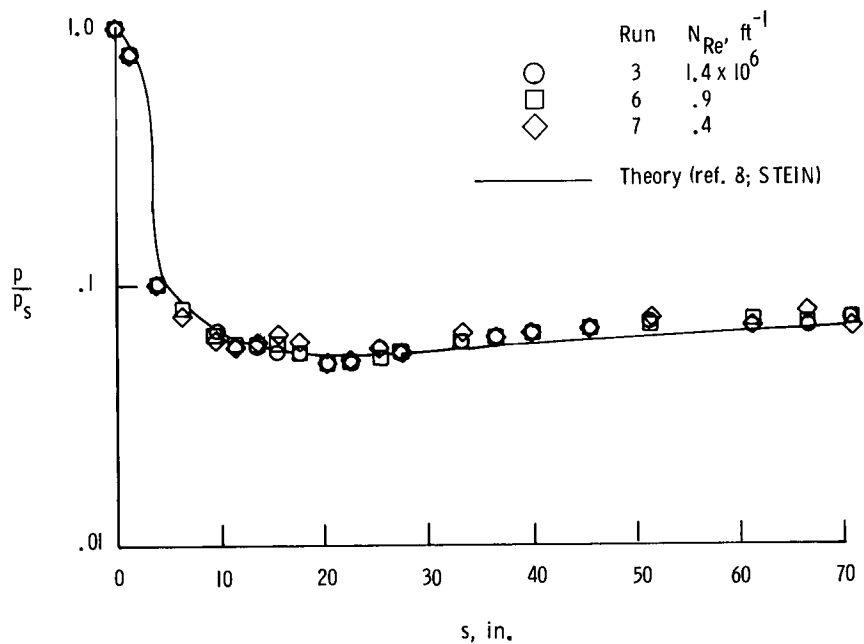


(b)  $\alpha = 0^\circ$ ; run 16.



(c)  $\alpha = 0^\circ$ ; run 17.

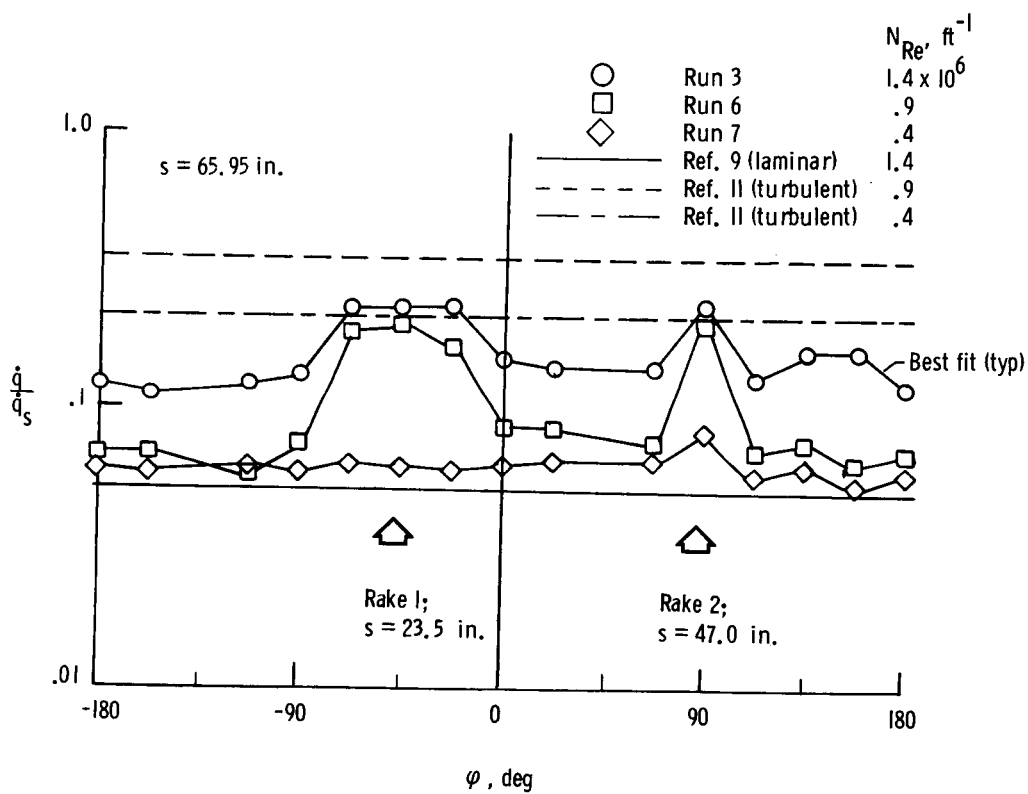
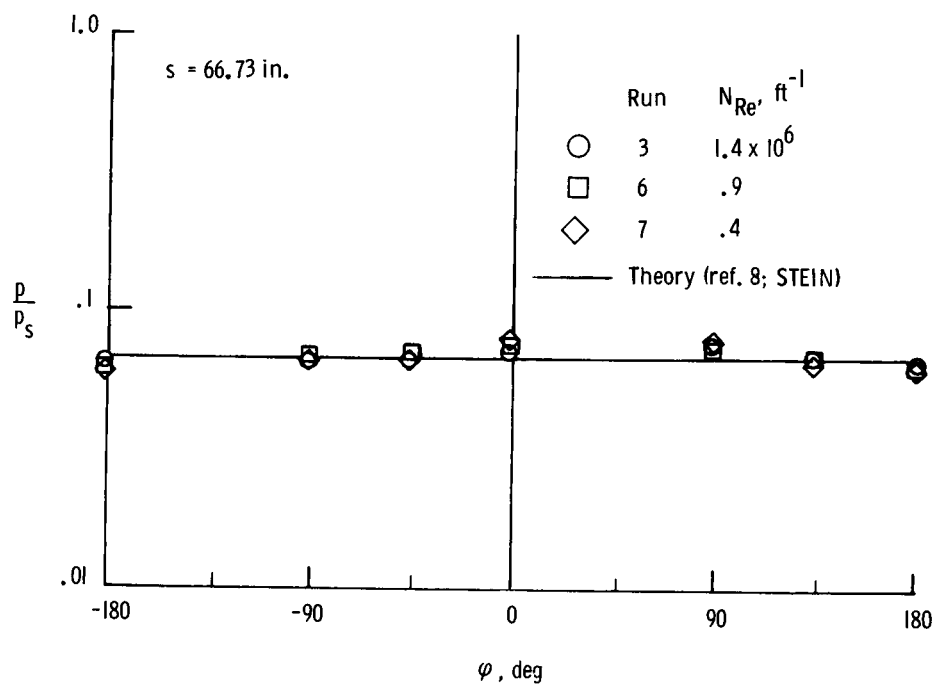
Figure 26.- Concluded.



(a) Longitudinal distributions.  $\varphi = 0^\circ$ .

Figure 27.- Effect of Reynolds number on surface pressures and heating-rate distributions on blunt  $12.5^\circ$  cone frustum at  $\alpha = 0^\circ$  for nose R-3.





(b) Circumferential distributions.

Figure 27.- Concluded.

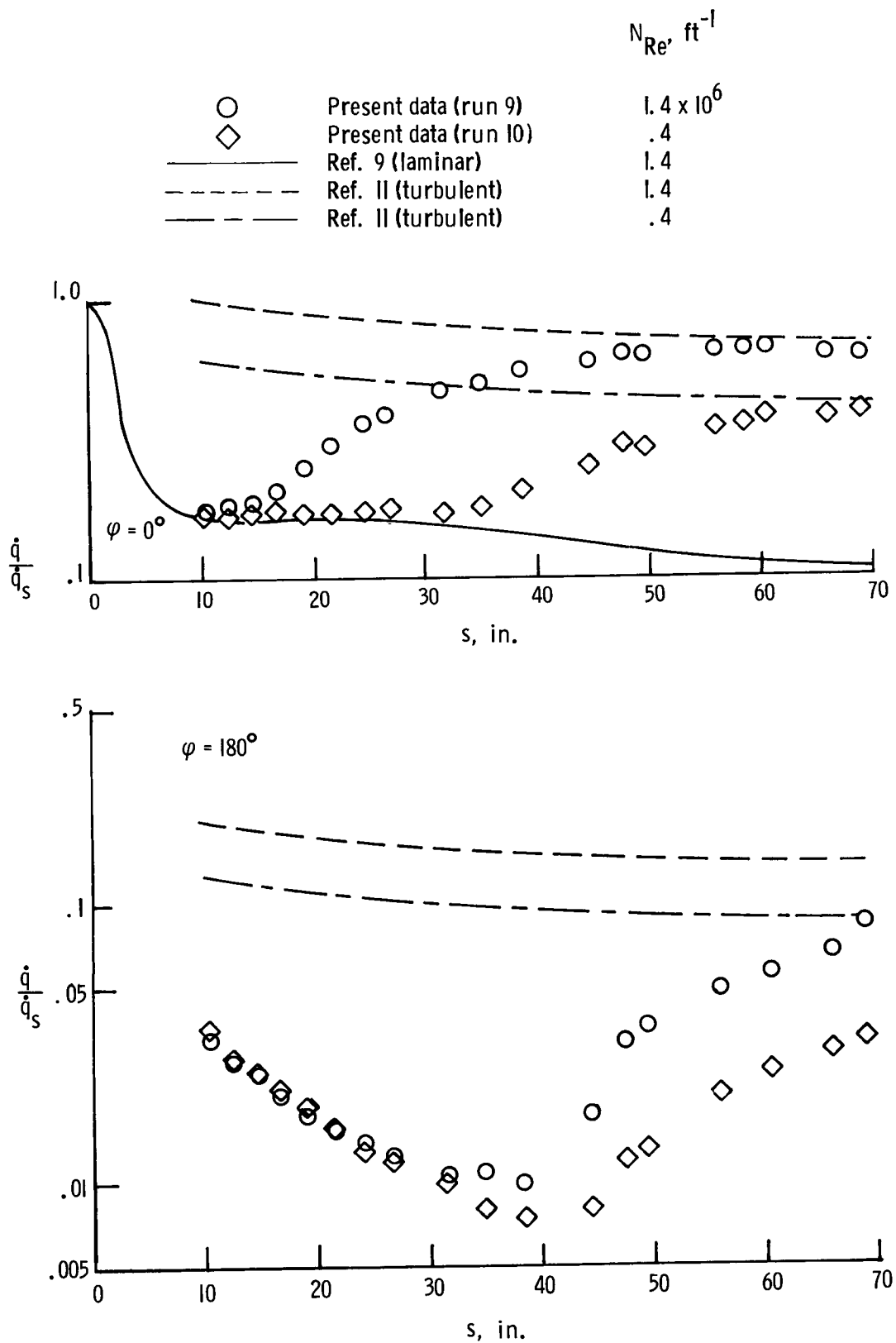
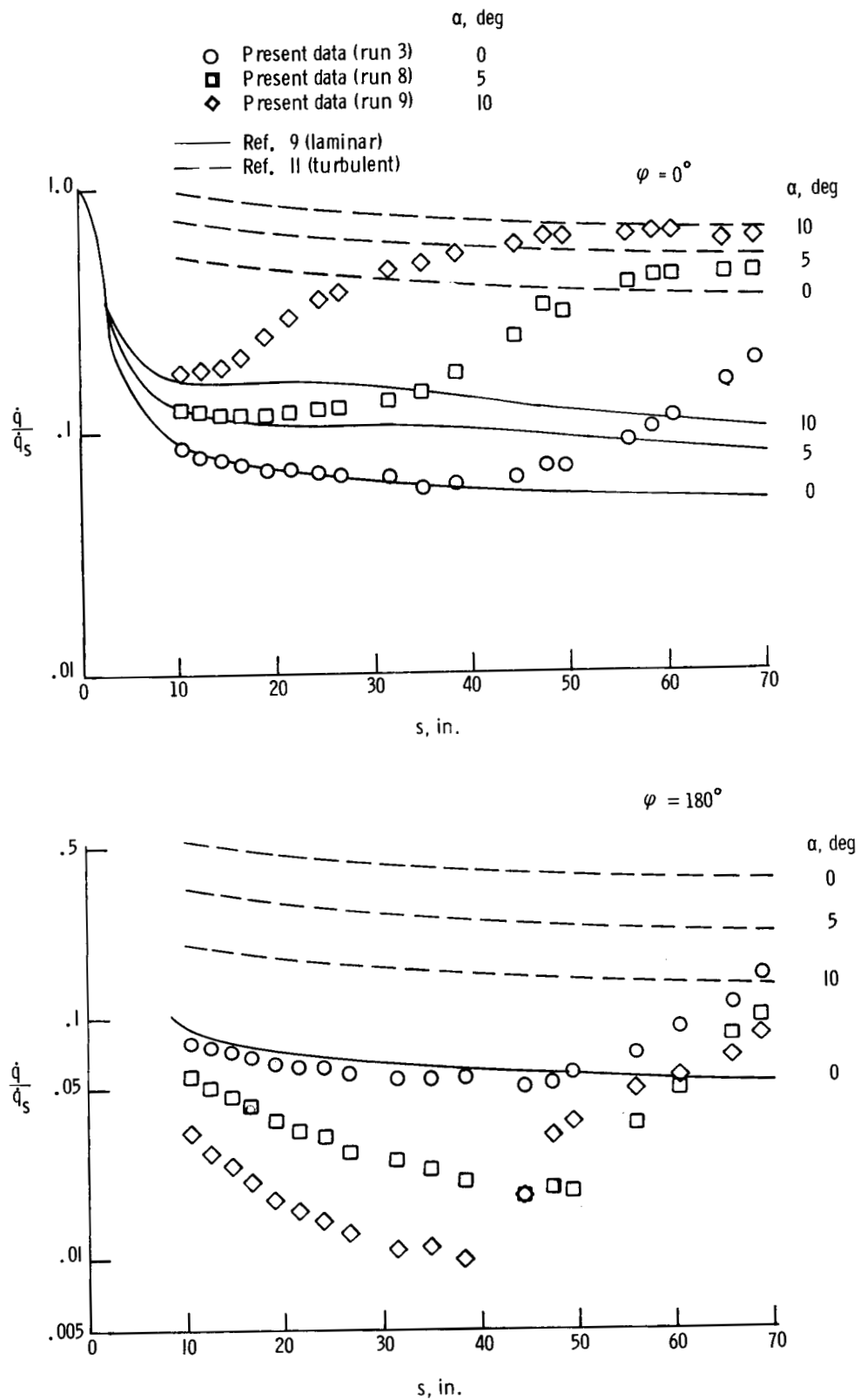
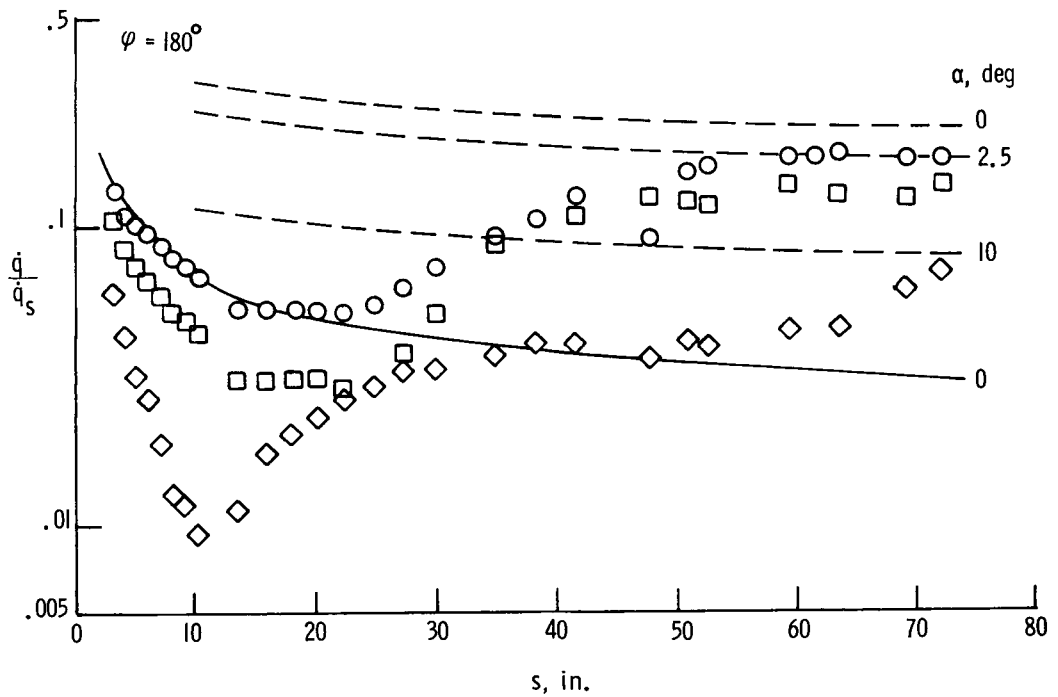
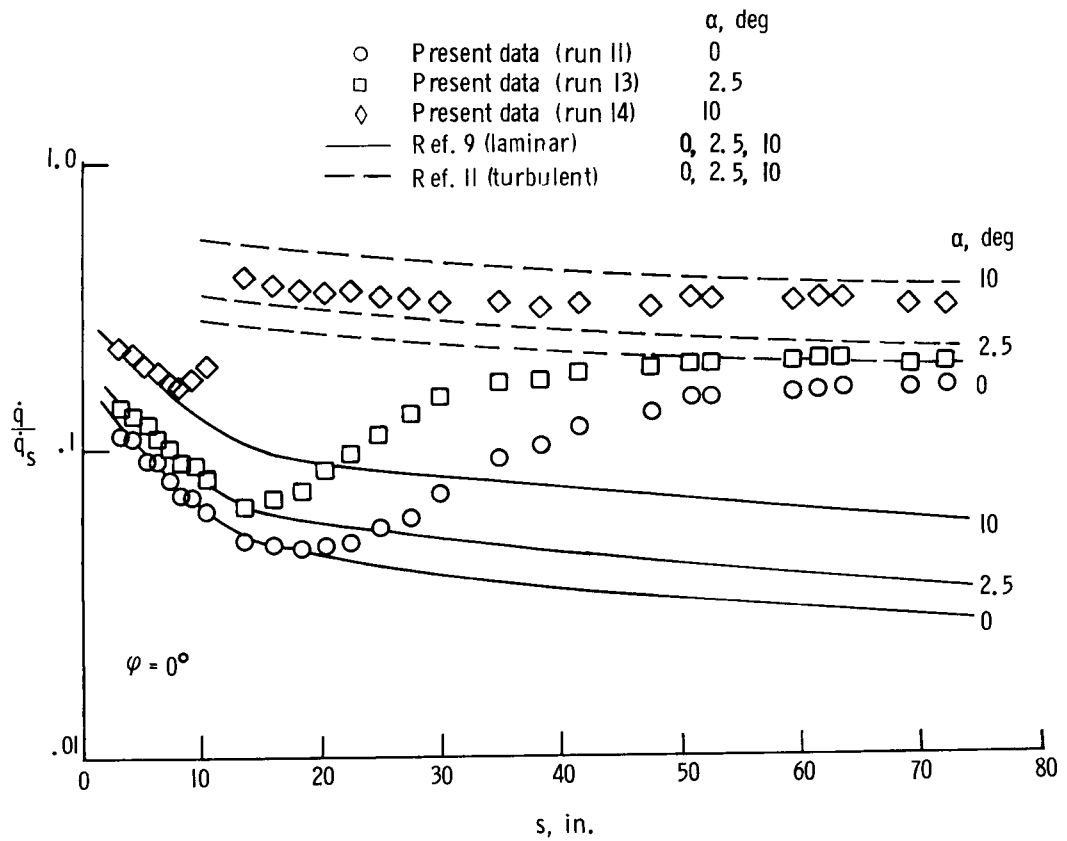


Figure 28.- Effect of Reynolds number on surface heating-rate distributions on blunt  $12.5^\circ$  cone frustum at  $\alpha = 10^\circ$  for nose R-3.



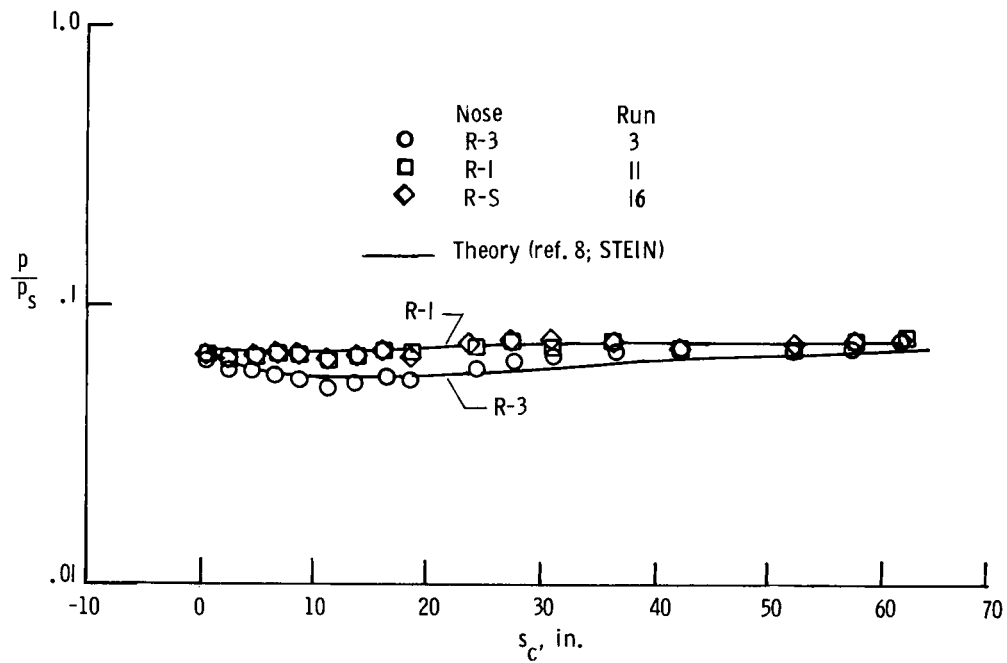
(a) Nose R-3.

Figure 29.- Effect of angle of attack on surface heating-rate distributions on 12.5° cone frustum.

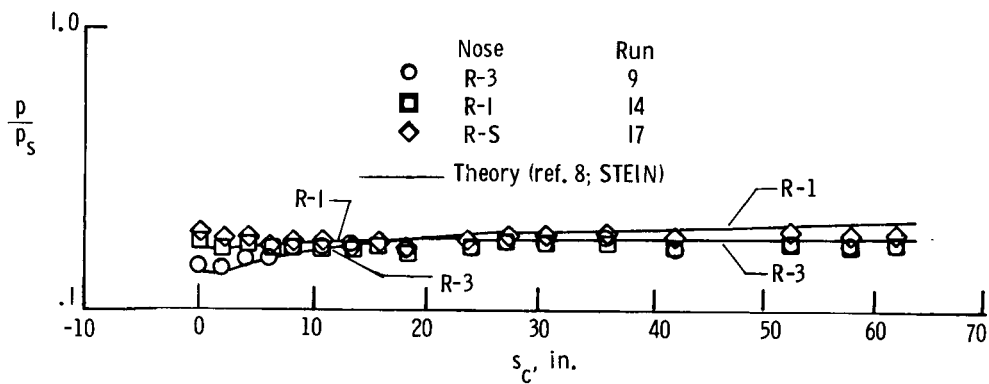


(b) Nose R-1.

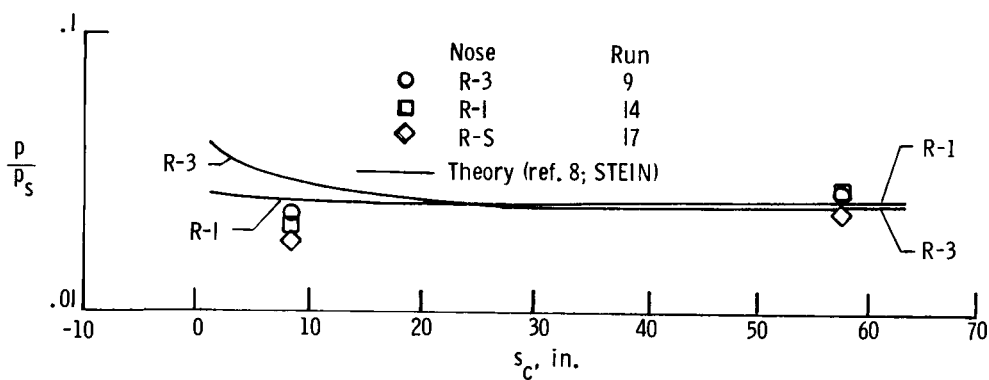
Figure 29.- Concluded.



(a)  $\alpha = 0^\circ$ ;  $\varphi = 0^\circ$ .

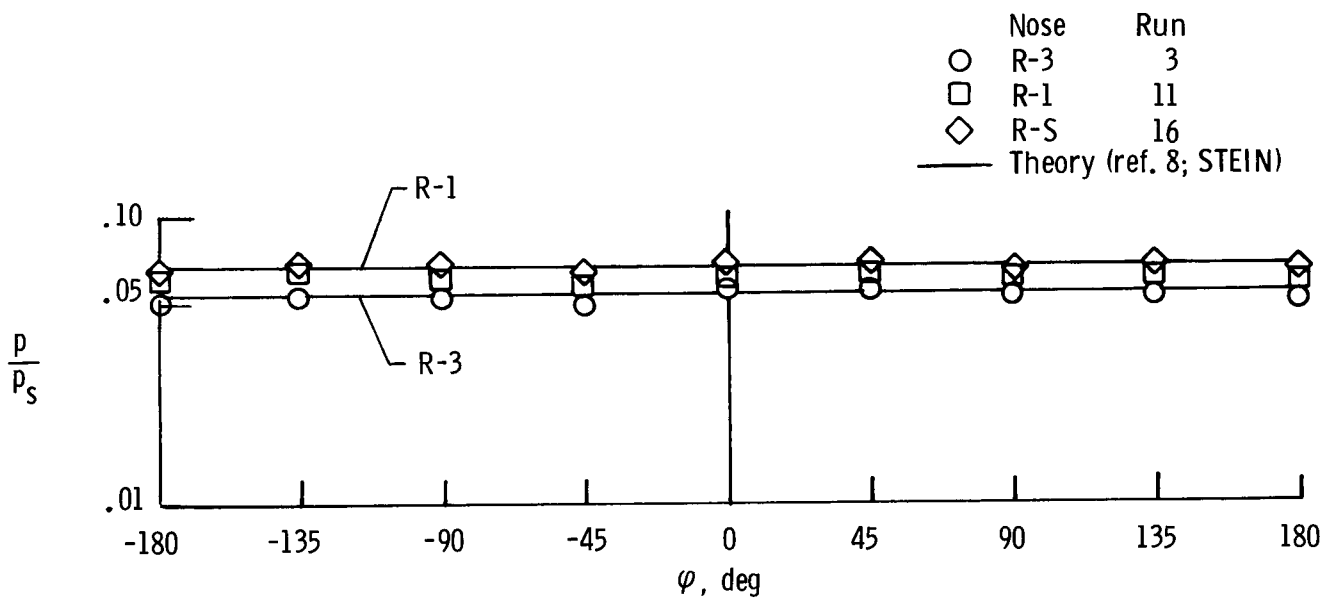


(b)  $\alpha = 10^\circ$ ;  $\varphi = 0^\circ$ .

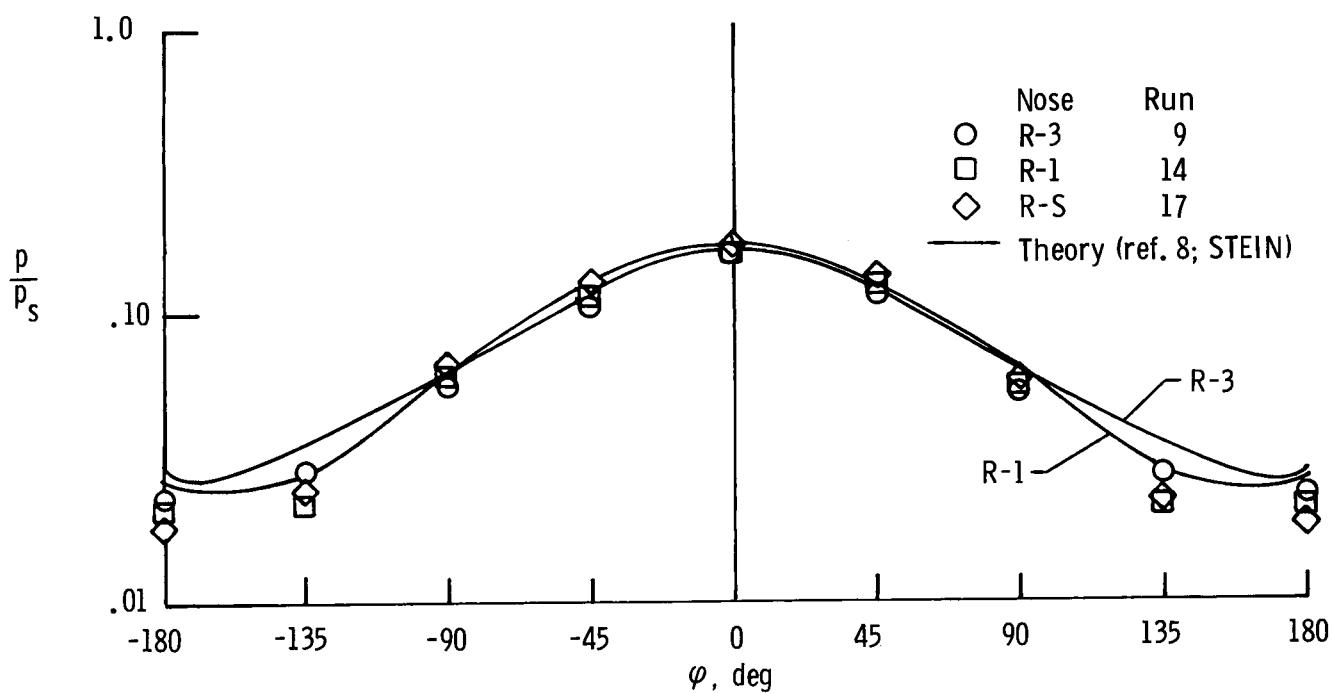


(c)  $\alpha = 10^\circ$ ;  $\varphi = 180^\circ$ .

Figure 30.- Effect of bluntness on longitudinal pressure distribution.  
 $N_{Re} = 1.4 \times 10^6$  per foot.

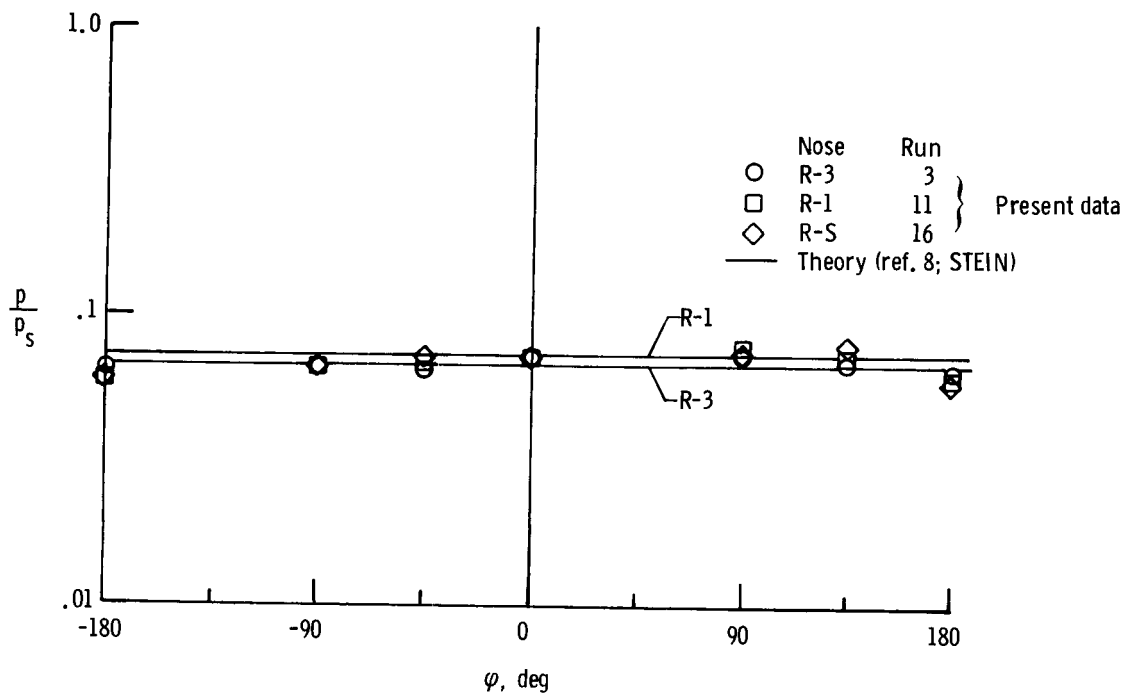


(a)  $s_c = 9.06$  in.;  $\alpha = 0^\circ$ .

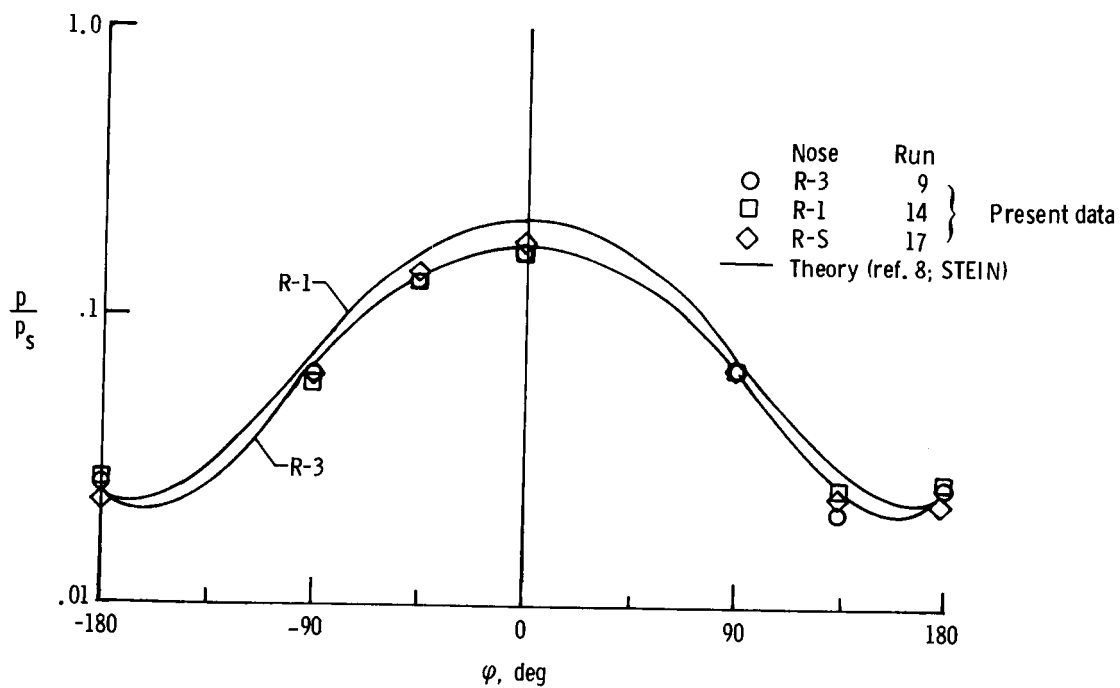


(b)  $s_c = 9.06$  in.;  $\alpha = 10^\circ$ .

Figure 31.- Effect of nose shape on circumferential pressure distribution.  
 $N_{Re} = 1.4 \times 10^6$  per foot.



(c)  $s_c = 58.0$  in.;  $\alpha = 0^\circ$ .



(d)  $s_c = 58.0$  in.;  $\alpha = 10^\circ$ .

Figure 31.- Concluded.

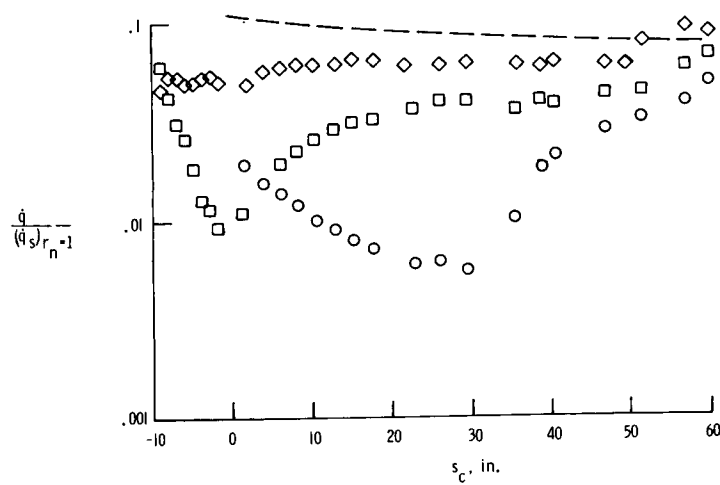
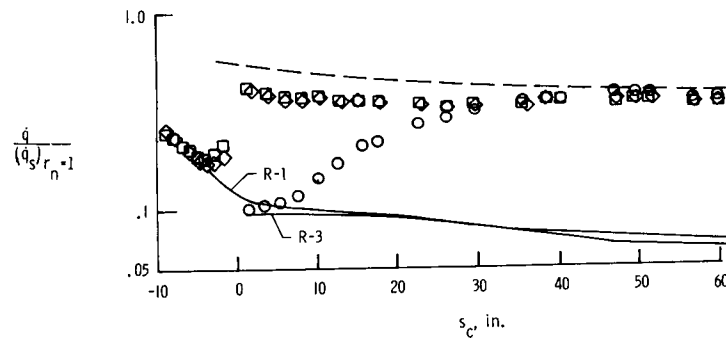
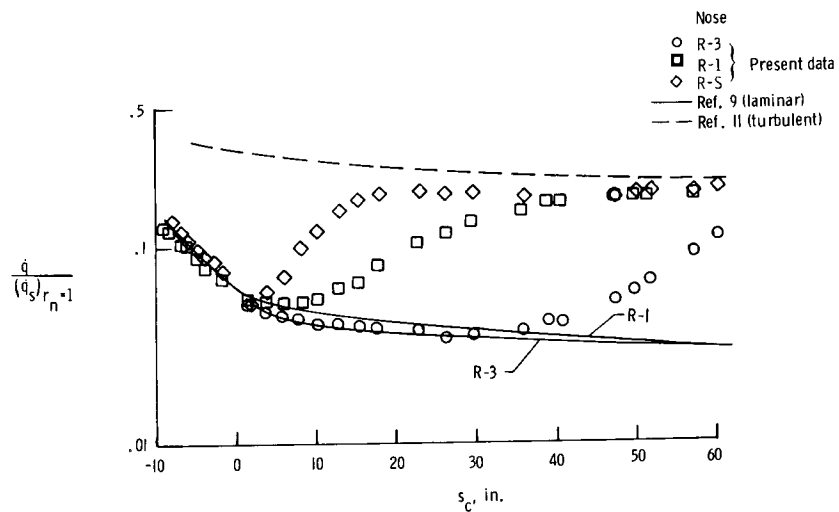
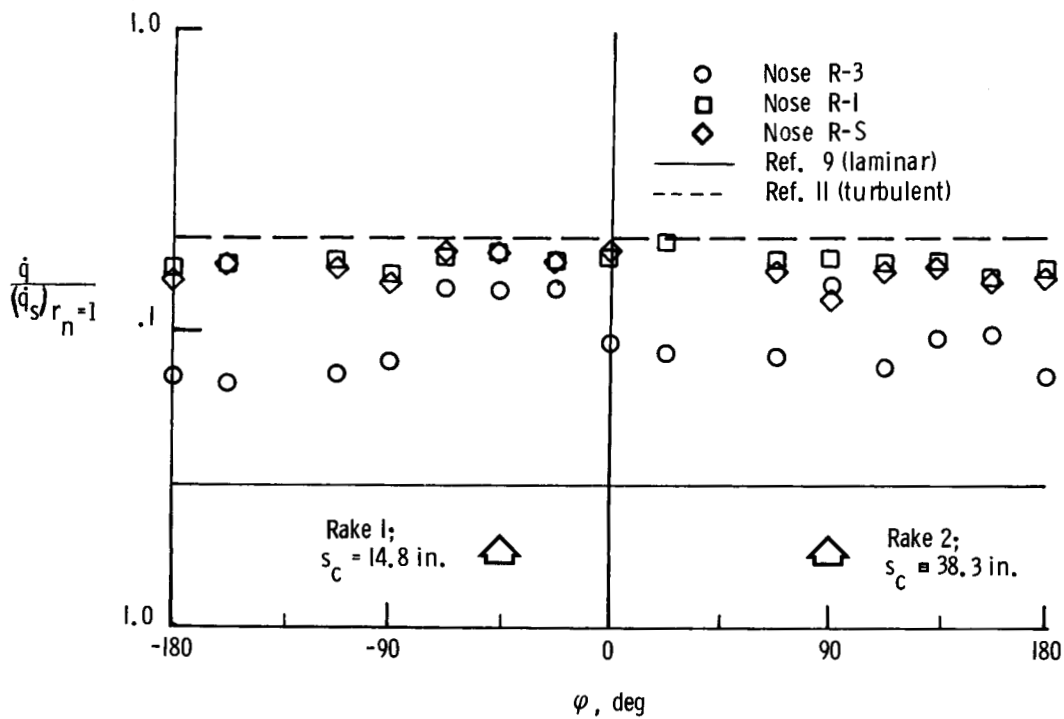
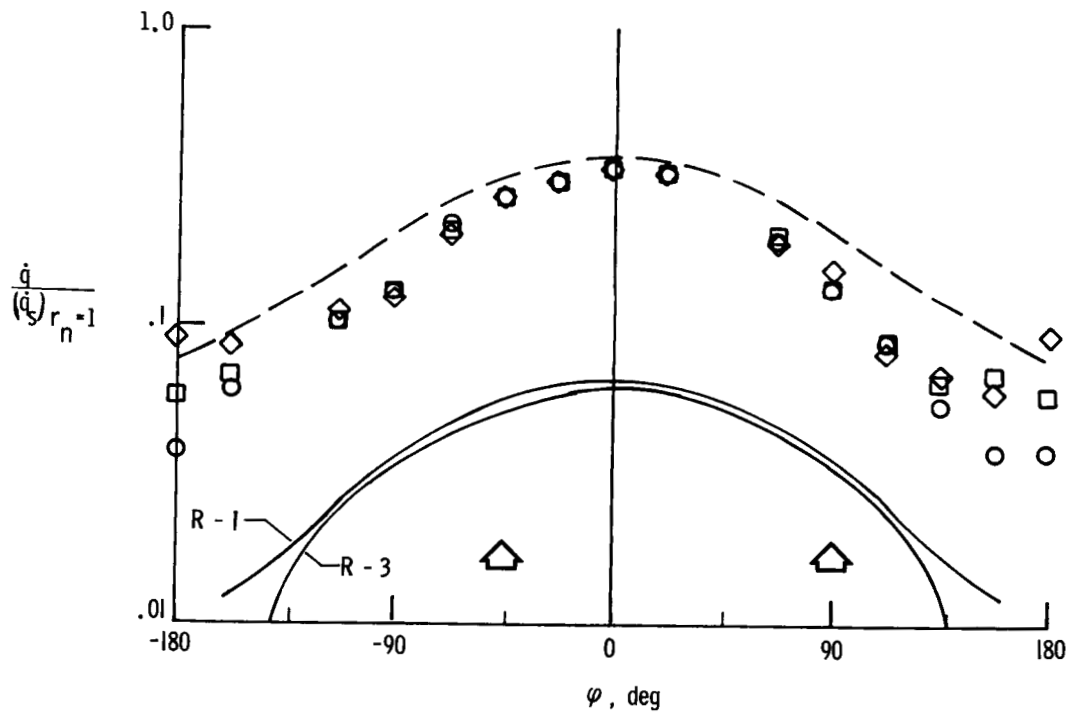


Figure 32.- Effect of bluntness on longitudinal heating distributions.  $N_{Re} = 1.4 \times 10^6$  per foot.





(a)  $\alpha = 0^\circ$ .



(b)  $\alpha = 10^\circ$ .

Figure 33.- Effect of bluntness on circumferential heating distributions.  
 $s_c = 57.2$  in.;  $N_{Re} = 1.4 \times 10^6$  per foot.

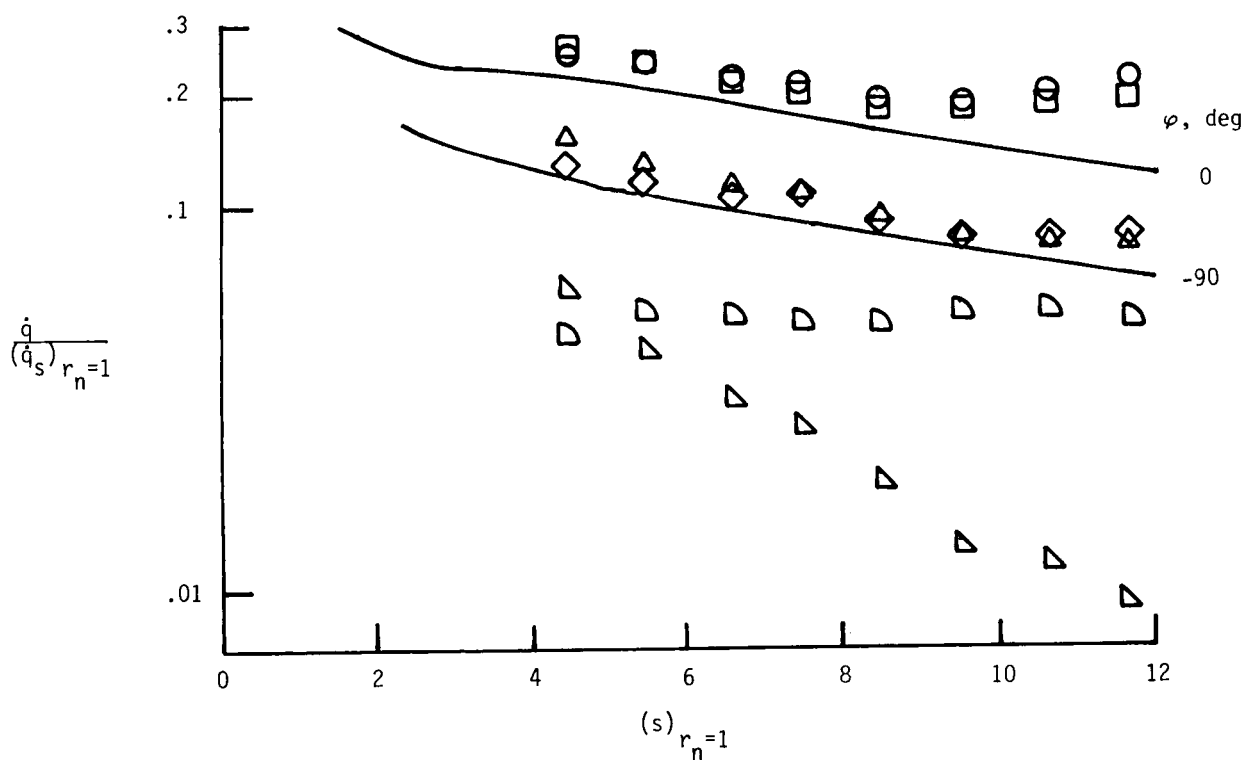
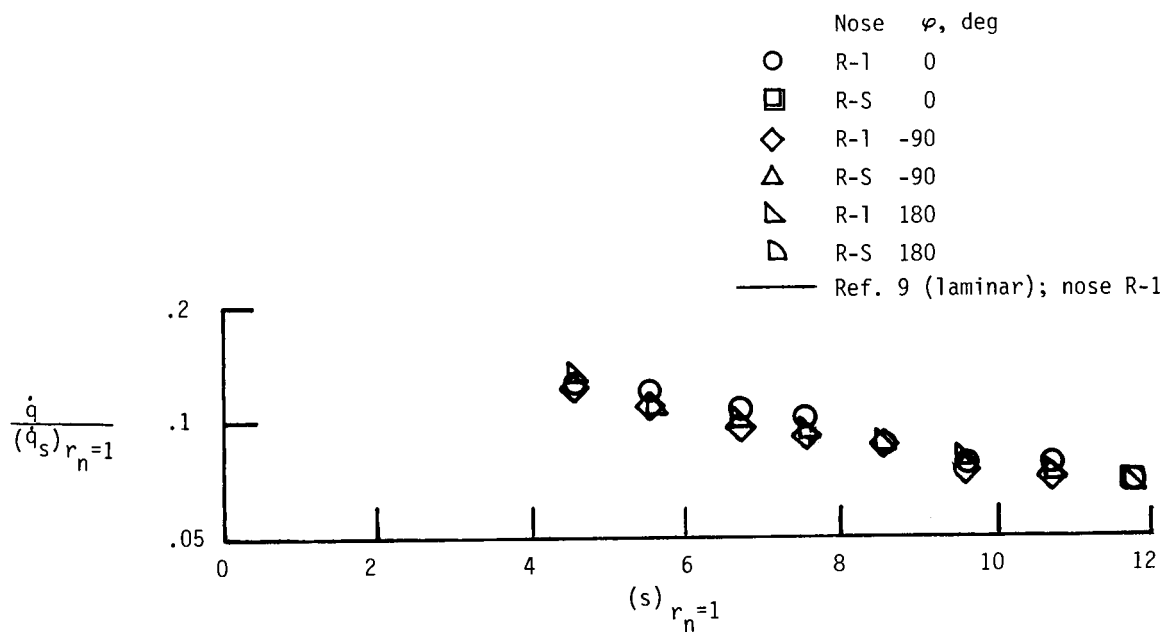


Figure 34.- Effect of nose bluntness on ogive heating.

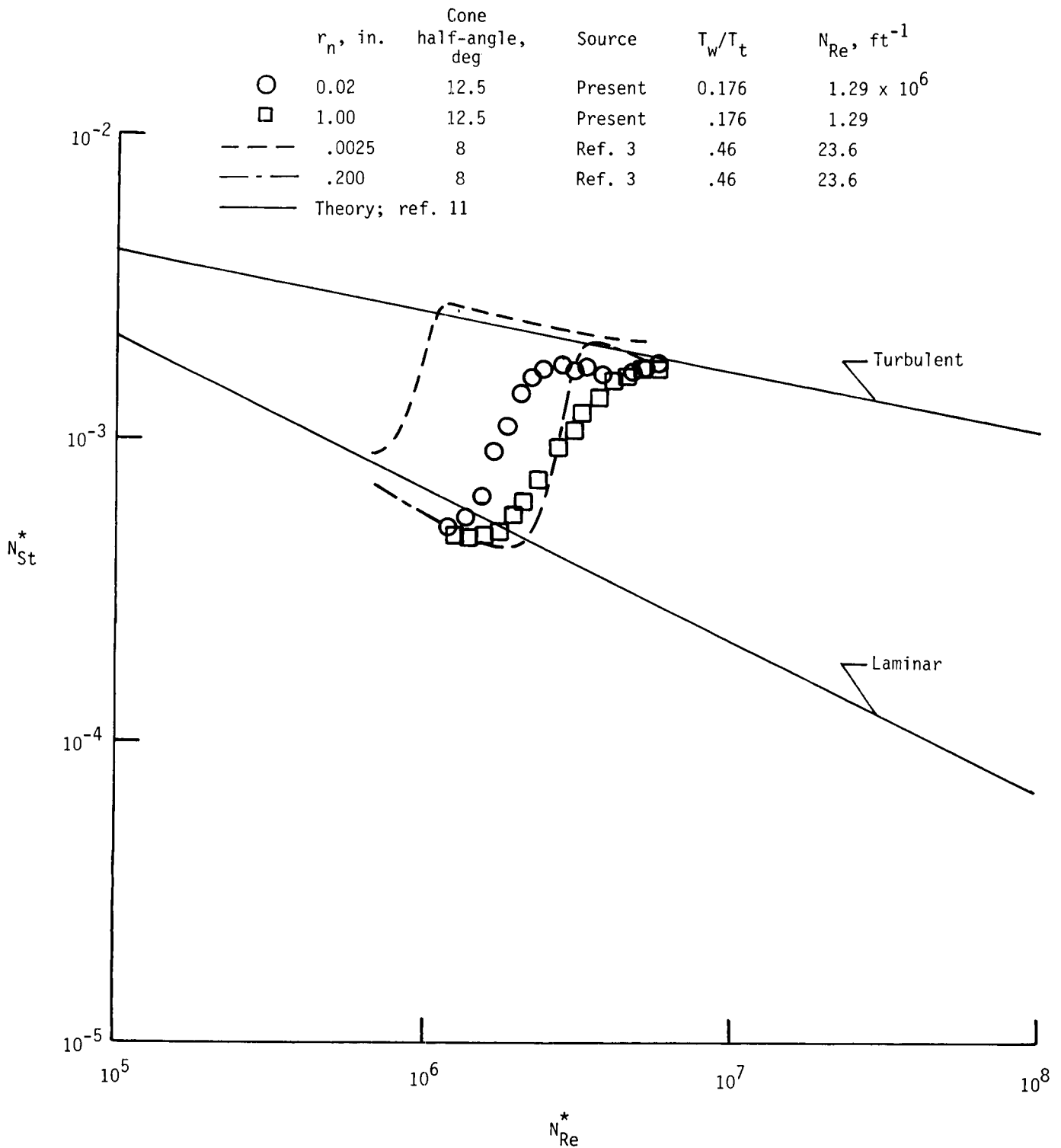
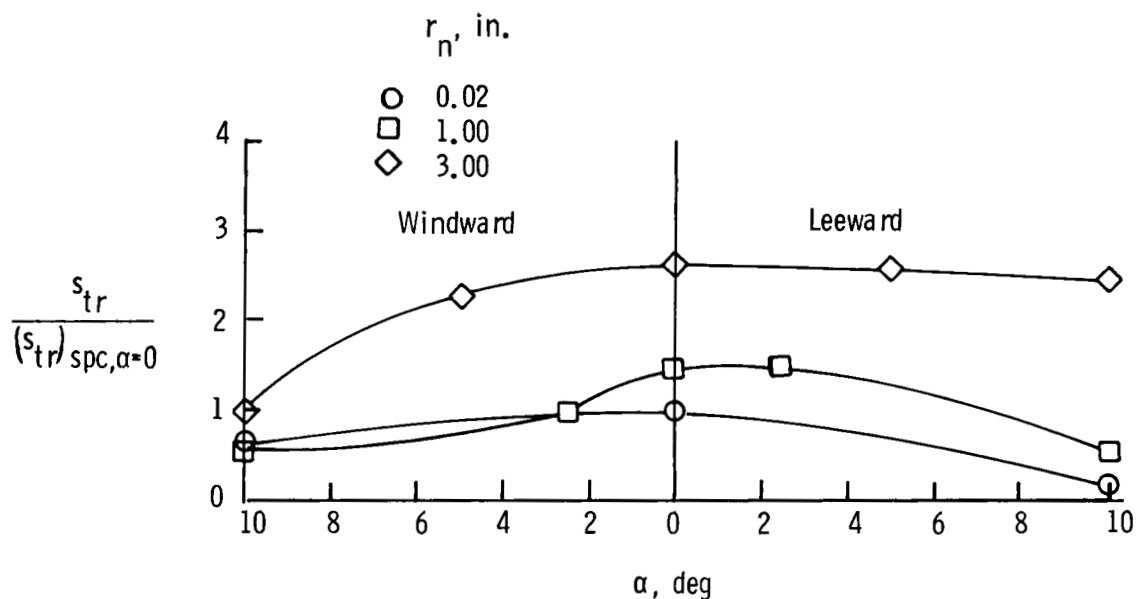
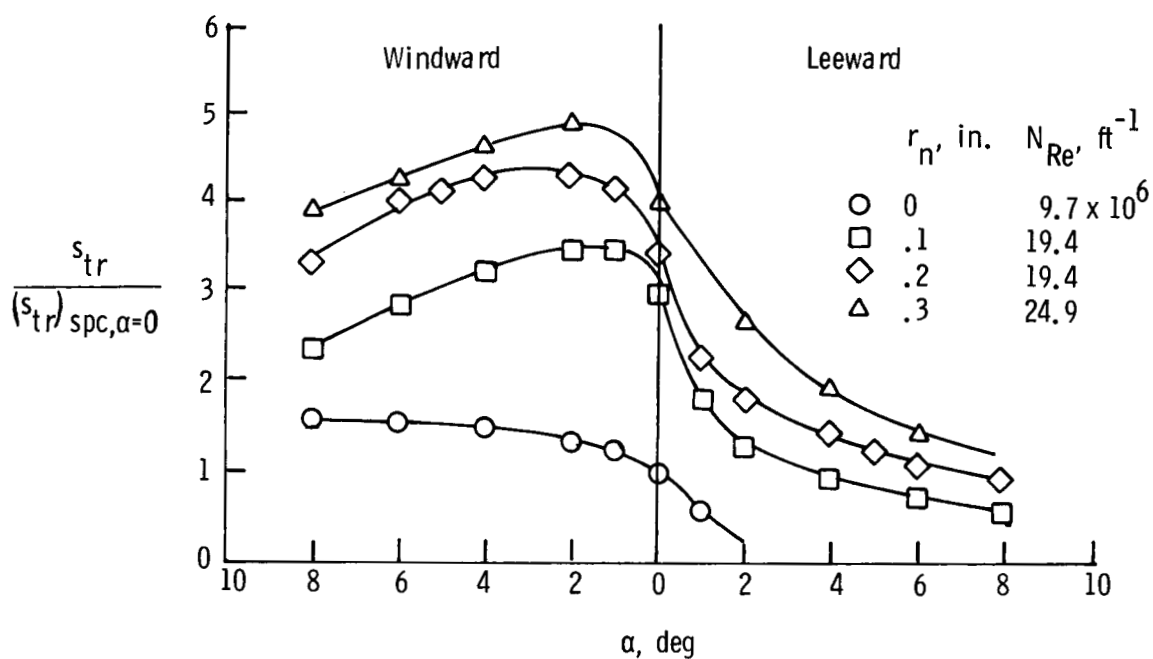


Figure 35.- Comparison of longitudinal heating distribution at  $\alpha = 0^\circ$  with theory and other tests.

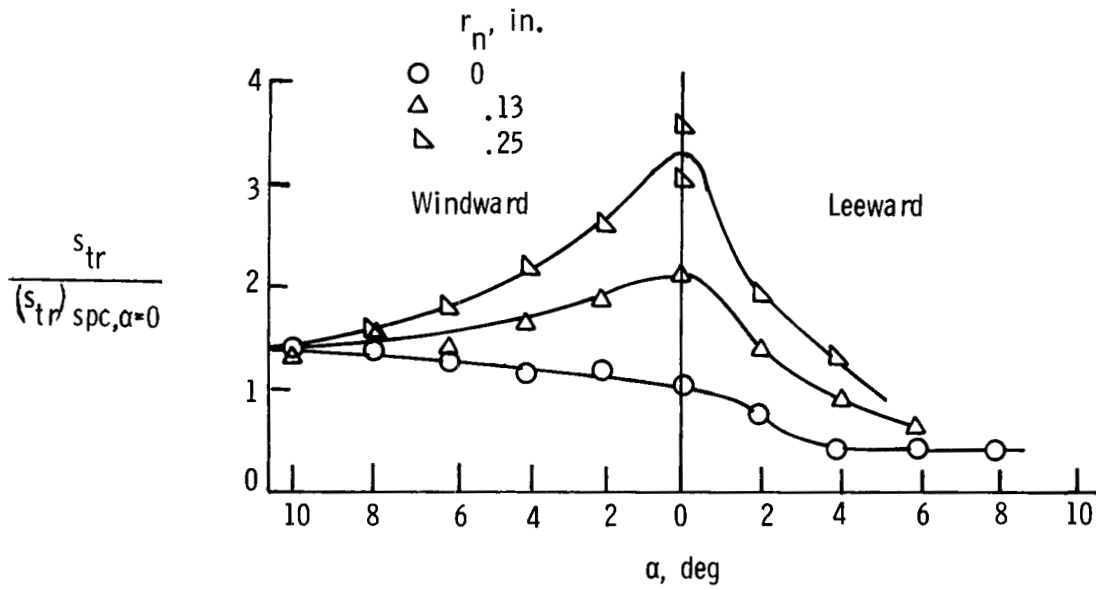


(a) Present data.  $r_b = 18.0$  in.;  $M_\infty = 6.8$ ;  $N_{Re} = 1.4 \times 10^6$  per foot;  $12.5^\circ$  half-angle;  $T_w/T_t = 0.176$ .

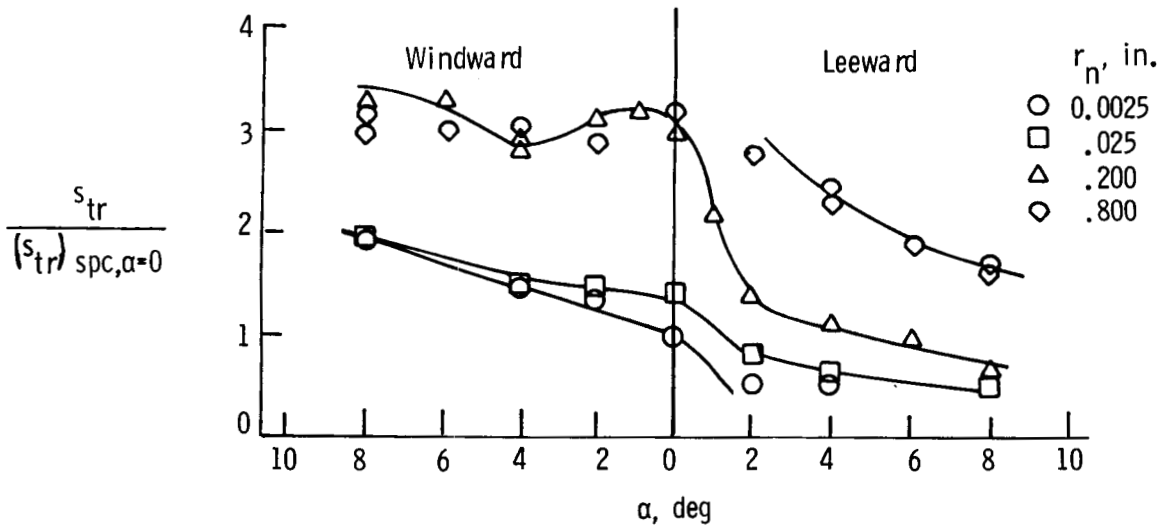


(b) Data from reference 1.  $r_b = 2.0$  in.;  $M_\infty = 5.9$ ;  $8^\circ$  half-angle;  $T_w/T_t = 0.52$  to  $0.58$ .

Figure 36.- Effect of angle of attack and bluntness on the start of transition.



(c) Data from reference 2.  $r_b = 3.0$  in.;  $M_\infty = 5.5$ ;  
 $N_{Re} = 1.2$  to  $7.0 \times 10^6$  per foot;  $8^\circ$  half-angle;  
 $T_w/T_t = 0.32$ .



(d) Data from reference 3.  $r_b = 5.0$  in.;  $M_\infty = 6.0$ ;  
 $N_{Re} = 9.7 \times 10^6$  per foot;  $8^\circ$  half-angle;  
 $T_w/T_t = 0.32$ .

Figure 36.- Concluded.

1. Report No. NASA TP-2345		2. Government Accession No.		3. Recipient's Catalog No.	
4. Title and Subtitle AEROTHERMAL TESTS OF A 12.5° CONE AT MACH 6.7 FOR VARIOUS REYNOLDS NUMBERS, ANGLES OF ATTACK, AND NOSE SHAPES				5. Report Date January 1985	
				6. Performing Organization Code 506-51-23-03	
7. Author(s) Robert J. Nowak, Cindy W. Albertson, and L. Roane Hunt				8. Performing Organization Report No. L-15729	
9. Performing Organization Name and Address  NASA Langley Research Center Hampton, VA 23665				10. Work Unit No.	
				11. Contract or Grant No.	
				13. Type of Report and Period Covered Technical Paper	
12. Sponsoring Agency Name and Address  National Aeronautics and Space Administration Washington, DC 20546				14. Sponsoring Agency Code	
15. Supplementary Notes					
16. Abstract  An experimental investigation was conducted in the Langley 8-Foot High-Temperature Tunnel at Mach 6.7 to determine the effects of free-stream unit Reynolds number, angle of attack, and nose shape on the aerothermal environment of a 3-ft base-diameter, 12.5° half-angle cone. The average total temperature was 3300°R, the free-stream unit Reynolds number ranged from $0.4 \times 10^6$ to $1.4 \times 10^6$ per foot, and the angle of attack ranged from 0° to 10°. Three nose configurations were tested on the cone: a 3-in-radius tip, a 1-in-radius tip on an ogive frustum, and a sharp tip on an ogive frustum. Surface-pressure and cold-wall (ratio of wall temperature to total temperature of 0.16) heating-rate distributions were obtained for laminar, transitional, and turbulent boundary layers. Shock shapes and profiles of Mach number and total temperature in the shock layer were obtained. Windward pressure data were well predicted by an inviscid flow-field code. Laminar heating data were well predicted on the windward side. Turbulent heating levels were in agreement with a semiempirical method. The location of the start of transition moved forward both on windward and leeward sides with increasing free-stream Reynolds numbers, increasing angle of attack, and decreasing nose bluntness.					
17. Key Words (Suggested by Author(s))  Heat-transfer data      Shock shape Pressure data Nose shapes Transition location Angle of attack			18. Distribution Statement  Unclassified - Unlimited   Subject Category 34		
19. Security Classif. (of this report)  Unclassified		20. Security Classif. (of this page)  Unclassified		21. No. of Pages  88	
				22. Price  A05	